# Nuclear modifications in strange particle production in proton-lead collisions at the LHC

By

Hong Ni

Dissertation

Submitted to the Faculty of the

Graduate School of Vanderbilt University

in partial fulfillment of the requirements

for the degree of

DOCTOR OF PHILOSOPHY

in

Physics

August 31, 2018

Nashville, Tennessee

Approved:

Julia Velkovska, Ph.D.

S. Victoria Greene, Ph.D.

M. Shane Hutston, Ph.D.

Alfredo Gurrola, Ph.D.

# ACKNOWLEDGMENTS

First and foremost, I would like to thank my beloved wife and best friend, Ting, for her patience, encouragement, and love. Without her love and support, the dissertation could not have been possible. I also want to express my sincere thanks to my parents, Zhangyong and Jin, for their unconditional love and unwavering support.

I would like to express my gratitude to my advisor, Prof. Julia Velkovska, who has guided and mentored me for the past several years. I learned not only how to do scientific research but also the skills of problem solving from her. I also want to thank Prof. Charles Maguire and Prof. Senta Greene for their mentorship and support, and Dr. Shengquan Tuo for the help I received in the past several years. My thanks go out to the former and current members of the Relativistic Heavy Ion Group at Vanderbilt University.

Finally, I would like to thank my undergraduate mentors at University of Science and Technology of China (USTC), Dr. Yichun Xu, Prof. Zebo Tang, and Prof. Hongfang Chen, for their patience and encouragement. It was them that guided me to physics research.

This thesis is based upon work supported by the U.S. Department of Energy, under the contract number DE-FG02-92ER40712.

TABLE OF CONTENTS

LIST OF TABLES

LIST OF FIGURES

# Chapter 1

# Introduction

It has been predicted theoretically that under extreme conditions, a novel phase of matter, quark gluon plasma (QGP), where quarks and gluons are the degree of freedom, can form. Due to the extreme conditions required to form QGP, the only places that QGP can be found are the early universe, shortly after the Big Bang, neutron stars, and heavy ion collisions. Thus, to study the properties of QGP, powerful colliders are needed. In 2005, the experimental collaborations at Relativistic Heavy Ion Collider (RHIC), announced the discovery of a strongly coupled system with partonic degrees of freedom. Since then, numerous intriguing analyses were performed around the world. The Large Hadron Collider started the heavy ion program in 2010 by colliding lead ions with a center-of-mass energy per nucleon pair of 2.76 TeV, which is 14 times larger than that of RHIC, and later on increased the collision energy by roughly a factor of 2. The Compact Muon Solenoid (CMS) is one of the four detectors at the LHC. Details on the LHC and the CMS detector will be introduced in Ch. 3. One of the signatures of QGP is the enhancement of strange particles in heavy ion collisions. Studies of strange particle production in different collision systems provide important tool for understanding the particle production mechanism and the evolution of the medium created in relativistic heavy ion collisions. This thesis will focus on the strange particle production with data recorded by the CMS detector.

## 1.1 Quantum chromodynamics and quark gluon plasma

Quantum Chromodynamics (QCD) is the theory that can describe the strong interaction between quarks [1] and the gluons. The main properties of QCD are:

- asymptotic freedom: the strength of the strong interaction decreases at small distance or high energies
- color confinement: isolated quarks or gluons are never observed

The asymptotic freedom is the main success of QCD, and its discovery was awarded the Nobel Prize in 2004. Perturbative QCD has shown great success in predicting the cross section of high energy processes. However, perturbative calculations are not applicable at lower energy, or in parton scattering with low momentum transfer, where the coupling constant is large. Many models have been developed to study processes in the non-perturbative domain. Among those, lattice QCD is the most promising one. In lattice QCD, field equations are solved in a finite number of discrete space-time grids. This numerical method has shown great success in the past decades thanks to the development of supercomputers and efficient algorithms. However, lattice QCD can only explore the region near the temperature axis with $\mu < T$ because of the sign problem [1] at finite baryon chemical potential.

The exact phase diagram of QCD matter is unknown. The proposed phase diagram of QCD matter is shown in Fig. 1.1, as it is conceived today. The control parameters are temperature T and baryon chemical potential $\mu$. The heavy ion collisions start with normal nuclear matter and QGP with small baryon density is expected to be formed after the collisions. The evolution of the formed QGP is similar to the evolution of the early universe started

[1] Gell-Mann coined the name based on James Joyce's book Finnegans Wake: Three quarks for Muster Mark!

with high temperature and zero baryon density. The lattice QCD calculations show that the phase transition from QGP to hadron gas changes from a first order transition at high baryon density to a crossover [2, 3]. However, the position of the critical point is unknown. A beam energy scan project is undergoing in the STAR collaboration at RHIC with the goal of locating the critical point. At the bottom right of the phase diagram with low T and high $\mu$, a color superconducting phase is predicted [4, 5]. Unfortunately, not much is known about this exotic phase of matter.

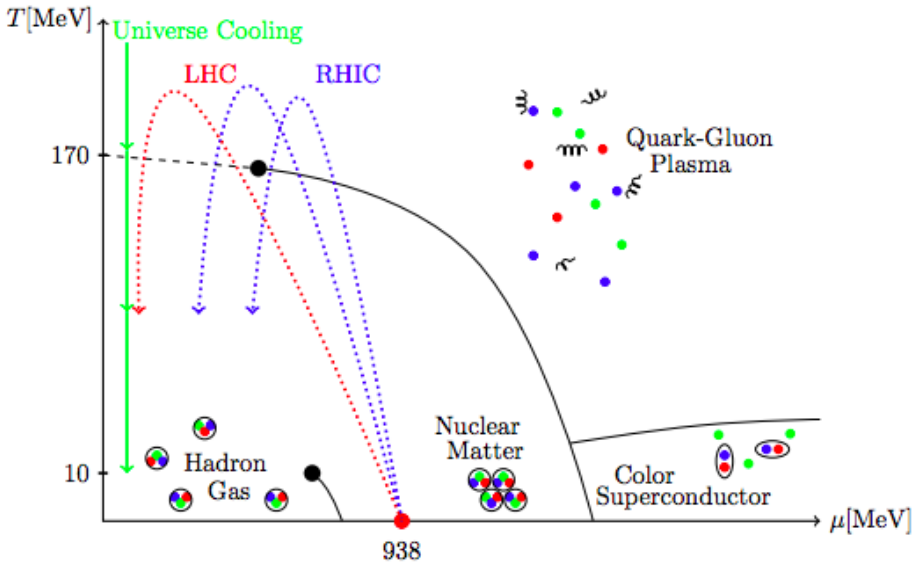


Figure 1.1: The phase diagram for strongly interacting matter, QCD. The three basic phases can be distinguished: hadronic phase, quark gluon plasma, and color super-conducting quark matter. The first order transition is represented with black solid lines. The black dashed lines represent transitions that are crossover. [6]

The Stefan-Boltzmann law for bosons [7] is:

$$\varepsilon_b = 3p = g\frac{\pi^2}{(\hbar c)^3}\frac{(k_B T)^4}{30} = g\frac{\pi^2}{30}T^4[MeV^4] \tag{1.1}$$

where $\varepsilon$ is energy density, p is pressure, and g is the number of degrees freedom of in the system.

The Stefan-Boltzmann law for fermions [7] is similar to that for bosons:

$$\varepsilon_{\mathrm{f}} = 3p = g\frac{7\pi^2}{(\hbar c)^3}\frac{(k_{\mathrm{B}}T)^4}{240} = g\frac{7\pi^2}{240}T^4[MeV^4] \tag{1.2}$$

For QGP with free massless light quarks (u, d, s) and gluons, the energy density of the system is:

$$\varepsilon = (\frac{\pi^2}{30}g_{\mathrm{g}} + \frac{7\pi^2}{240}g_{\mathrm{q}})T^4[MeV^4] \tag{1.3}$$

where $g_{\mathrm{g}}$ and $g_{\mathrm{q}}$ are degrees of freedom of gluons and quarks, respectively, with $g_{\mathrm{g}} = 16$ (2 helicity states and 8 color states) and $g_{\mathrm{q}} = 36$ (2 spin states, 3 color states, 3 flavor states, and 2 particle-antiparticle states). With the above calculation, the Stefan-Boltzmann limit for 3 flavors of massless quarks and 8 gluons is:

$$\varepsilon_{\mathrm{SB}} = 15.63T^4[MeV^4] \tag{1.4}$$

The $\varepsilon/T^4$ as a function of T from lattice QCD calculation is shown in Fig. 1.2. The calculation indicates a critical temperature $T_{\mathrm{c}}$ at around 170 MeV.

## 1.2 Heavy Ion collisions

Heavy ion collisions at relativistic energies have been studied since the early 1970s starting with the BEVALAC at Lawrence Berkeley National Laboratory, and the center of mass energy per nucleon has increased from 2.1 GeV to 5.5 TeV. With heavy ion collisions at different center of mass energy, different regions of the QCD phase diagram can be explored.

Various studies have been done to study the dynamic evolution of heavy ion collisions and

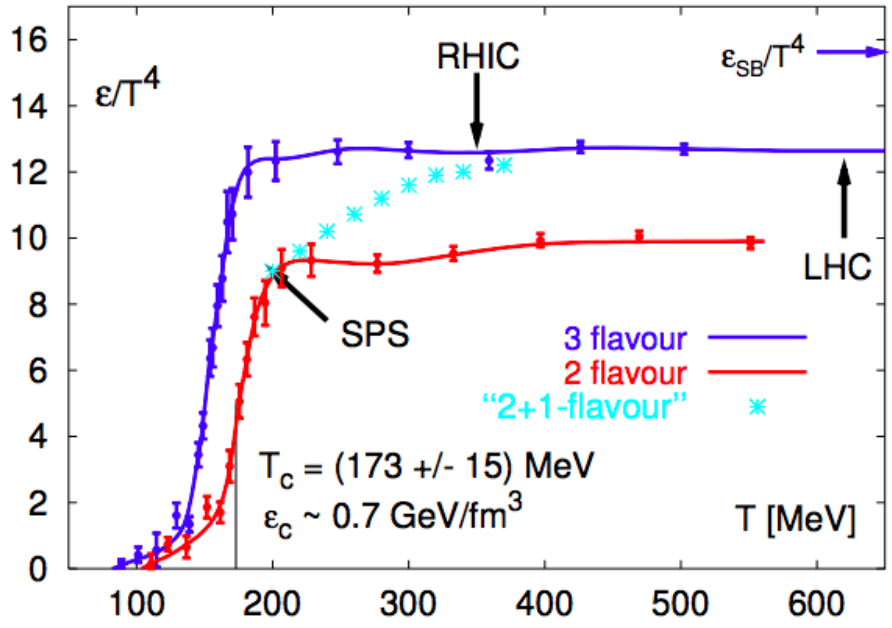


Figure 1.2: Dependence of the energy density as a function of the temperature of the hadronic matter at zero baryon potential calculated by lattice QCD at finite temperature. The calculations are performed for two massless quarks, three massless quarks and two massless quarks and one (s) with its real mass. A transition is observed at a temperature of around 173 MeV. For the calculations with a real s mass, the transition is faded away. [8]

the properties of QGP. Fig. 1.3 shows a schematic view of the stages heavy ion collisions depicted in the beam-axis vs time view. The two solid lines represent the trajectories of the two incoming nuclei that collide at z = 0 and t = 0. At the time of impact, initial events are very high energy inelastic collisions between individual nucleons, which liberate many of the partons. With enough energetical collision to get the temperature, $T$, larger than the critical temperature, $T_c$, QGP can form. Then, the formed QGP will expand and cool, and at some point $T \approx T_c$ hadrons reform. These hadrons may interact inelastically and still change identities in the hadron gas. The temperature at which the hadron abundances are fixed is denoted as the chemical freeze-out temperature, $T_{ch}$, which may be lower or it may coincide with $T_c$. The system will continue cool down until the elastic collisions among the hadrons stop. This is known as the kinetic freeze-out point. After this point, the hadrons

leave the system and can be detected.

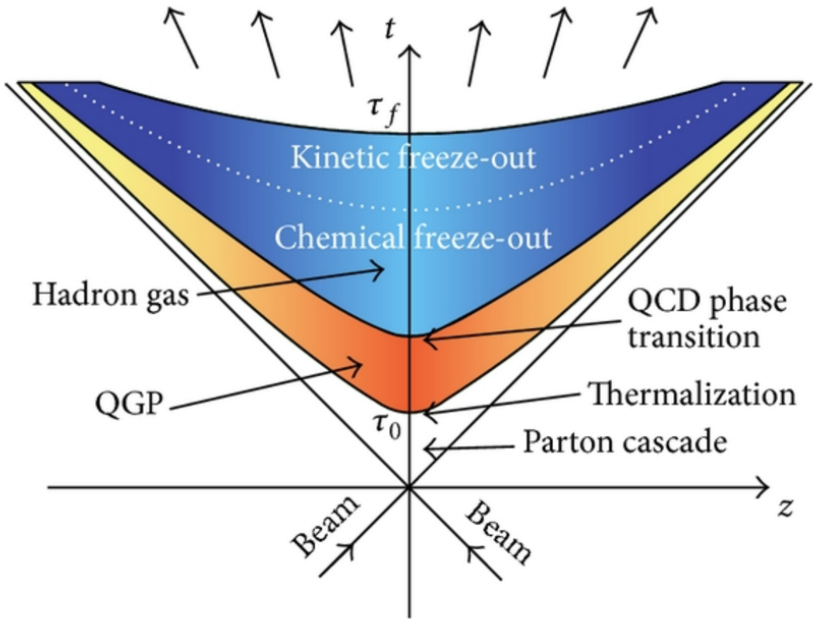


Figure 1.3: The space-time evolution of a relativistic heavy ion collision. [9]

## 1.3 Signatures of QGP

The properties of QGP cannot be observed directly, thus signatures are needed. These signatures include: strangeness enhancement [10, 11], jet quenching [12, 13, 14, 15], collective flow [16, 17, 18], and others.

1. Strangeness enhancement: This was the first signature of QGP proposed in the 1980s [10]. Since the colliding nuclei do not contain valence strange quarks, in leading order, any strange quarks observed after the collision must come from the collision. It is believed that more strange quarks will be produced in the heavy ion collisions with the existence of QGP in comparison to proton-proton collisions. Details of the strangeness production will be introduced in Ch. 2.

2. Jet quenching: A jet is a spray of particles produced by the fragmentation of a highly energetic parton, quark or gluon, in a collision. At the beginning of a collision, a pair of partons with large transverse momentum, $p_{\mathrm{T}}$, will be created from hard scatterings of incoming partons. With the existence of QGP, the colored partons lose energy by gluon emission through the strong interaction. The partons that travel a longer path will lose more energy due to the interaction with the medium. Thus, the energy of the two back-to-back jets will be unbalanced. This phenomenon is called "jet quenching".

   In CMS, jets were reconstructed based on their energy deposits in the CMS calorimeters. An event display of a dijet unbalanced event recorded by the CMS detector can be seen in Fig. 1.4.

   To characterize the dijet momentum imbalance quantitatively, the asymmetry ratio, $A_{\mathrm{J}}$, is employed. The definition of $A_{\mathrm{J}}$ is as follows:

$$A_{\mathrm{J}} = \frac{p_{\mathrm{T},1} - p_{\mathrm{T},2}}{p_{\mathrm{T},1} + p_{\mathrm{T},2}} \tag{1.5}$$

   where the subscript 1 always refers to the leading jet, and subscript 2 always refers to subleading jet. In Fig. 1.5(a), the $A_{\mathrm{J}}$ calculated by PYTHIA is compared to pp data, which shows a good agreement. The good agreement between PYTHIA + DATA and the most peripheral PbPb data is shown in Fig. 1.5(b). The centrality [2] dependence of $A_{\mathrm{J}}$ can be seen in Figs. 1.5(b)– 1.5(f). The dijet momentum balance exhibits a dramatic change in shape for the most central collisions.

3. Collective flow: In a non-central heavy ion collision, the initial overlap region of has an almond-like shape. If no collective behavior takes place in the medium, the outgoing particles will be azimuthally isotropic. However, the observed outgoing

[2] centrality is used in heavy ion physics to quantify the overlap region of the two colliding nuclei, with centrality 100% denoting the most peripheral collisions

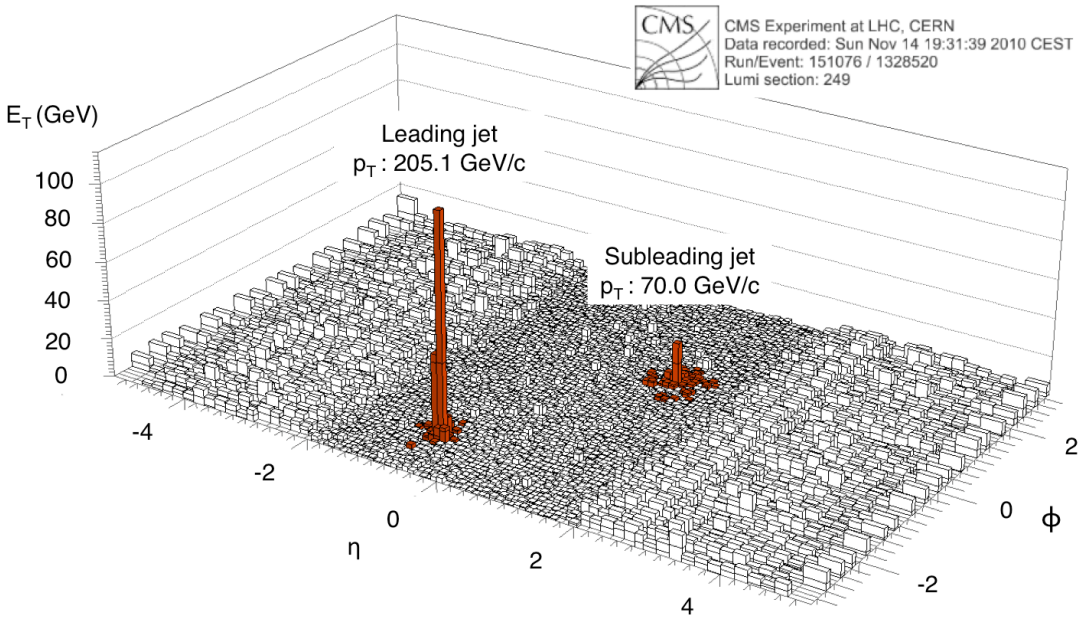


Figure 1.4: Example of an unbalanced dijet in a PbPb collision event at $\sqrt{s_{NN}} = 2.76$ TeV. Plotted is the summed transverse energy in the electromagnetic and hadron calorimeters vs $\eta$ and $\phi$, with the identified jets highlighted in red, and labeled with the corrected jet transverse momentum. [19]

particles are not azimuthally isotropic, which means that collective behavior happens in the medium. In the context of hydrodynamics, the pressure gradient in the medium is larger in the short direction of the almond, thus, more particles are collectively pushed to the short direction of the almond. The presence of collective flow reveals the fluid nature of QGP, and is considered to be an important signature of QGP.

The collective flow effect is one of the main discoveries at RHIC. The elliptic flow [3] measurements of identified hadrons are compared to ideal hydrodynamic predictions in Fig. 1.6. The good agreement between data and ideal hydrodynamic predictions indicates that the matter created at RHIC behaves like a nearly perfect fluid.

[3] the second harmonic coefficient of the azimuthal Fourier decomposition of the momentum distribution [21]

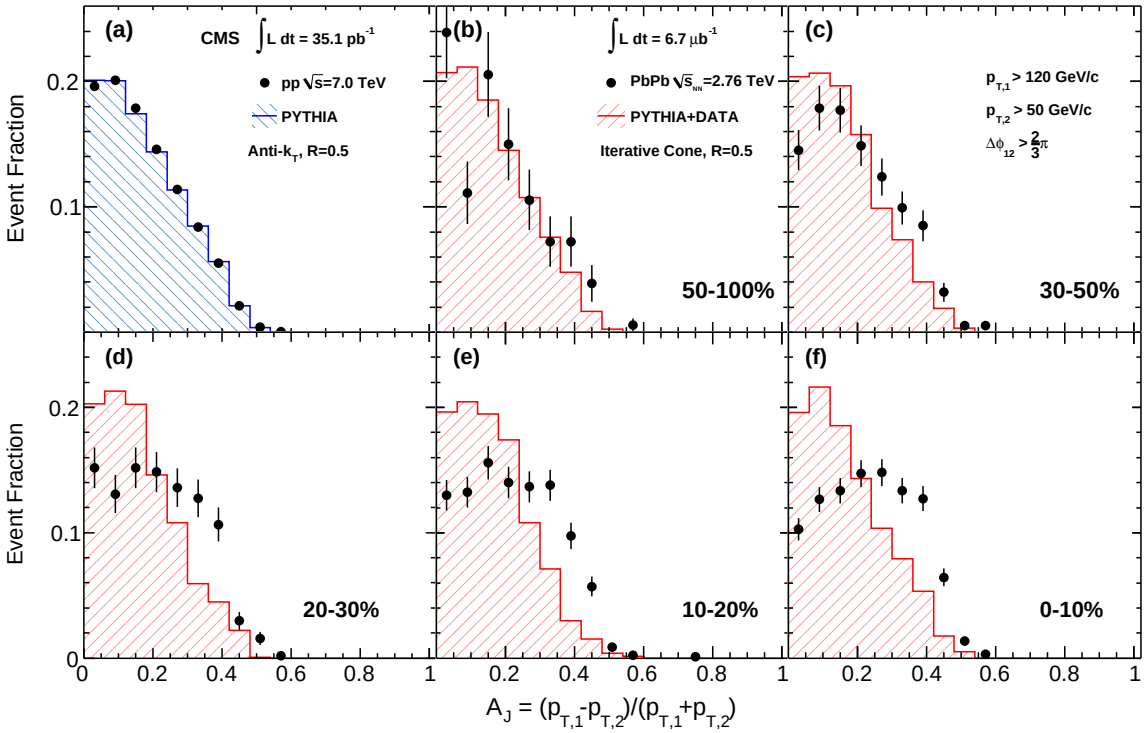


Figure 1.5: Dijet asymmetry ratio $A_J$ for leading jets of $p_{T,1} > 120$ GeV/c, subleading jets of $p_{T,2} > 50$ GeV/c, and $\Delta\phi_{12} > 2\pi/3$ for 7 TeV pp collisions (a) and 2.76 TeV PbPb collisions in several centrality bins: (b) 50%–100%, (c) 30%–50%, (d) 20%–30%, (e) 10%–20%, and (f) 0%–10%. Data are shown as black points, while the histograms show (a) PYTHIA [20] events and (b)-(f) PYTHIA events embedded into PbPb data. The error bars show the statistical uncertainties. [19]

## 1.4 Role of pA collisions

In the early days of QGP studies, pA collisions have been considered to be a control experiment for AA collisions with the expectation to disentangle the initial state effects (e.g. nuclear effects due to the presence of a cold nucleus) from the final state effects, where hot nuclear matter is created. The assumption is that QGP will not form in such a small collision volume, and only initial state effects will play a role.

However, as more and more analyses are done on pA collisions, pA collisions are found to be far more important than a simple control experiment. Recent studies on high-multiplicity

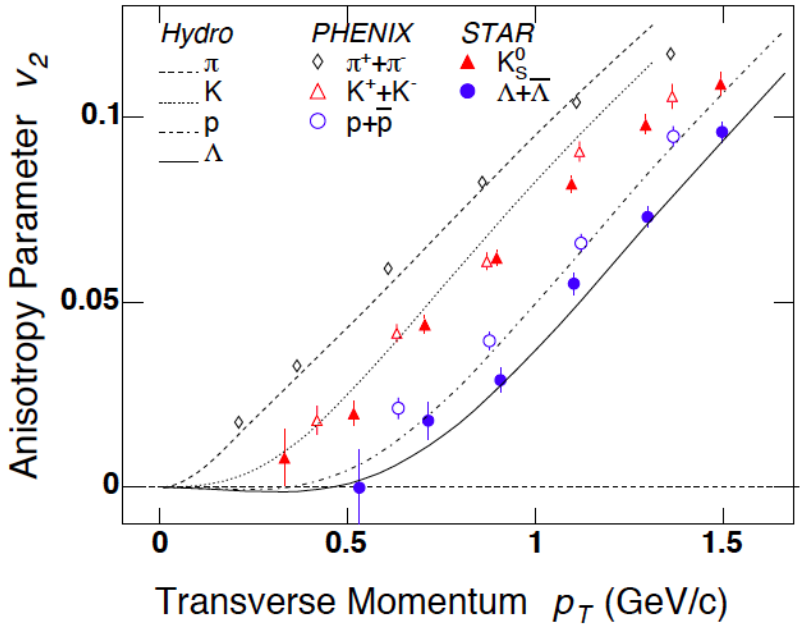


Figure 1.6: The elliptical flow for identified hadrons from STAR and PHENIX compared to ideal hydrodynamics calculations in 200 GeV AuAu collisions. [22]

pp and pA collisions show the collective behavior of the created matter just as the AA collisions [23, 24, 25, 26]. However, jet quenching is not observed in pA collisions [27, 28]. Thus, it is still not conclusive, whether QGP can be formed in small systems. Also, the studies of pA collisions provide a unique chance to study effects that can impact particle production in AA collision, such as initial-state multiple scattering of the partons prior to a hard-scattering (also known as Cronin enhancement), modification of the parton distribution functions in the nucleus, hadronization by quark recombination, and radial flow.

## 1.5 Outline of this thesis

There are two goals of this thesis. The first goal is to study the potential collective effect in small collision systems. Another goal is to study the particle production mechanism in pPb collisions reaching from low to high transverse momentum ($p_{\mathrm{T}}$).

To achieve the first goal, $K^0_S$, $\Lambda$, and $\Xi^-$ particle spectra in different multiplicity ranges are measured for all the three collision systems: pp, pPb, and PbPb. Particle ratios and average transverse kinetic energy, $\langle KE_T \rangle$, are compared among different collision systems in similar multiplicity ranges.

As to the second goal, nuclear modification factors, $R_{pPb}$, and particle yield rapidity asymmetry, $Y_{asym}$, are measured for different particle species. With these measurements, particle production mechanism such as Cronin effect, nuclear shadowing effect, radial flow effect, and recombination effect can be studied. They can provide new insights into the physics of small-volume nuclear collisions at high energies.

In Ch.2 of this thesis, the brief history and importance of strangeness production in QGP is introduced. Some previous experimental results are presented to give an idea what can be done in terms of strangeness studies.

In Ch.3, the apparatus involved in this thesis, LHC and CMS, are introduced. Special attention is given to the tracking system of the CMS detector, since this is the part that makes the results in this thesis possible.

The experimental methods are introduced in Ch.4. In this chapter, reconstruction cut criteria of strange hadrons are introduced. The way to obtain the transverse momentum spectra of strange hadrons is also presented.

The results of multiplicity dependence of strange hadron production is presented in Ch.5. Data samples and event selections used in this analysis are discussed. Systematic uncertainty checks are also presented.

In Ch.6, the results of $R_{pPb}$ and $Y_{asym}$ are shown. The structure of this chapter is similar to the previous one.

The discussion and conclusion part of the thesis is reached in Ch.7.

# Chapter 2

# Strangeness production in QGP

Strangeness as a signature of QGP was first proposed by Johann Rafelski and Berndt Müller in 1982 [10]. Since then, the study of strangeness in heavy ion collisions has been an intense field.

## 2.1 Strange quark

In 1964, Murray Gell-Mann [29] and George Zweig [30, 31] proposed the quark model independently. Nowadays, the model has been absorbed as a component of the established quantum field theory of strong and electroweak particle interactions, known as the Standard Model. The elementary particles in the standard model are shown in Fig. 2.1. In this writing, the three lightest quarks: u, d, and s, and the gluons will be discussed.

## 2.2 Strangeness as a QGP signature

Johann Rafelski and Berndt Müller proposed strangeness enhancement as a signature of QGP based on the s quark production in two different systems:

- Hadron gas, where quarks and gluons are confined in hadrons
- QGP, where the degrees of freedom are quarks and gluons

The energy threshold of producing strange hadrons in a thermally equilibrated hadron gas is significantly higher than in QGP. In the hadron gas, direct production of strange hadrons

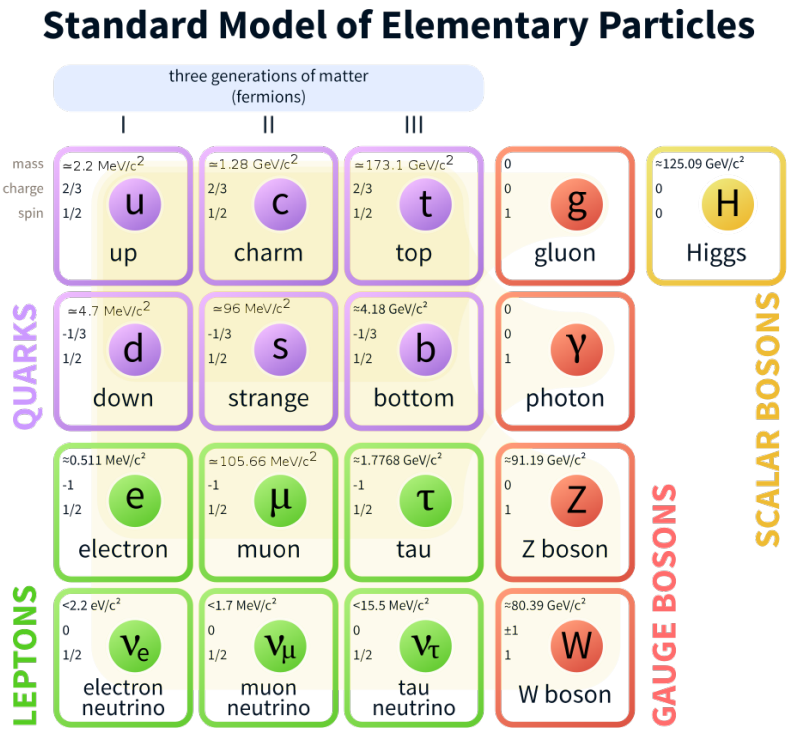


Figure 2.1: The Standard Model of elementary particles. [32]

can be achieved via $\pi + \pi \rightarrow \pi + \pi +$ strange and antistrange hadron pair. The energy threshold of this interaction is twice the rest mass of the strange hadrons. Take $\Lambda$-$\overline{\Lambda}$ baryon pair production as an example: the energy threshold is around 2231 MeV. Strange hadrons can also be produced via chain reactions: $\pi + N \rightarrow K + \Lambda$, $\pi + \Lambda \rightarrow K + \Xi$, $\pi + \Xi \rightarrow K + \Omega$. The strange hadron production via chain reactions is smaller. In this case, the production of $\Lambda$ baryon has a energy threshold of around 530 MeV. In the case of QGP, s quarks can be formed through both quark anti-quark annihilation and gluon fusion processes. The Feynman diagrams of these interactions are shown in Fig. 2.2. In these interactions, the gluon fusion is the dominant process, contributing to 80% of the $s\bar{s}$ quark production. The energy threshold needed for these interactions is reduced to the mass of $s\bar{s}$ quark pair, which is around 200 MeV. Besides the lower energy threshold of strange quark creation in QGP, the equilibration time of partonic reactions, especially due to the gluon fusion processes, are

much shorter than the ones of hadronic reactions. Based on the above arguments, creations of strange hadrons would be much easier in QGP in comparison to the production in a hadron gas, because the energy threshold is comparable to the temperature of the system and the $s\bar{s}$ pair can be produced thermally.

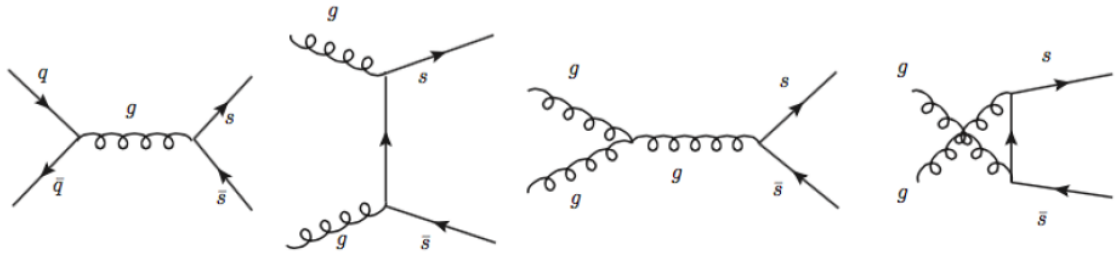


Figure 2.2: The lowest order Feynman diagrams showing the thermal production of $s\bar{s}$ pairs, via quark (left most) and gluon fusion (right three diagrams). [33]

## 2.3 Experimental results

Since there are no valence s quarks in the incoming nuclei before collisions, at the leading order, any strangeness detected later must come from the medium produced in the collisions. Thus, the study of strangeness can provide insights about this medium. The s quark is the third lightest quark, its mass is between the mass of the two lightest quarks, u and d, and the three heavier quarks. So, the production of s quarks is much easier than the heavier quarks (charm, beauty, and top). With a relatively small number of events, the studies of strange hadrons can be performed unlike the heavy flavor analyses that require significant statistics. The analyses of strange hadrons usually involve the following particles: $K^0_S, \phi, \Lambda, \overline{\Lambda}, \Xi^-, \overline{\Xi}^+, \Omega^-$ and $\overline{\Omega}^+$. Summary of these particles is shown in Table 2.1. These strange hadrons provide unique opportunities to study particle production mechanisms in collisions. The reasons are as following:

- these particles include both mesons and baryons, and therefore provide information about baryon number transport and hadronization by quark recombination

- these identified particles have mass values from 497 to 1672 MeV, providing a large dynamic range to study collective effects that depend on the particle mass
- these particles have strangeness quantum numbers S = -3, -2, -1, 0, 1, 2, 3

Table 2.1: Summary of strange hadrons involved in this thesis. Numbers are taken from Ref. [34].

| | Meson | | Baryon | | |
|---|---|---|---|---|---|
| Particle symbol | $K^0_S$ | $\phi$ | $\Lambda$ | $\Xi^-$ | $\Omega^-$ |
| Rest mass (MeV) | 497.611 | 1019.445 | 1115.683 | 1321.71 | 1672.45 |
| Quark content | $\frac{d\bar{s}+s\bar{d}}{\sqrt{2}}$ | $s\bar{s}$ | uds | dss | sss |
| Mean lifetime (s) | $8.954\times10^{-11}$ | $1.55\times10^{-22}$ | $2.631\times10^{-10}$ | $1.639\times10^{-10}$ | $8.21\times10^{-11}$ |

With these strange hadrons, various analyses can be conducted. Some examples are given below.

### 2.3.1 Particle ratios

Particle ratios provide insights on particle production mechanism by comparing the relative production rate of particles.

In Ref.[35], ALICE measured $K^0_S$ and $\Lambda$ production in PbPb collisions. The $\Lambda/K^0_S$ ratio is shown in Fig. 2.3. The $\Lambda/K^0_S$ ratios in pp collisions do not change with collision energy. The $\Lambda/K^0_S$ ratio in most peripheral PbPb collisions is consistent with that of pp collision. As the centrality moves from peripheral bins to central bins, the maximum of $\Lambda/K^0_S$ ratio shifts towards higher $p_T$, which is consistent with the prediction from radial flow effect. At higher $p_T$, $\Lambda/K^0_S$ ratios in PbPb collisions are similar to the pp results, which indicates that the particle production in this $p_T$ region is dominated by hard processes and fragmentation. The particle ratio can reveal the nature of the particle production mechanism if compared to various theoretical models.

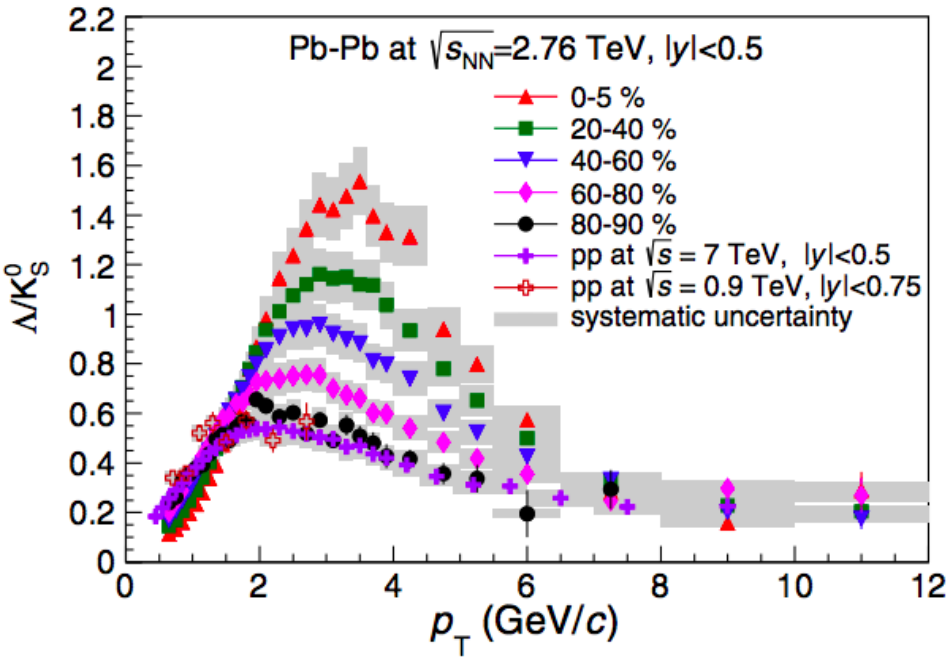


Figure 2.3: ALICE: $\Lambda/K^0_S$ ratios as a function of $p_T$ for different event centrality intervals in PbPb collisions at 2.76 TeV and pp collisions at 0.9 and 7 TeV. [35]

### 2.3.2 Strangeness enhancement

As mentioned above, the strangeness production rate in QGP is higher than in hadron gas. Thus, comparing strangeness production in heavy ion collisions and pp collisions can quantify whether strangeness is enhanced or not in heavy ion collisions.

In Ref.[36], the enhancement for $\Xi^-$ and $\Omega^-$ in PbPb collisions at 2.76 TeV as a function of the mean number of participants is shown in Fig. 2.4. The enhancements are larger than unity for all the particles. They increase with the strangeness content of the particle, showing the hierarchy already observed at lower energies and also consistent with the picture of enhanced $s\bar{s}$ pair production in a hot and dense partonic medium. Comparing the ALICE results with those from other experiments, the enhancements are found to decrease with increasing center-of-mass energy.

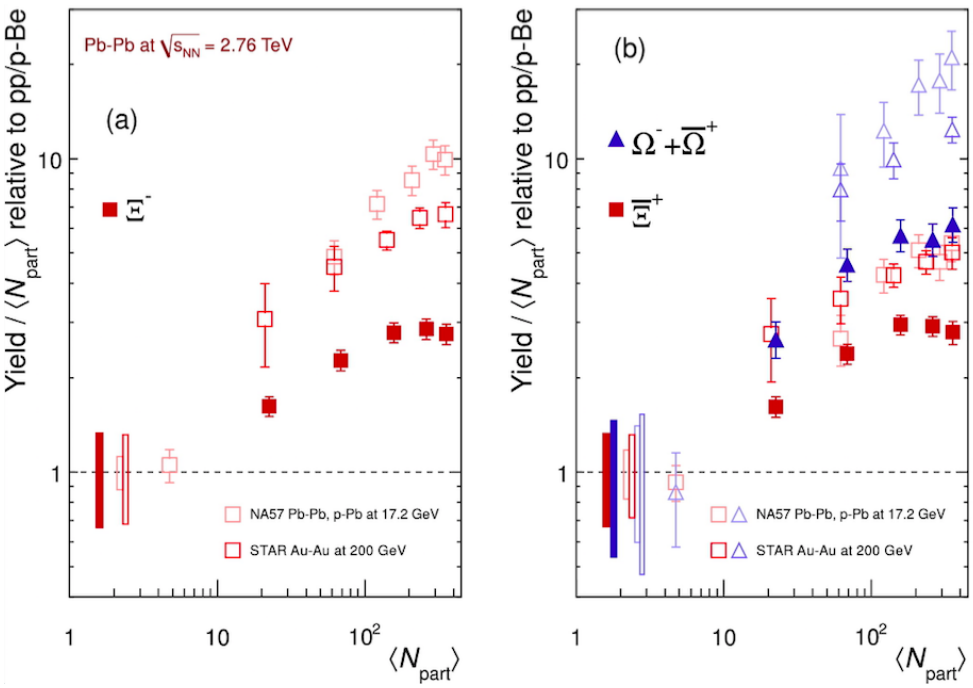


Figure 2.4: ALICE: Enhancements in the rapidity range $|y| < 0.5$ as a function of the mean number of participants $\langle N_{\text{part}} \rangle$, showing LHC (ALICE, full symbols), RHIC and SPS (open symbols) data. The LHC data use interpolated pp values. Boxes on the dashed line at unity indicate statistical and systematic uncertainties on the pp or p-Be reference. Error bars on the data points represent the corresponding uncertainties for all the heavy-ion measurements and those for pPb at the SPS. [36]

Lately, ALICE has published a paper [37], which demonstrates that the enhancement of multi-strange hadrons can be seen in high-multiplicity. This could mean that QGP can be formed in small systems with high multiplicity.

### 2.3.3 Nuclear modification factors

For collisions between two nuclei, A and B, the nuclear modification factor, $R_{\text{AB}}$, is defined as the ratio of particle yield in AB collisions to those in pp collisions scaled by the average

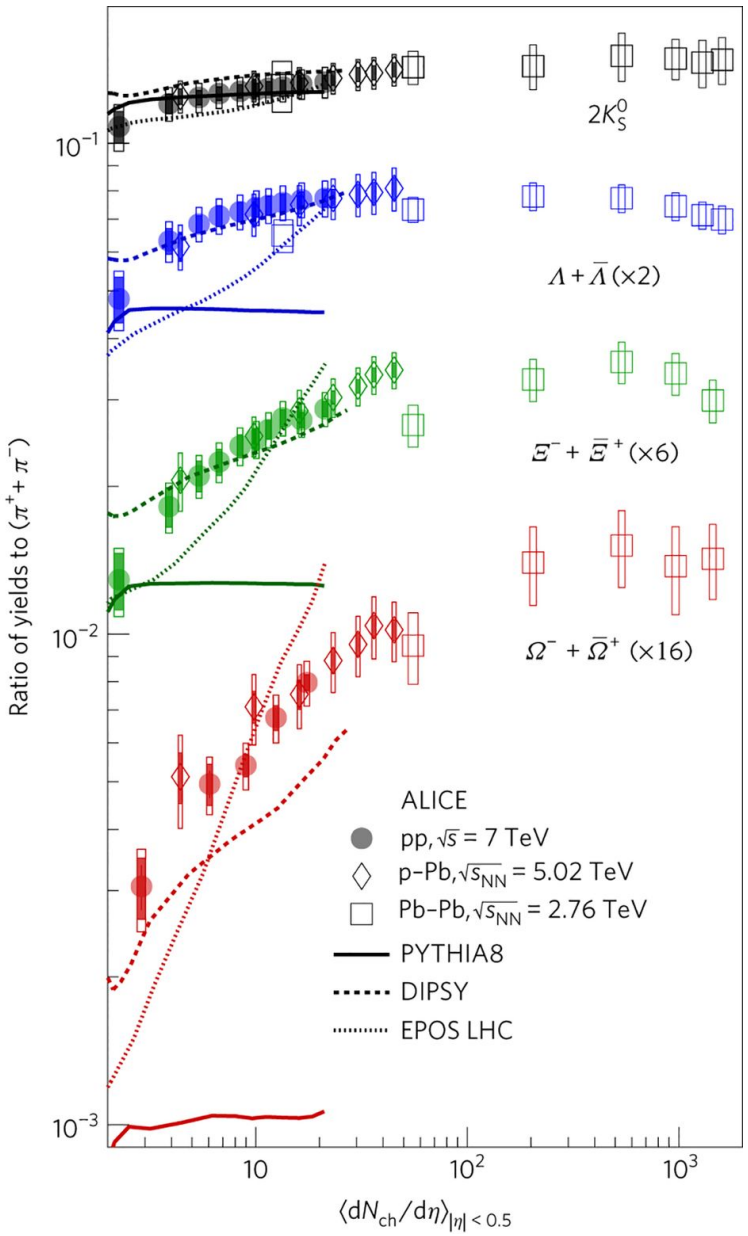


Figure 2.5: ALICE: $p_T$-integrated yield ratios to pions as a function of multiplicity measured in $|y| < 0.5$. The error bars show the statistical uncertainty, whereas the empty and dark-shaded boxes show the total systematic uncertainty and the contribution uncorrelated across multiplicity bins, respectively. The values are compared to calculations from MC models, and to results obtained in pPb and PbPb collisions at the LHC. [37]

number of binary nucleon-nucleon collisions, $\langle N_{coll} \rangle$, in AB collisions. It is given by

$$R_{AB}(p_T) = \frac{d^2N^{AB}/dp_T dy_{CM}}{\langle N_{coll} \rangle d^2N^{pp}/dp_T dy_{CM}} = \frac{d^2N^{AB}/dp_T dy_{CM}}{\langle T_{AB} \rangle d^2\sigma^{pp}/dp_T dy_{CM}}, \quad (2.1)$$

where $y_{CM}$ is the rapidity computed in the center-of-mass frame of the colliding nucleons, and $\langle T_{AB} \rangle$, the nuclear overlap function, accounts for the nuclear collision geometry and is calculated from a Glauber model [38]. If nuclear collisions behave as incoherent superpositions of nucleon-nucleon collisions, $R_{AB}$ is expected to be unity.

In Ref.[39], PHENIX measured $R_{dA}$ of identified particles as a function of $p_T$ in different centrality classes shown in Fig. 2.6. The charged kaon agrees with the charged pion within the systematic uncertainties. The $\phi$ meson exhibits no apparent modification. However, the protons show a very large and strongly centrality-dependent Cronin enhancement. The $R_{dA}$ of $\pi$, K, $\phi$, and p show significant dependence on the number of valence quarks, which suggests an important role of recombination in particle production.

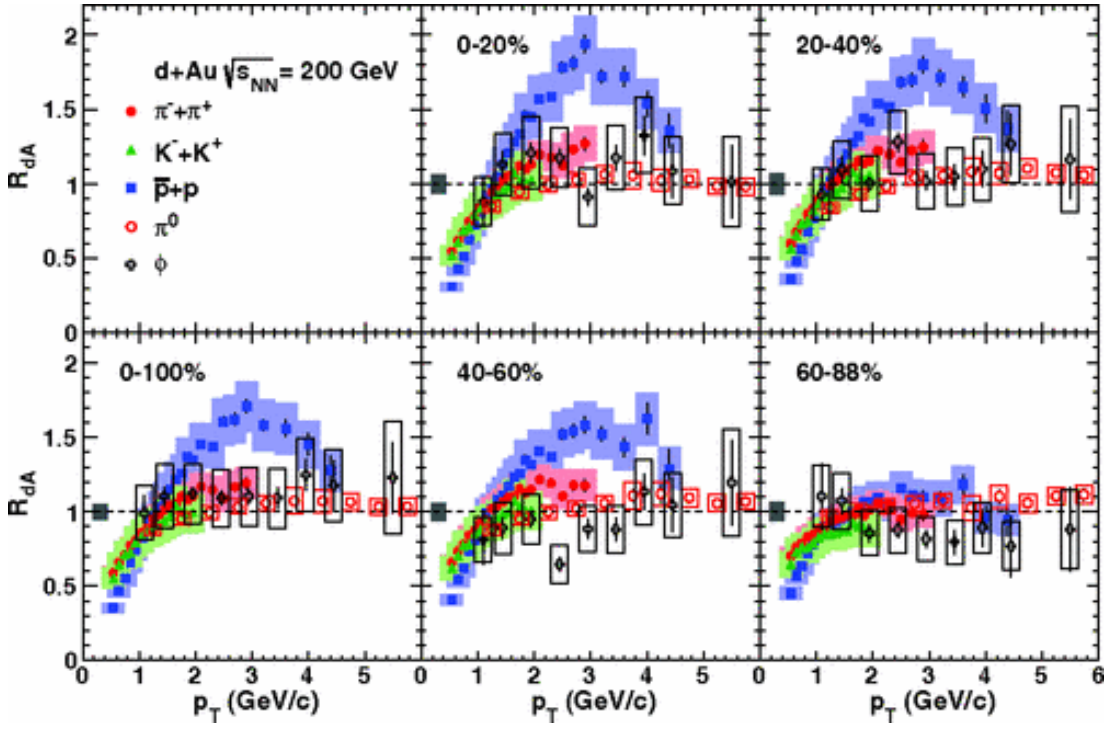


Figure 2.6: PHENIX: Nuclear modification factor $R_{dA}$ as a function of $p_T$ in different centrality classes of charge-averaged pions, kaons, and protons, $\pi^0$, and $\phi$. A dashed black line is drawn at unity as a visual aid, indicating no modification. The shaded gray boxes indicate the associated uncertainty on $N_{coll}$ from the Glauber model calculations. [39]

### 2.3.4 Radial flow of strange hadrons

As identified particles, the measurement of $v_2$ of strange hadrons can also be used to probe the potential mass dependence predicted by hydrodynamic models.

In Ref.[40], CMS measured $v_2$ values of $K^0_S$ and $\Lambda$ and compared the results to charged hadrons. In the top row of Fig. 2.7, for $p_T < 2$ GeV region for all high-multiplicity ranges, the $v_2$ values of $K^0_S$ particles are larger than those for $\Lambda$ particles at each $p_T$ value. Both of them are consistently below the $v_2$ values of inclusive charged particles. As most charged particles are pions, the data indicate a mass ordering behavior, which is consistent with the hydrodynamic expectations. At higher $p_T$, the $v_2$ values of $\Lambda$ particles are larger than those of $K^0_S$. The inclusive charged particle $v_2$ values fall between the values of these two. In the bottom two rows, the number of constituent quarks scaling is investigated. After scaling by the number of quarks, the $v_2$ for $K^0_S$ and $\Lambda$ particles are found to be in agreement.

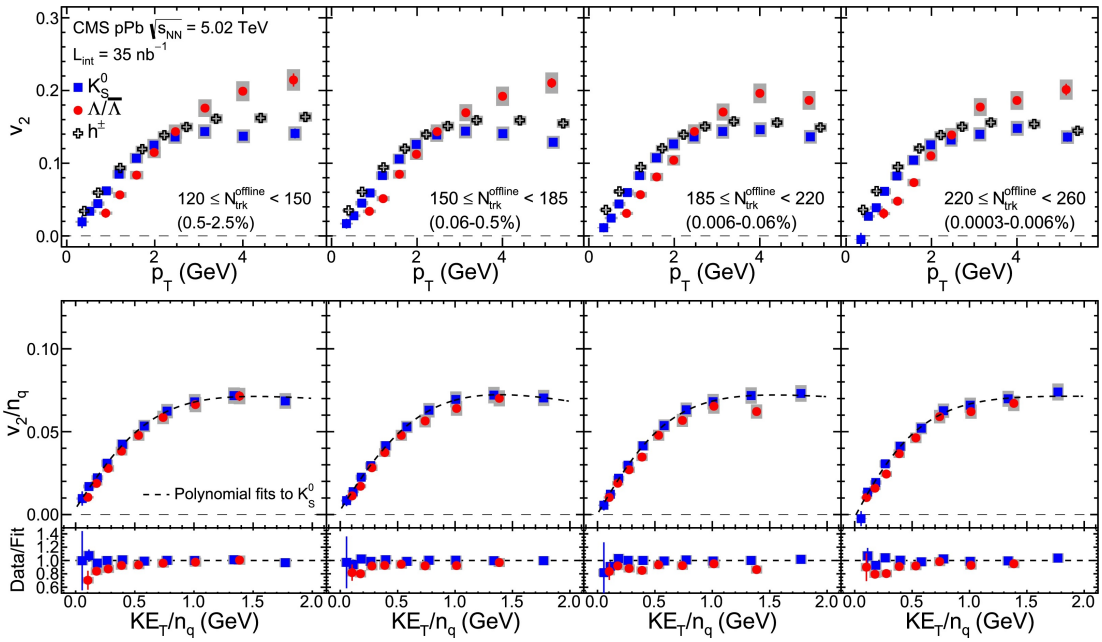


Figure 2.7: Top row: the $v_2$ results for $K^0_S$ (filled squares), $\Lambda$ (filled circles), and inclusive charged particles (open crosses) as a function of $p_T$ for four multiplicity ranges obtained from high-multiplicity triggered pPb sample at $\sqrt{s_{NN}} = 5.02$ TeV. Middle row: the $v_2/n_q$ ratios for $K^0_S$ (filled squares), $\Lambda$ (filled circles) particles as a function of $KE_T/n_q$, along with a fit to the $K^0_S$ results using a polynomial function. Bottom row: ratios of $v_2/n_q$ for $K^0_S$ and $\Lambda$ particles to the fitted polynomial function as a function of $KE_T/n_q$. The error bars correspond to the statistical uncertainties, while the shaded areas denote the systematic uncertainties. The values in parentheses give the range of the fraction of the full multiplicity distribution included for pPb. [40]

# Chapter 3

# The LHC and CMS detector

In this chapter, apparatuses used in the analysis performed in this thesis will be introduced. The LHC collider is the world's largest and most powerful particle accelerator, with the capability of accelerating proton and heavy-ion beams to extremely high energy and colliding at designed interaction points. The CMS detector is located at one of these points. The LHC collider and the CMS detector will be discussed in the following text.

## 3.1 The Large Hadron Collider

The LHC is a two-ring-superconducting-hadron accelerator as well as a collider [41]. The 26.7 km tunnel where LHC is installed is between 45 m and 170 m underground and straddles the border of Switzerland and France. The LHC was designed to collide proton beams with a center-of-mass energy of up to 14 TeV and an unprecedented luminosity of $10^{34}$ $\mathrm{cm}^{-2}\mathrm{s}^{-1}$, and collide heavy (lead) ions with an energy of up to 5.5 TeV per nucleon and a peak luminosity of $10^{27}$ $\mathrm{cm}^{-2}\mathrm{s}^{-1}$ [41]. At the time of this writing, both proton beams and heavy-ion beams have been collided in the LHC, and the top energy for pp and PbPb collisions have reached 13 and 5.5 [42] TeV, respectively. The proton beams were collided in 2010, 2011, 2012, 2013, 2015, 2016, 2017, and 2018. Proton-lead collisions took place in 2013 and 2016. Lead-lead collisions happened in 2010, 2011, 2013, and 2015. In 2017, there was a short run of xenon-xenon collisions.

This powerful collider is designed with the purpose of answering some of the fundamental questions in physics, which can be not studied otherwise. These questions are as follows:

- **The Higgs boson** Does Higgs boson exist, as predicted in the Standard Model? The discovery of this new boson with mass around 125 GeV was announced by scientists working at the LHC in year of 2012. More research on the Higgs boson is ongoing.
- **Supersymmetry** Do all known particles have more massive, invisible twins?
- **Dark matter** What is the nature of dark matter that makes up 27% of the universe?
- **Antimatter** The universe should be created with equal amounts of matter and antimatter. Where are the antimatter particles?
- **Extra dimensions** Could there be more dimensions besides the four space-time dimensions?
- **Quark Gluon Plasma** What is the nature of the matter that existed at the very beginning of our universe just after the Big Bang? This is the key goal of heavy ion physics and is the focus of the thesis.

In Fig. 3.1, the layout of the LHC is shown. From the figure, eight arcs and four beam-crossing points can be easily seen. These four beam-crossing points are where the collisions happen and the four large detectors located. The four large detectors are: **A** **T**oroidal **L**HC **A**pparatu**S** (ATLAS, located at P1), **A** **L**arge **I**on **C**ollider **E**xperiment (ALICE, located at P2) ,**C**ompact **M**uon **S**olenoid (CMS, located at P5), and The **L**arge **H**adron **C**ollider **b**eauty experiment (LHCb, located at P8).

Besides the four large detectors, there are three smaller detectors, and they share the same collision points with ATLAS, CMS and ALICE. The three smaller detectors are: **TOT**al **E**lastic and diffractive cross section **M**easurement (TOTEM, located at P5), **L**arge **H**adron **C**ollider **f**orward (LHCf, located at P1), and **M**onopole and **E**xotics **D**etector **A**t the **L**HC (MoEDAL, located at P2).

The purposes of these seven detectors are as follows:

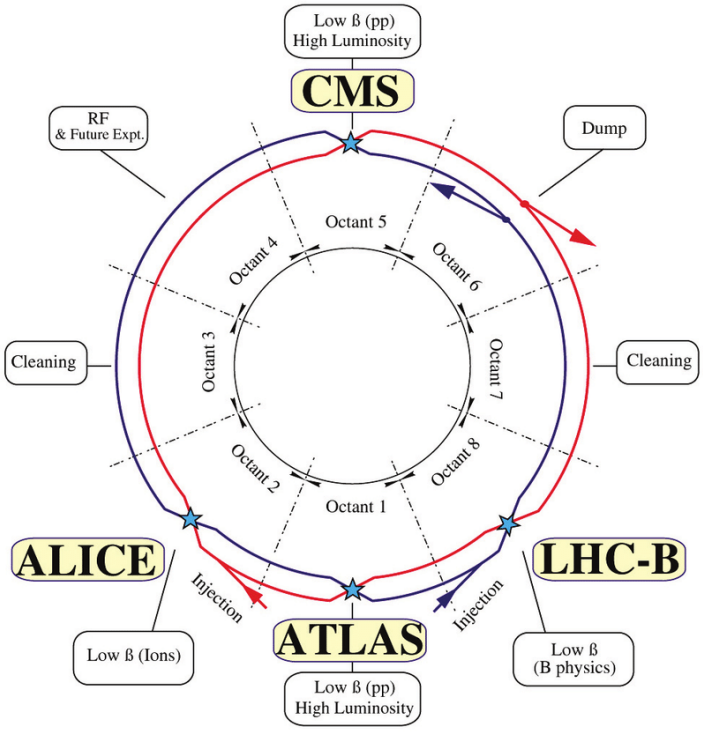


Figure 3.1: Current layout of the LHC ring. [41]

- **ATLAS** and **CMS**: general-purpose detectors built to study high-luminosity pp collisions. Later, these two experiments also showed excellent performance in heavy-ion collisions, and became key players in the heavy-ion filed ever since.
- **ALICE**: a dedicated heavy-ion detector.
- **LHCb**: focuses on CP-violation in the b-quark systems in pp collisions.
- **TOTEM**: designed for the measurement of total cross section, elastic scattering, and diffractive processes in pp collisions.
- **LHCf**: designed to study particles in "forward" region.
- **MoEDAL**: a new detector to search for Magnetic Monopole at the LHC.

The CMS detector will be introduced in the following text, since data used in this thesis were recorded by it. Other detectors are not the focus of this thesis, thus will not be introduced here.

## 3.2 The Compact Muon Solenoid Detector

As mentioned above, CMS is a general-purpose detector and can be used to study both pp and heavy-ion collisions. A detailed description of the CMS detector can be found in Ref.[43]. The overall layout of the CMS detector is shown in Fig. 3.2. The CMS detector with a weight of 12500 tons is 21.6 m long and has a diameter of 14.6 m. Inside out, each layer of the CMS detector will be introduced briefly in the following text.

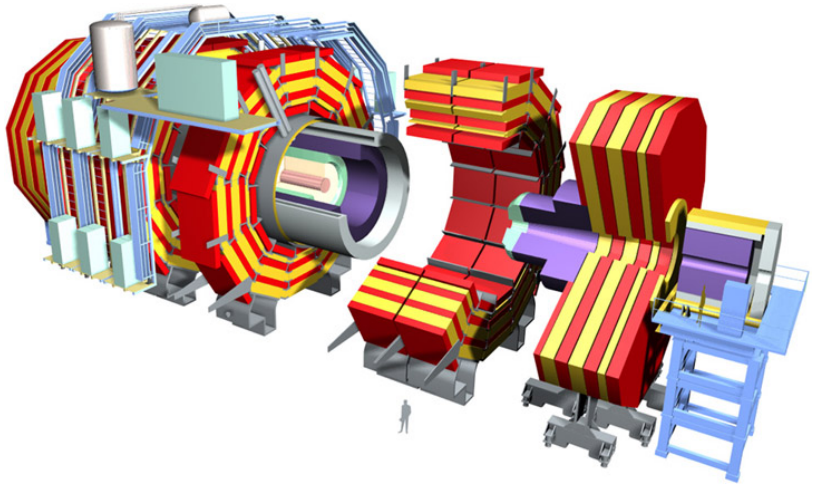

Figure 3.2: Overall layout of the CMS detector. Different parts are indicated with different color coding: the beige cylinder represents the silicon tracker, the green material represents the electromagnetic calorimeter, the purple material represents the hadronic calorimeter, the gray part is the solenoid magnet, the iron return yoke is represented by yellow, and the muon stations are shown by red. A sketch of person is placed to show the scale of the CMS detector. [44]

The first layer is the tracker that can provide a precise and efficient measurement of the trajectories of charged particles emerging from the LHC collisions, as well as a precise reconstruction of secondary vertices. The CMS tracker contains a pixel detector and a

silicon strip tracker. Detailed descriptions of the tracker will be given in the next section.

The second layer is the Electromagnetic Calorimeter (ECAL) which is designed to measure electrons and photons with good energy resolution. Lead tungstate ($PbWO_4$) crystals are used in ECAL, due to their properties of high density, short radiation length, and small Molière radius. The barrel part of the ECAL covers the pseudorapidity [1] range $|\eta| < 1.479$, while the endcaps cover the pseudorapity range $1.479 < |\eta| < 3.0$. Thus, the whole ECAL has a pseudoraidity coverage up to $|\eta| < 3.0$.

The third layer is the Hadron Calorimeter (HCAL), which is particularly important for the measurement of hadron jets, and neutrinos or exotic particles resulting in apparent missing transverse energy. The HCAL includes the following subdetectors: barrel (HB), endcap (HE), outer calorimeter (HO), forward calorimeter (HF). The longitudinal view of the CMS detector is shown in Fig. 3.3. The dashed lines are at fixed $\eta$ values.

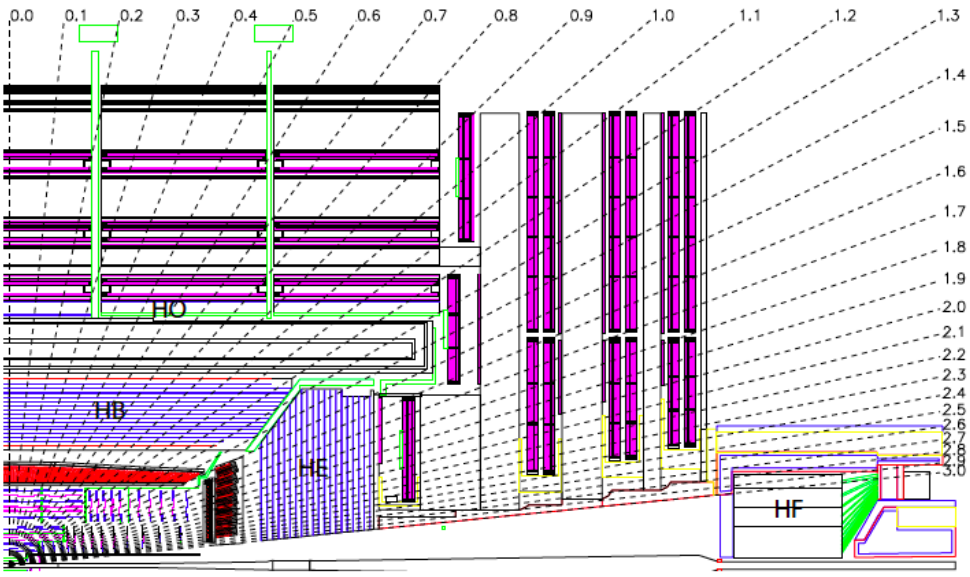


Figure 3.3: Longitudinal view of the CMS detector showing the locations of the hadron barrel (HB), outer (HO), and forward (HF) calorimeters. [43]

[1] $\eta \equiv -\ln[\tan(\frac{\theta}{2})]$, where $\theta$ is the angle between the particle three-momentum and the positive direction of the beam axis.

The name "Compact Muon Solenoid" implies that the muon system is one of the signatures of CMS. The muon system played an important role in the discovery of the Higgs boson, as the "gold plated" decay of the Standard Model Higgs boson is its decay into four muons. The muon system has three functions: muon identification, momentum measurement, and triggering. The muon system has a cylindrical, barrel section and two planar endcap regions. In the barrel region, drift chambers with standard rectangular drift cells are used, since the muon rate is low and the 4-T magnetic field is uniform and mostly contained in the steel yoke. In the two endcap regions, cathode strip chambers are used, because the muon rates are high and the magnetic field is non-uniform.

Besides the subdetectors mentioned above, there are other subdetectors, such as The Beam Scintillator Counters (BSC) and The Beam Pick-up Timing for the eXperiments (BPTX). These subdetectors will not be discussed in this thesis.

In the following section, the tracker system of CMS will be described as it is directly relevant to the analysis of strange particles.

### 3.2.1 The Inner Tracker System

As mentioned above, the goal of the tracking system of CMS is to provide a precise and efficient measurement of the trajectories of charged particles emerging from the LHC collisions. At the LHC design luminosity of $10^{34}$ $\mathrm{cm}^{-2}\mathrm{s}^{-1}$ [2], there will be on average about 1000 particles from more than 20 overlapping proton-proton interactions traversing the tracker for each bunch crossing, i.e. every 25 ns. Therefore, a detector technology featuring high granularity and fast response is required. Furthermore, the intense particle flux could cause severe radiation damage to the tracking system and the detector components should be able to operate for an expected lifetime of ten years in such harsh environment.

[2] In 2017, the instantaneous luminosity reached $2.06\times10^{34}$ $\mathrm{cm}^{-2}\mathrm{s}^{-1}$, which is over twice of the design. [45]

To fulfill all the requirements, the tracker was designed entirely based on silicon detector technology.

The CMS tracker is composed of a pixel detector with three barrel layers at radii between 4.4 cm and 10.2 cm and a silicon strip tracker with ten barrel detection layers extending outwards to a radius of 1.1 m. Each system is completed by endcaps which consist of two disks in the pixel detector and three plus nine disks in the strip tracker on each side of the barrel, extending the acceptance of the tracker up to a pseudorapidity of $|\eta| < 2.5$. A schematic drawing of the CMS tracker is shown in Fig. 3.4. As shown in Fig. 3.4, these layers are: Tracker Inner Barrel (TIB), Tracker Outer Barrel (TOB), Tracker Inner Disc (TID), and Tracker Endcap (TEC).

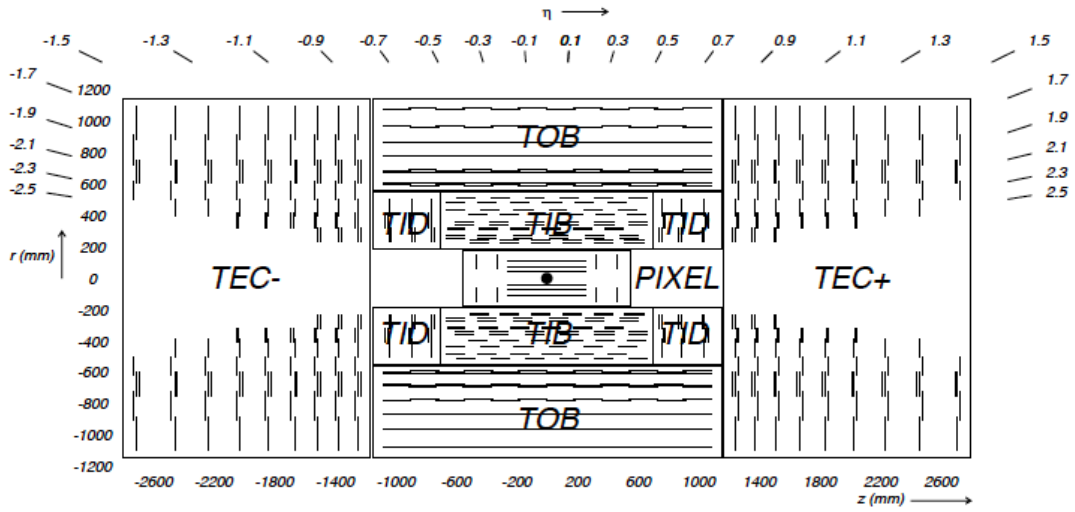


Figure 3.4: Schematic cross section through the CMS tracker. Each line represents a detector module. Double lines indicate back-to-back modules which deliver stereo hits. [43]

#### 3.2.1.1 Pixel detector

The pixel system is the part of the tracking system that is closest to the interaction region. It contributes precise tracking points in r-$\phi$ and z and therefore is responsible for a small

impact parameter resolution that is important for good secondary vertex reconstruction. A geometrical layout of the pixel detector can be seen in Fig. 3.5. From Fig. 3.5, it is clear that the pixel detector can cover a pseudorapidity range $-2.5 < \eta < 2.5$, which matches the acceptance of the central tracker. There are three barrel layers (BPix) and two endcap disks (FPix). The 53-cm-long BPix layers locate at mean radii of 4.4, 7.3, and 10.2 cm. The FPix disks extending from 6 to 15 cm in radius, are placed on each side at z = $\pm$ 34.5 and z = $\pm$46.5 cm.

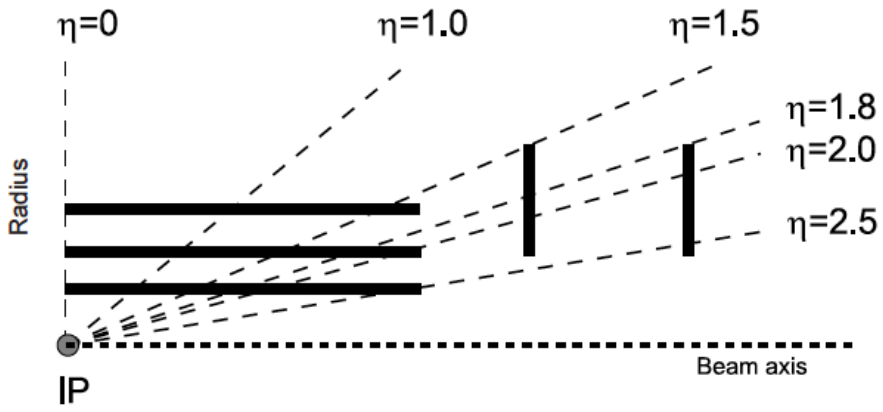


Figure 3.5: Geometrical layout of the pixel detector. [43]

To meet the challenge of the increasing luminosity in LHC, the CMS collaboration has built a new pixel detector that was installed in March 2017 [46]. This new pixel detector is called “Phase-1”, while the previous one is called “Phase-0”. A comparison of the layouts of Phase-1 pixel detector and Phase-0 pixel detector is shown in Fig. 3.6. With the new pixel detector, high tracking efficiency can be maintained until Long Shutdown 3, which will take place in 2024–2025. A two year shutdown (Long Shutdown 2) is also scheduled for 2019–2020.

All the data used in this thesis were collected with Phase-0 pixel detector.

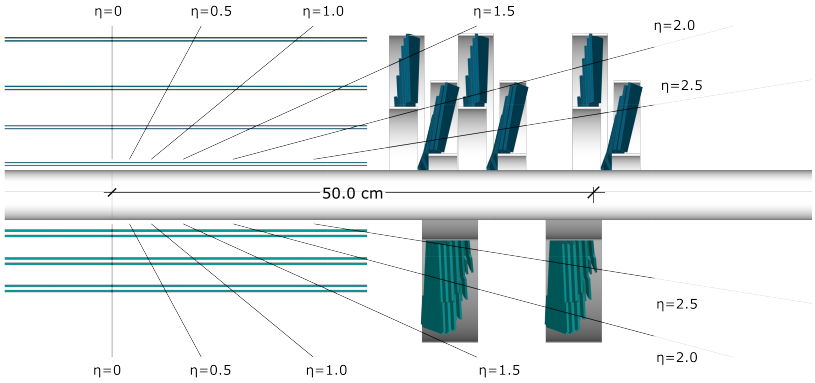


Figure 3.6: CMS pixel detector upgrade: “Phase-1” versus “Phase-0”. [47]

#### 3.2.1.2 Silicon strip tracker

The TIB consists of four concentric cylinders placed at radii of 255.0 mm, 339.0 mm, 418.5 mm, and 498.0 mm respectively from the beam axis that extend from -700 mm to + mm along the z axis. The TID contains three disks placed in z between $\pm$ 800 mm and $\pm$ 900 mm. The disks are identical and each one consists of three rings, which span the radius from roughly 200 mm to 500 mm. The TOB consists of a single mechanical structure (wheel) supporting 688 self-contained sub-assemblies, called rods. The wheel has a length of 2180 mm, and inner and outer radii of 555 mm and 1160 mm, respectively. As to the TEC, the endcaps extend radially from 220 mm to 1135 mm and from $\pm$ 1240 mm to $\pm$ 2800 mm along the z-direction. The silicon strip tracker has the same pseudorapidity coverage as the pixel detector, which is $|\eta| < 2.5$. As can be seen later, the large pseudorapidity coverage of CMS tracker enables the measurement of the $p_{\mathrm{T}}$ spectra of strange particles in different rapidity ranges, and to study their evolution with rapidity.

# Chapter 4

# Experimental method

In this chapter, the methods used to reconstruct $K^0_S$, $\Lambda$, $\Xi^-$, and $\Omega^-$ candidates, how signal counts are extracted, how efficiency corrections are performed, and how to deal with "non-prompt" $\Lambda$ are discussed in details.

## 4.1 Reconstruction of $K^0_S$, $\Lambda$, $\Xi^-$, and $\Omega^-$ candidates

The $K^0_S$ and $\Lambda$ candidates, generally referred to as $V^0$ [1], are reconstructed via their decay topology, $K^0_S \to \pi^+ + \pi^-$ and $\Lambda \to \pi^- + p^+$, by combining pairs of oppositely charged tracks that are displaced from the primary vertex to form a good secondary vertex with an appropriate invariant mass. For $K^0_S$ candidate reconstruction, two tracks are assumed to be pions, and pion mass is assigned to each track. For $\Lambda$ candidate reconstruction, the track with lower momentum is assumed to be a pion track, while the one with higher momentum is assumed to be a proton track. For $\Xi^-$ and $\Omega^-$ candidate reconstruction, ($\Xi^- \to \Lambda + \pi^-$ and $\Omega^- \to \Lambda + K^-$), a track with the proper charge is combined with a previously reconstructed $\Lambda$ candidate to form a good secondary vertex with a reasonable invariant mass. This extra track is assumed to be a pion (kaon) for $\Xi^-$ ($\Omega^-$) candidate reconstruction. Detailed discussion regarding reconstruction criteria for $K^0_S$, $\Lambda$, $\Xi^-$, and $\Omega^-$ candidates is shown below.

In Fig. 4.1, the decay topology as well as the topological selections that will be mentioned below of $\Lambda$ are demonstrated. A schematic plot of $\Xi^-$ decay topology is shown in Fig. 4.2.

[1] The name comes from the facts that they are neutral particles and their decay topology have the "V" shape.

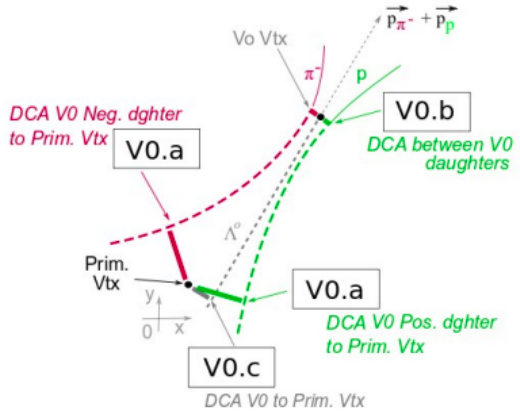


Figure 4.1: Decay topology as well as topological selections of Λ baryon. "DCA" stands for distance of closest approach. [48]

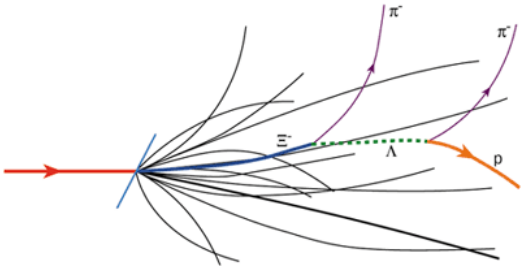


Figure 4.2: Schematic decay topology of $\Xi^-$ baryon. [49]

### 4.1.1 Reconstruction of $V^0$ candidates

To reduce the background of $V^0$ candidates, a set of topological selections, shown in Fig. 4.1 are needed. In our analysis, a quantity called "DCA significance", which is defined as DCA value divided by the uncertainty of DCA, is used.

Criteria of $V^0$ reconstruction are summarized below:

- 3D distance of closest approach significance with respect to the primary vertex $> 2$ for both daughter tracks, since secondary tracks that come from particle decays will be displaced.

- 3D distance of closest approach significance of the $V^0$ candidate with respect to the primary vertex $< 2.5$, since primary tracks will point to the primary vertex will small significance.

- 3D separation significance between $V^0$ vertex and primary vertex $> 3$, since decay length of $V^0$s are in the order of several centimeters [2].

The cut variables used for $V^0$ reconstruction mentioned above are identical as previous CMS publication: QCD-10-007 [50]. In a recent CMS publication, which is also an important part of this thesis, HIN-15-006 [51], cosine pointing angle cut, which is shown in Fig. 4.3, was used instead of the 3D distance of closest approach significance of the $V^0$ with respect to the primary vertex. Both cuts serve the same purpose to require the momentum of $V^0$ candidates to point back to the primary vertex. My research confirmed that these two cuts yield consistent results.

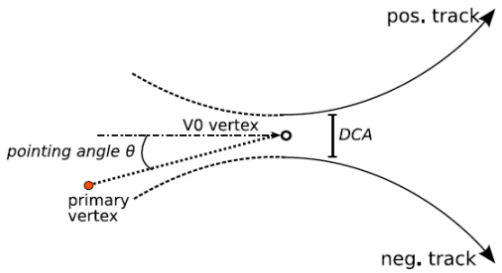


Figure 4.3: Demonstration of pointing angle cut. [52]

To make sure that the reconstruction efficiency and acceptance are properly evaluated, it is crucial to investigate the distribution of the cut variables in data and Monte Carlo (MC) such as EPOS [53, 54] and PYTHIA [20]. The EPOS event generator [54] was used to evaluate the efficiency and acceptance. It is a phenomenological approach that based on the parton model [53]. Comparison plots for the distribution of cut variables of $V^0$s in data and MC are shown in Fig. 4.4 and Fig. 4.5. These comparison plots are from pp collisions.

[2] $c\tau(\mathrm{K}^0_\mathrm{S}) = 2.69\ cm$, $c\tau(\Lambda) = 7.89\ cm$.

Similar studies have been done for pPb collisions as well. These plots show that the cut variables used in $V^0$ reconstruction in data and MC are in good agreement.

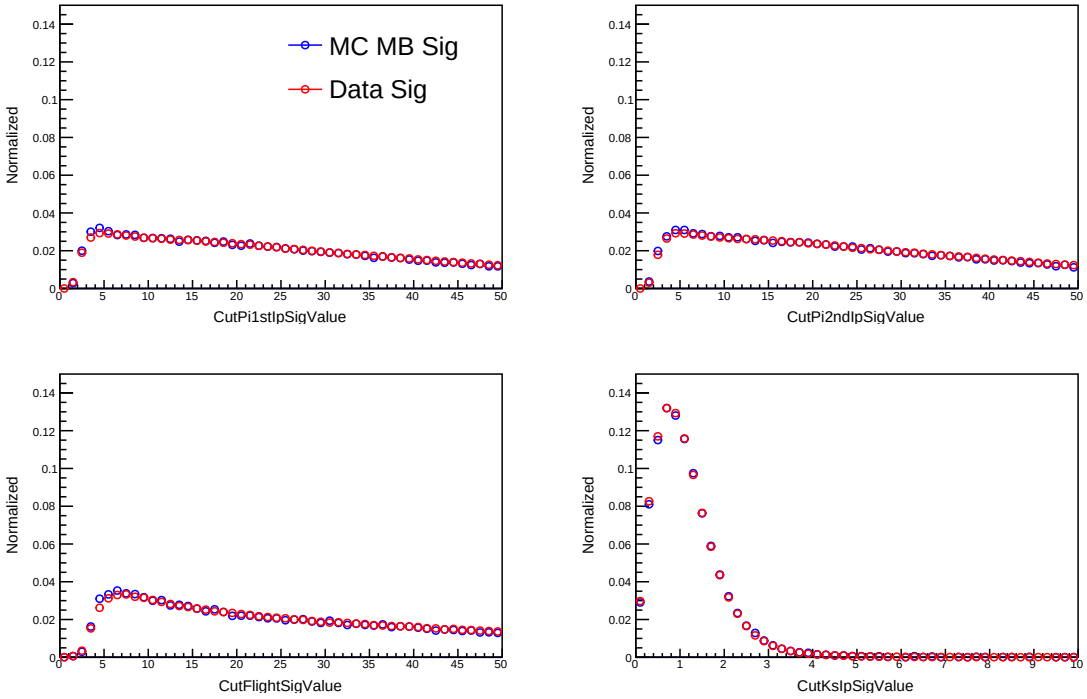


Figure 4.4: Cut variables of $K^0_S$ in pp data and pp EPOS: normalized distributions of $\pi^+$ (top left) and $\pi^-$ (top right) track 3D distance of closest approach significance with respect to primary vertex, distribution of the 3D vertex separation significance between $V^0$ vertex and primary vertex (bottom left), and $V^0$ candidates 3D distance of closest approach significance with respect to primary vertex (bottom right). Red circles represent pp data, while blue circles stand for pp EPOS.

### 4.1.2 Reconstruction of $\Xi^-$ and $\Omega^-$ candidates

To reconstruct $\Xi^-$ and $\Omega^-$ candidates, an extra charged track with the correct sign is combined with a previously reconstructed $\Lambda$ candidate to form a good secondary vertex with an appropriate invariant mass. To reduce background, cut criteria for $\Xi^-$ ($\Omega^-$) candidates reconstruction are summarized below:

- 3D distance of closest approach significance of proton track from $\Lambda$ decay with re-

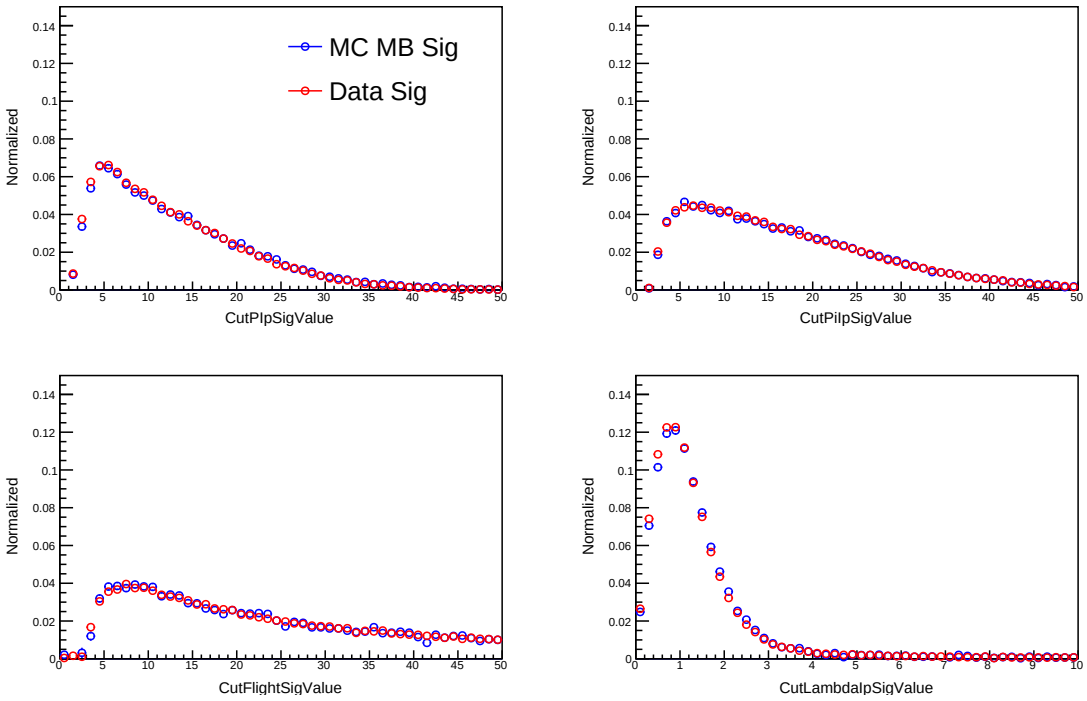


Figure 4.5: Cut variables of $\Lambda$ in pp data and pp EPOS: normalized distributions of proton (top left) and $\pi^-$ (top right) track 3D distance of closest approach significance with respect to primary vertex, distribution of the 3D vertex separation significance between $V^0$ vertex and primary vertex (bottom left), and $V^0$ candidates 3D distance of closest approach significance with respect to primary vertex (bottom right). Red circles represent pp data, while blue circles stand for pp EPOS.

spect to the primary vertex $> 2$

- 3D distance of closest approach significance of $\pi$ track from $\Lambda$ decay with respect to the primary vertex $> 3$ [3]

- 3D distance of closest approach significance of $\pi$ (K) track from $\Xi^-$ ($\Omega^-$) decay with respect to the primary vertex $> 4$

- 3D distance of closest approach significance of the $\Xi^-$ ($\Omega^-$) candidate with respect to the primary vertex $< 3$

[3] Comparing to proton track, the momentum of $\pi$ track is smaller, thus DCA significance of $\pi$ track is larger.

- 3D separation significance between $\Lambda$ vertex and primary vertex $> 10$
- 3D separation significance between $\Xi^-$ ($\Omega^-$) vertex and primary vertex $> 2$

The cut variables used for $\Xi^-$ reconstruction mentioned above are identical to the ones used in CMS publications: QCD-10-007 [50] and HIN-15-006 [51].

To make sure that the reconstruction efficiency and acceptance are properly evaluated, it is crucial to investigate the distribution of cut variables in data and MC. Comparison plots for cut variables distribution of $\Xi^-$ and $\Omega^-$ candidates in data and MC are shown in Fig. 4.6 and Fig. 4.7 for pp collisions. Similar studies have been done for pPb collisions as well. These plots show that cut variables used in $\Xi^-$ and $\Omega^-$ reconstruction in data and MC are in good agreement.

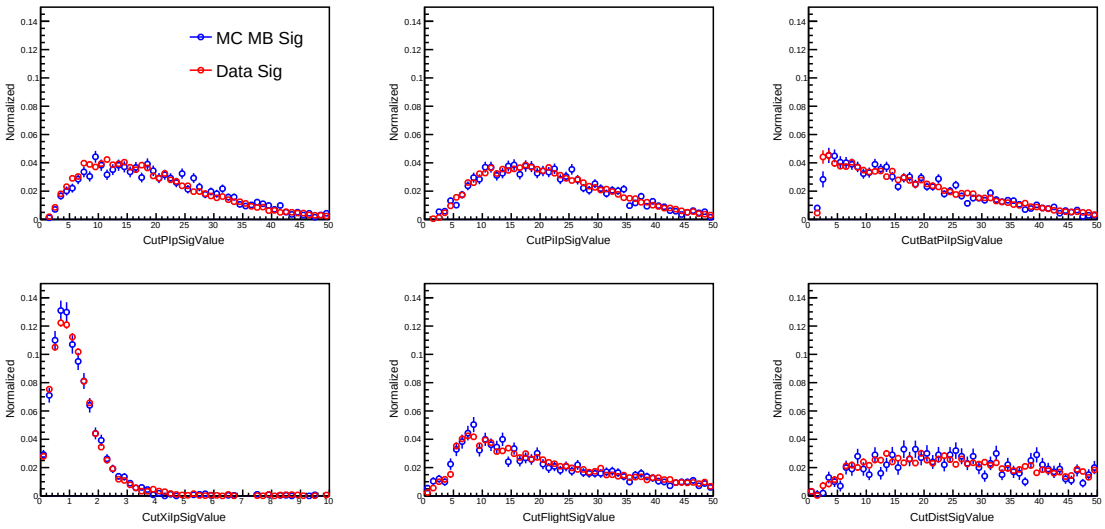


Figure 4.6: Cut variables of $\Xi^-$ in pp data and pp EPOS: normalized distributions of proton track from $\Lambda$ decay (top left), $\pi^-$ track from $\Lambda$ decay (top middle), and bachelor $\pi^-$ track (top right) 3D distance of closest approach significance with respect to primary vertex, $\Xi^-$ candidates 3D distance of closest approach significance with respect to primary vertex (bottom left), distribution of the 3D vertex separation significance between $\Xi^-$ vertex and primary vertex (bottom middle), and distribution of the 3D vertex separation significance between $\Lambda$ vertex and primary vertex (bottom right). Red circles represent pp data, while blue circles stand for pp EPOS.

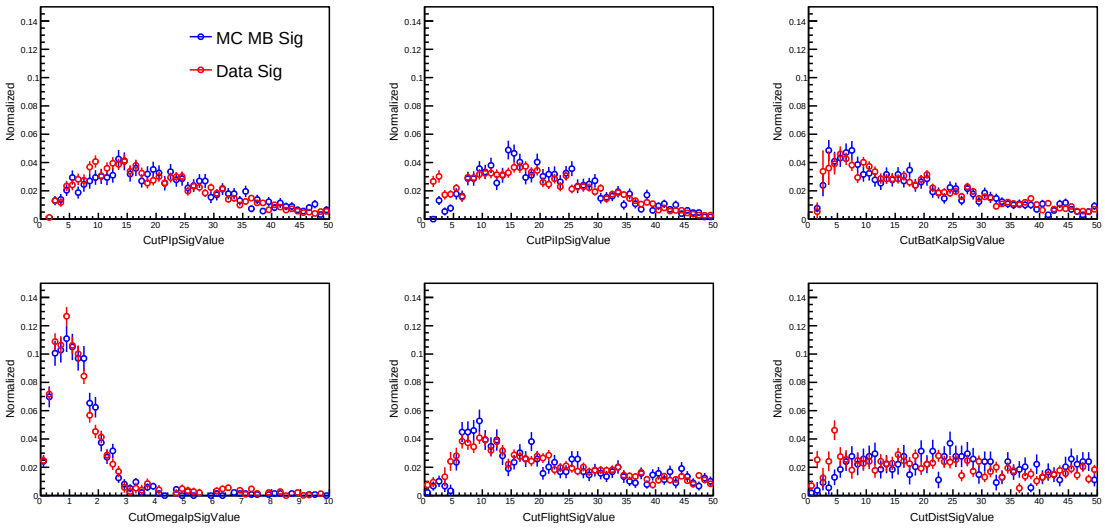


Figure 4.7: Cut variables of $\Omega^-$ in pp data and pp EPOS: normalized distributions of proton track from $\Lambda$ decay (top left), $\pi^-$ track from $\Lambda$ decay (top middle), and bachelor $K^-$ track (top right) 3D distance of closest approach significance with respect to primary vertex, $\Omega^-$ candidates 3D distance of closest approach significance with respect to primary vertex (bottom left), distribution of the 3D vertex separation significance between the $\Omega^-$ vertex and the primary vertex (bottom middle), and distribution of the 3D vertex separation significance between the $\Lambda$ vertex and the primary vertex (bottom right). Red circles represent the pp data, while the blue circles stand for pp EPOS.

### 4.1.3 Removal of mis-identified candidates

As the identity of each track cannot be determined, the mass of each charged particle leaving a track in the detector has to be assumed depending on the identity of the $V^0$ candidate. It is possible that $\mathrm{K}^0_\mathrm{S}$ ($\Lambda$) candidates are mis-identified as $\Lambda$ ($\mathrm{K}^0_\mathrm{S}$) candidates. Especially, there is a high probability that a track assumed to be a proton in a $\Lambda$ candidate is actually a pion, due to the abundance of pions. To select a clean sample of $\mathrm{K}^0_\mathrm{S}$ and $\Lambda$, the Armenteros-Podolanski (A-P) plot [55] is investigated.

The A-P plot is a two-dimensional plot of transverse momentum ($p_\mathrm{T}$) of the oppositely charged decay products with respect to the $V^0$ candidates versus the longitudinal momentum asymmetry $\alpha = (p_L^+ - p_L^-)/(p_L^+ + p_L^-)$. Examples of A-P plot can be found in Fig. 4.8

and Fig. 4.9. The obtained distribution can be explained by the fact that the pair of pions from the $K^0_S$ decay have the same masses and therefore their momenta are distributed symmetrically on average (upper band), while the proton (anti-proton) in $\Lambda$ ($\overline{\Lambda}$) decay carries, on average, a larger portion of the total momentum and results in an asymmetric distribution (two lower bands).

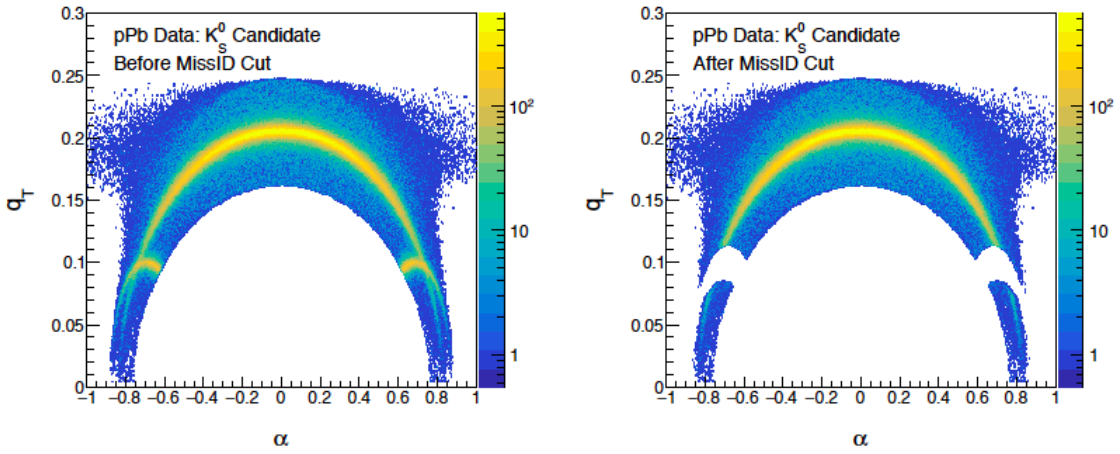


Figure 4.8: Armenteros-Podolanski(A-P) plot for $K^0_S$ candidates in pPb data before mis-identified mass cut (left) and after mis-identified mass cut (right).

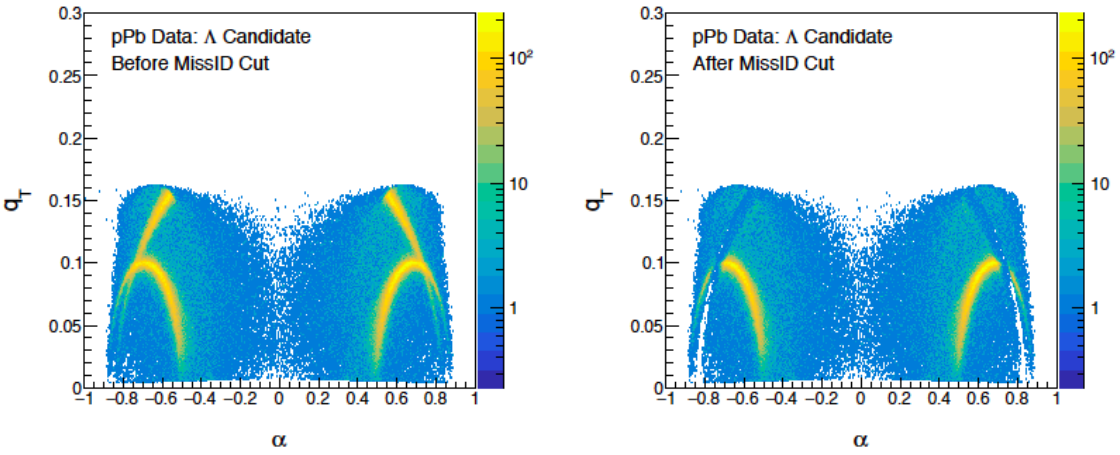


Figure 4.9: Armenteros-Podolanski(A-P) plot for $\Lambda$ candidates in pPb data before mis-identified mass cut (left) and after mis-identified mass cut (right).

To identify the mis-identified $K^0_S$, the $\pi - \pi$ hypothesis is applied to $\Lambda$ candidates. The

hypothesis assumes that both daughter tracks from the decay of $\Lambda$ candidates are pions and re-calculates the invariant mass of the decayed mother particle. Similar procedure is used to identify the mis-identified $\Lambda$ particles. The re-calculated invariant mass distribution for $K^0_S$ and $\Lambda$ in data and MC are shown in Fig. 4.10 for pPb collisions. Clear peaks at the present best experimental value of the $K^0_S$ ($\Lambda$) particle mass, as determined by the Particle Data Group (PDG) [34] mass value, 0.497614 (1.15683) GeV, can be seen the for re-calculated invariant mass peaks of $\Lambda$ ($K^0_S$) candidates. To remove those mis-identified $\Lambda$ ($K^0_S$), the re-calculated masses of the $K^0_S$ ($\Lambda$) candidates are required to be 10 (20) MeV away from the $\Lambda$ ($K^0_S$) PDG mass value. Effects of the cut can be seen on the right hand side of Fig. 4.8 and Fig. 4.9. With this cut, mis-identified band is completely removed, while only a tiny fraction of the real candidates are removed. A similar cut is needed for $\Omega^-$ candidates reconstruction to remove the mis-identified $\Xi^-$, due to the abundance of $\Xi^-$ candidates in comparison to the $\Omega^-$ candidates. The re-calculated mass of the $\Omega^-$ candidates is required to be 15 MeV away from the $\Xi^-$ PDG mass value. This procedure is not necessary for the $\Xi^-$ candidates, since the amount of $\Omega^-$ candidates is small in comparison to the $\Xi^-$ candidates.

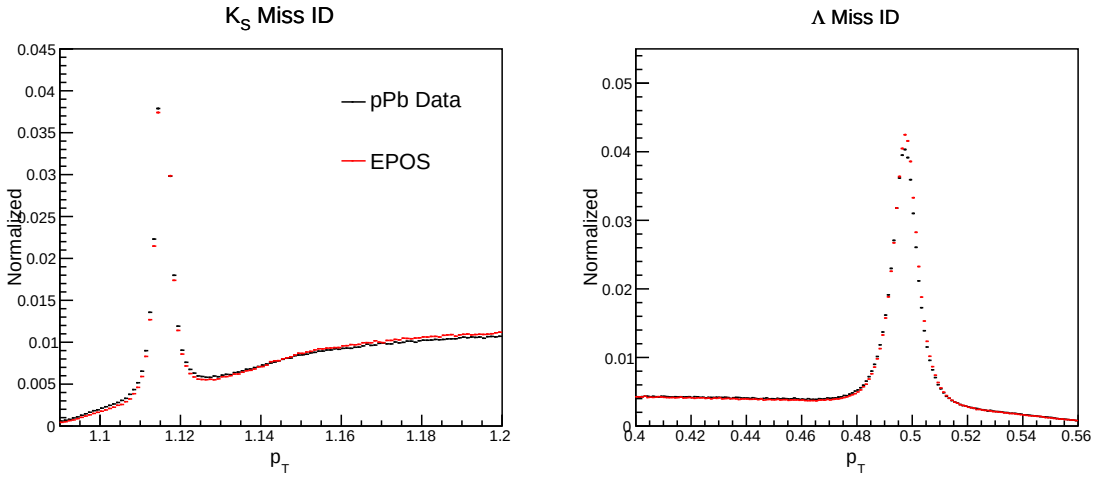


Figure 4.10: Re-calculated invariant mass in pPb : $K^0_S$ (left) and $\Lambda$ (right) for data (black) and pPb EPOS (red)

For $V^0$ candidates, there is also a chance that both of the daughter tracks are, in fact,

electrons from a photon conversion. Therefore, to remove the mis-identified photons, the re-calculated $V^0$ mass is required to be larger than 15 MeV.

## 4.2 Transverse momentum spectra

### 4.2.1 Yield extraction

The invariant mass distributions of the reconstructed $K^0_S$, $\Lambda$, $\Xi^-$, and $\Omega^-$ candidates in pPb collisions simulated by EPOS for differential $p_T$ bins are shown from Fig. 4.11 to Fig. 4.14. Only plots for the first several $p_T$ bins are shown as examples. To extract signal counts from the invariant mass distribution, a double Gaussian with a common mean is used for the signal function. To describe the background, a second-order polynomial is used to fit the background of $K^0_S$, while a function in the form $Aq^B$, where $q = m_{mother} - (m_{dau1} + m_{dau2})$, is used for the three strange baryon species. The mean values of the mass peaks from this fitting are close to the PDG values of particle masses, and the average standard deviat, $\sigma$, of the double Gaussian function is calculated as:

$$\sigma_{ave} = \sqrt{\frac{Y_1}{Y_1+Y_2}\sigma_1^2 + \frac{Y_2}{Y_1+Y_2}\sigma_2^2}, \tag{4.1}$$

where $\sigma_1(\sigma_2)$ and $Y_1(Y_2)$ are $\sigma$ and yield of first (second) Gaussian.

The fittings are performed using the RooFit [56] package in ROOT [57]. The raw yield is given by the integral of the signal function for the entire mass range.

Once the invariant mass peaks are fitted with background and signal functions, the signal counts can be obtained by integrating the signal function over the full mass range.

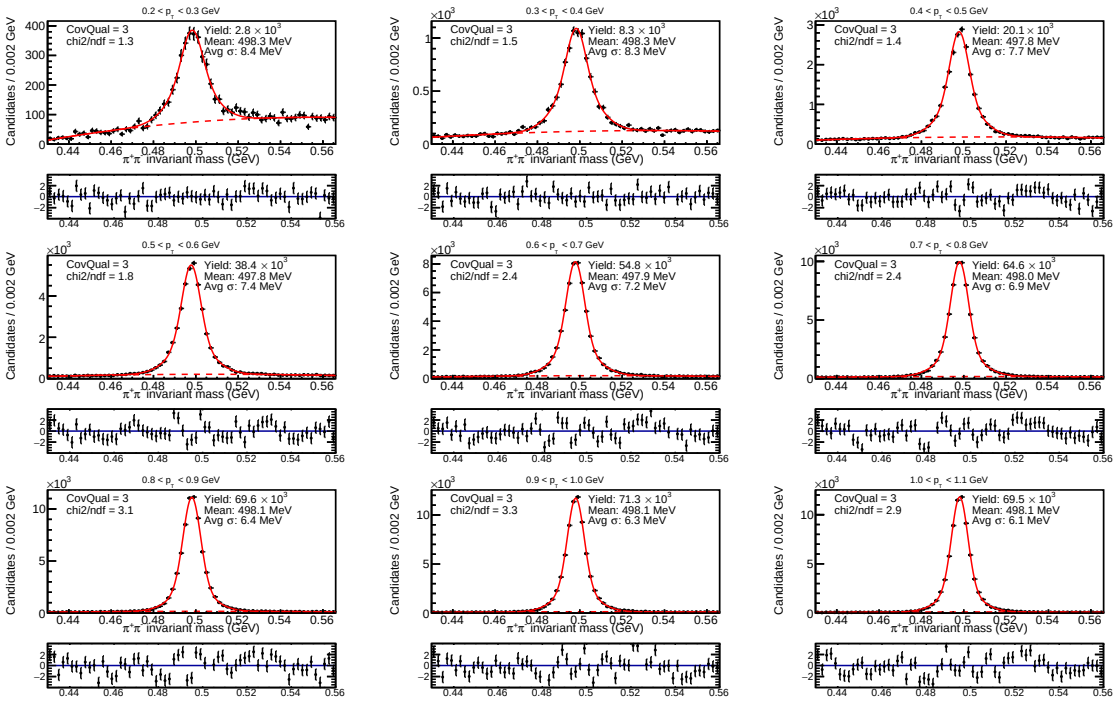


Figure 4.11: Samples of invariant mass distributions for $K^0_S$ in pPb collisions simulated by EPOS after applying cut criteria mentioned above. Pull plots are also provided. "Pull" is defined as the difference between the histogram value and the fitting value normalized by the histogram error.

### 4.2.2 Efficiency corrections

The performance of reconstructing $K^0_S$, $\Lambda$, $\Xi^-$, and $\Omega^-$ candidates is evaluated based on MC simulations. The efficiency $\times$ acceptance is calculated as follows:

$$\alpha \times \varepsilon = \frac{N^{\mathrm{RECO}}_{\mathrm{y,p_T,allcuts}}}{N^{\mathrm{GEN}}_{\mathrm{y,p_T}}} \tag{4.2}$$

where the ratio between reconstruction level (RECO) number of candidates and that from the generated level (GEN) is calculated in each $p_{\mathrm{T}}$ and center-of-mass rapidity ($y_{CM}$) interval for pp and pPb collision separately. With the above correction, the branching ratio and detector acceptance are also taken into account.

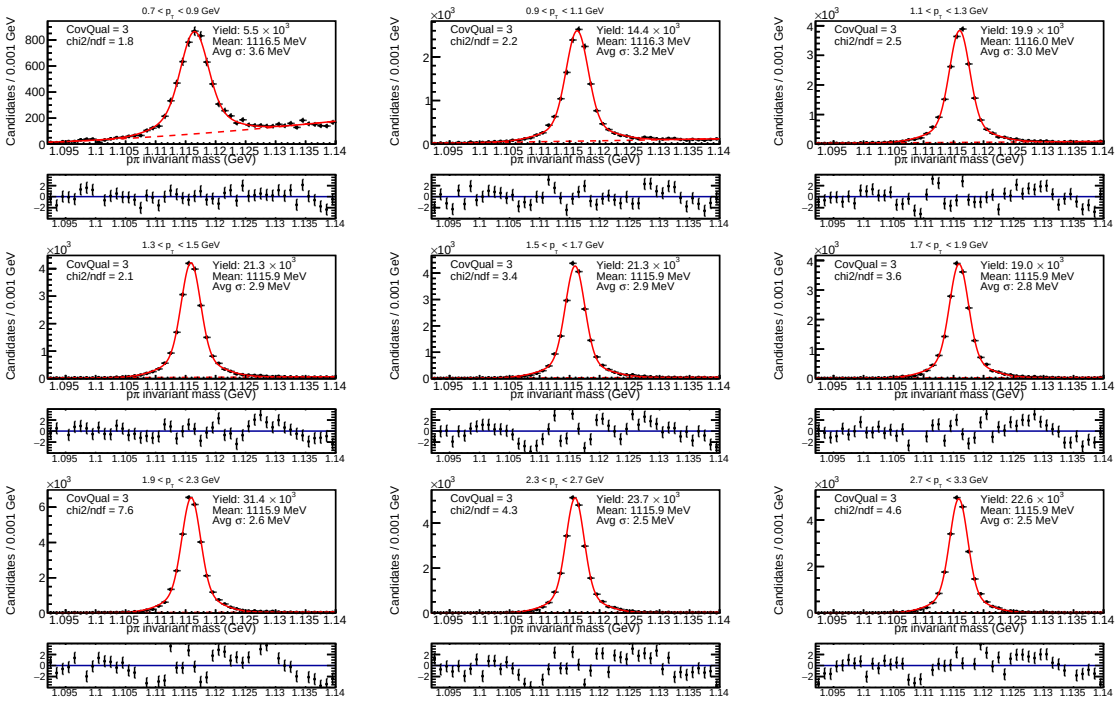


Figure 4.12: Samples of invariant mass distributions for Λ in pPb EPOS after applying cut criteria mentioned above. Pull plots are also provided.

Due to the fact that the z coordinate of the position of primary vertex (vertex z) could have a large effect on particle reconstruction, it is essential ensure that the collision z-vertex distributions are the same in the data and in the MC. If this turns out not to be the case, the vertex z distribution of the MC is reweighted it the same as in the data. The reweighting factor is derived as follows: First we fit vertex z distribution of the data and the MC with Gaussian function separately; then we take ratio of the two Gaussian functions (data over MC); after getting the ratio, reweighting factors are obtained according to the vertex z value of a certain event in MC. The vertex z reweighting for MC is shown in following plots. Fig.4.15 shows the vertex z distribution of pp data, PYTHIA before and after vertex z reweighting. From the plot, it is clear that the reweighting procedure matches vertex z distribution in PYTHIA to that in data. The vertex z reweighting is done for pp EPOS and pPb EPOS as well, which is shown in Fig.4.16 and Fig.4.17.

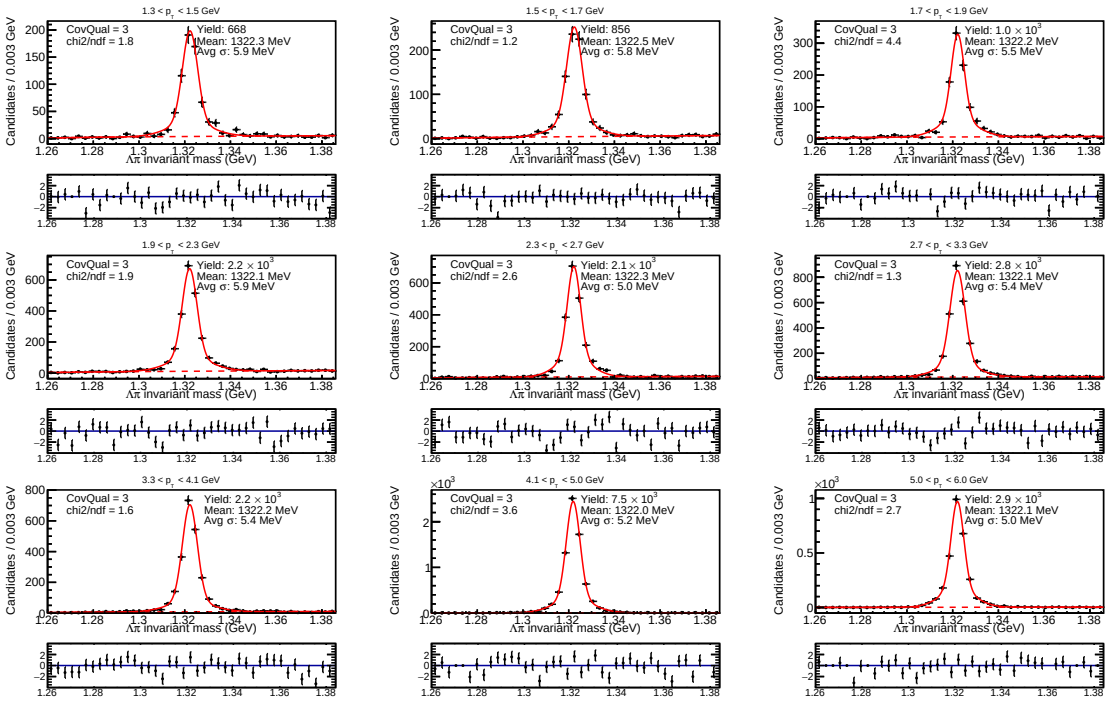


Figure 4.13: Samples of invariant mass distributions for $\Xi^-$ in pPb EPOS after applying cut criteria mentioned above. Pull plots are also provided.

Three different approaches can be deployed to get RECO level number of candidates:

1. fit the invariant mass peak and integrate the signal function to get signal counts, as what is done for data;

2. count the number of candidates within [peak$-3\sigma$, peak$+3\sigma$] mass window to estimate the total counts ($y_{tot}$) and use the sum of counts in [peak$-7\sigma$, peak$-4\sigma$] and [peak$+4\sigma$, peak$+7\sigma$] to estimate the background counts ($y_{bkg}$), then the signal counts equals $y_{tot} - y_{bkg}$;

3. match reconstructed strange particle candidates to generated strange particle candidates, as what is done in previous CMS publication, QCD-10-007 [50]. Due to the long lifetime of $K^0_S$, $\Lambda$, $\Xi^-$, and $\Omega^-$, these particles are decayed by GEANT4 [58] rather than generators and are not normally stored in the "GenParticles" collec-

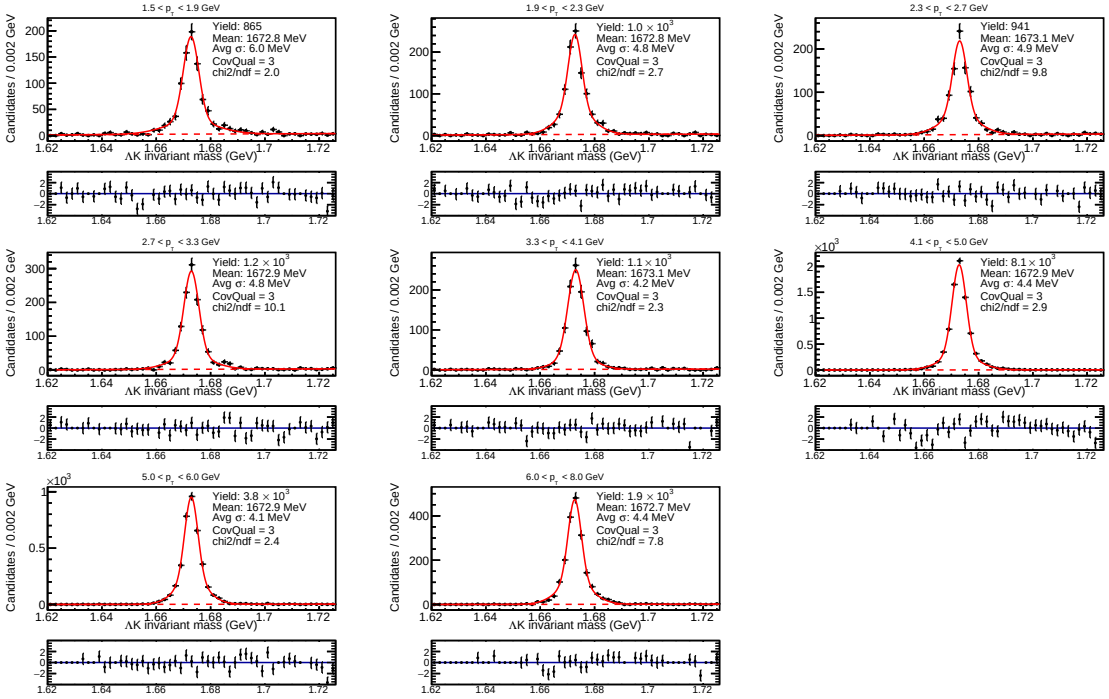


Figure 4.14: Samples of invariant mass distributions for $\Omega^-$ in pPb EPOS after applying cut criteria mentioned above. Pull plots are also provided.

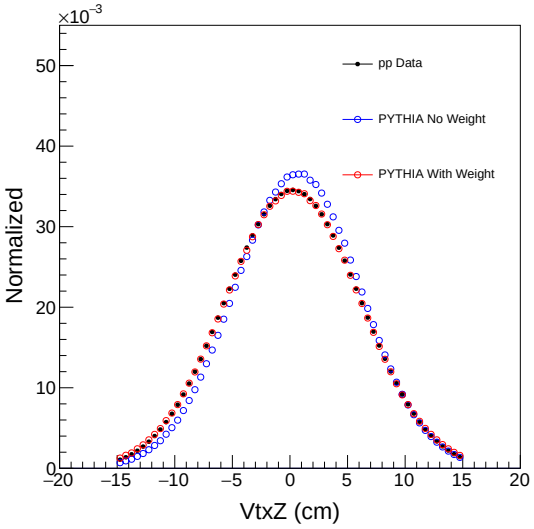


Figure 4.15: Vertex z reweighting for PYTHIA: black dots stand for vertex z distribution of pp data; blue circles represent vertex z distribution of PYTHIA before vertex z reweighting; red circles show vertex z distribution of PYTHIA after vertex z reweighting.

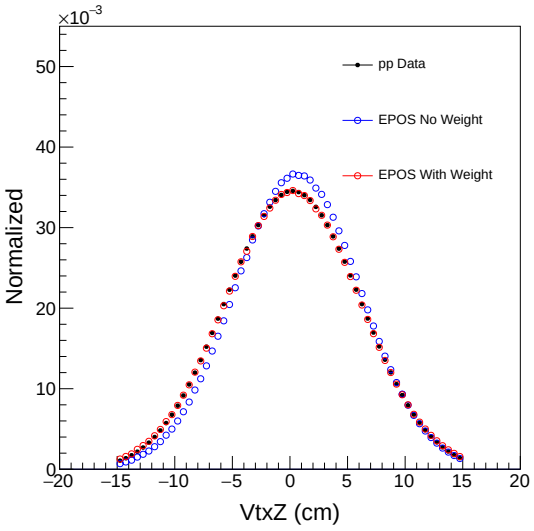


Figure 4.16: Vertex z reweighting for pp EPOS: black dots stand for vertex z distribution of pp data; blue circles represent vertex z distribution of pp EPOS before vertex z reweighting; red circles show vertex z distribution of pp EPOS after vertex z reweighting.

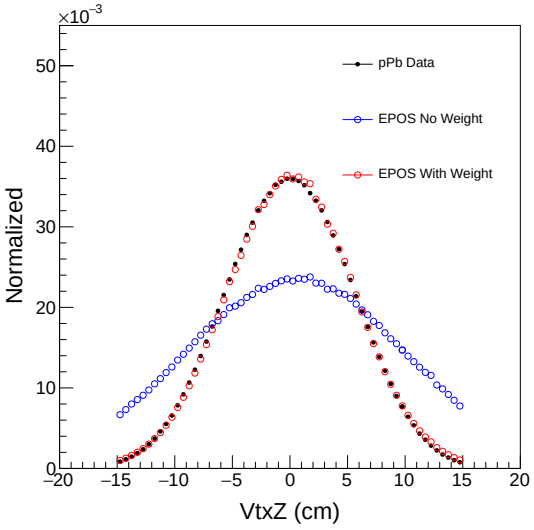


Figure 4.17: Vertex z reweighting for pPb EPOS: black dots stand for vertex z distribution of pPb data; blue circles represent vertex z distribution of pPb EPOS before vertex z reweighting; red circles show vertex z distribution of pPb EPOS after vertex z reweighting.

tion [59]. The "GenPlusSimParticleProducer" [60] is used to produce a new collection with both generator and GEANT4 particles.

For $V^0$ candidates, the matching criteria are:

- Each reconstructed track must be matched to the proper generated track by requiring $\Delta R < 0.1$ where $\Delta R = \sqrt{(\Delta\phi)^2 + (\Delta\eta)^2}$
- The distance between the reconstructed $V^0$ vertex and the true reconstructed vertex($\Delta$L) must be smaller than 10 *cm*

Note that the $\Delta$R matching is performed using the track parameters at the location of the $V^0$ vertex.

For $\Xi^-$ and $\Omega^-$ candidates, the matching criteria are:

- Each reconstructed track must be matched to the proper generated track by requiring $\Delta R < 0.05$
- The distance between the reconstructed $\Xi^-$ or $\Omega^-$ vertex and the true reconstructed vertex($\Delta$L) must be smaller than 5 *cm*

Fig.4.18 shows the difference of the yields obtained with the three different methods in the pPb EPOS MC sample. The full integral of the signal fitting function is the nominal method used in this analysis. The efficiency plots shown below are obtained with this method. The side-band method to estimate the background shows some difference to the nominal method only at low $p_{\mathrm{T}}$. This is expected, as the side-band method is equivalent as assuming the background shape around the invariant mass peak can be described with a linear function. The small discrepancy between the matching method and the nominal one is also expected, as the signal counts obtained with the matching method depend on the matching criteria. Overall, the three methods show consistent results within 5% for all particles.

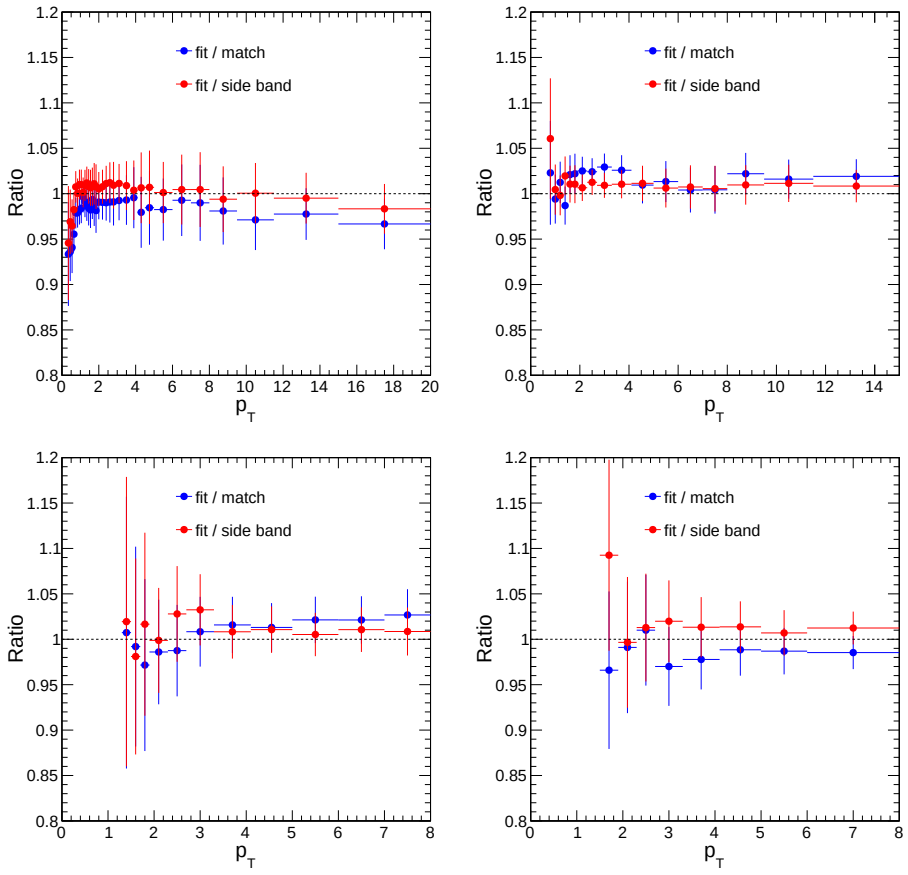


Figure 4.18: Ratio of RECO yields obtained with matching of RECO to GEN (blue dots) and direct counting of the number of candidates under the mass peak within $\pm 3\sigma$ using side band to estimate the number of candidates in background (red dots) to RECO yields obtained with full integral of the fitting double Gaussian function for different particles: $K^0_S$ (top left), $\Lambda$ (top right), $\Xi^-$ (bottom left), and $\Omega^-$ (bottom right) as a function of $p_T$ in $|y_{CM}| < 1.8$ derived from pPb EPOS.

At the RECO level, the same cut criteria as data are used. Also, the vertex z distribution is properly weighted for each event to match that of data. Efficiency $\times$ Acceptance of $K^0_S$ as a function of $p_T$ in several $y_{CM}$ bins for pp and pPb collisions are shown from Fig. 4.19 to Fig .4.21. Due to statistic limitations of the MC samples, Efficiency$\times$Acceptance may have some uneven structure. In this case, a fourth order polynomial function is used to smoothen out the Efficiency$\times$Acceptance. The smoothed Efficiency$\times$Acceptance of $K^0_S$ particles as a function of $p_T$ in several $y_{CM}$ bins for pp and pPb [4] collisions are shown from Fig.4.22

[4]In the middle of the 2013 pPb data taking, the direction of beam was reversed. Thus, there are two sets

to Fig.4.24. Similar efficiency tables are studied for other strange hadrons as well. The smoothed Efficiency×Acceptance of $\Lambda$, $\Xi^-$, and $\Omega^-$ particles in pp collisions are shown from Fig. 4.25 to Fig. 4.27 as examples.

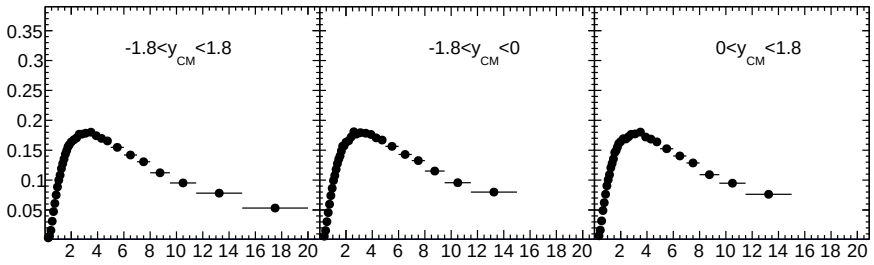


Figure 4.19: Efficiency × Acceptance of $K^0_S$ as a function of $p_T$ in several $|y_{CM}|$ bins as described in each plot derived from pp EPOS.

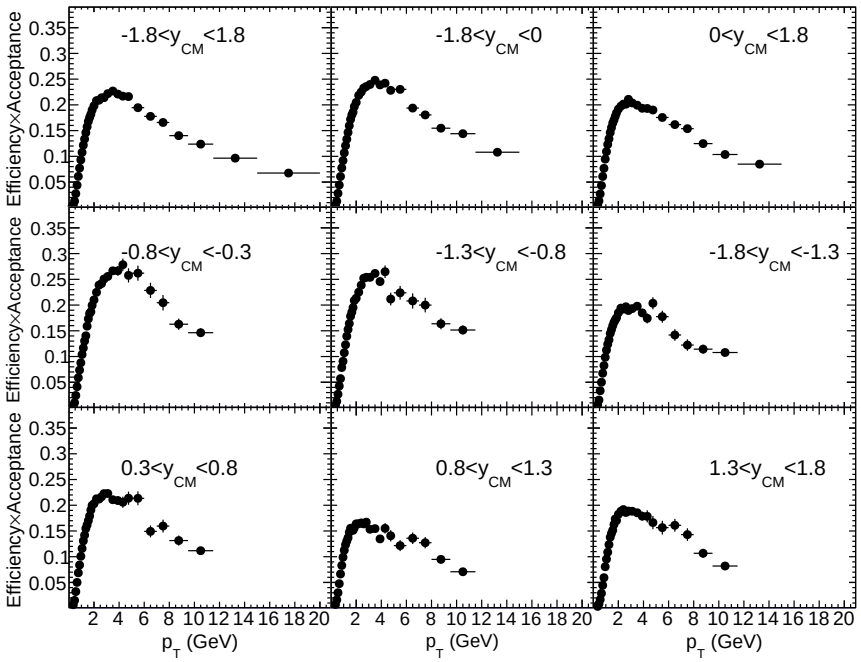


Figure 4.20: Efficiency × Acceptance of $K^0_S$ as a function of $p_T$ in several $|y_{CM}|$ bins as described in each plot derived from pPb EPOS with proton goes to the negative z direction.

The raw yields of strange particles are corrected for branching ratio (BR), acceptance ($\alpha$),

of efficiency tables for pPb data.

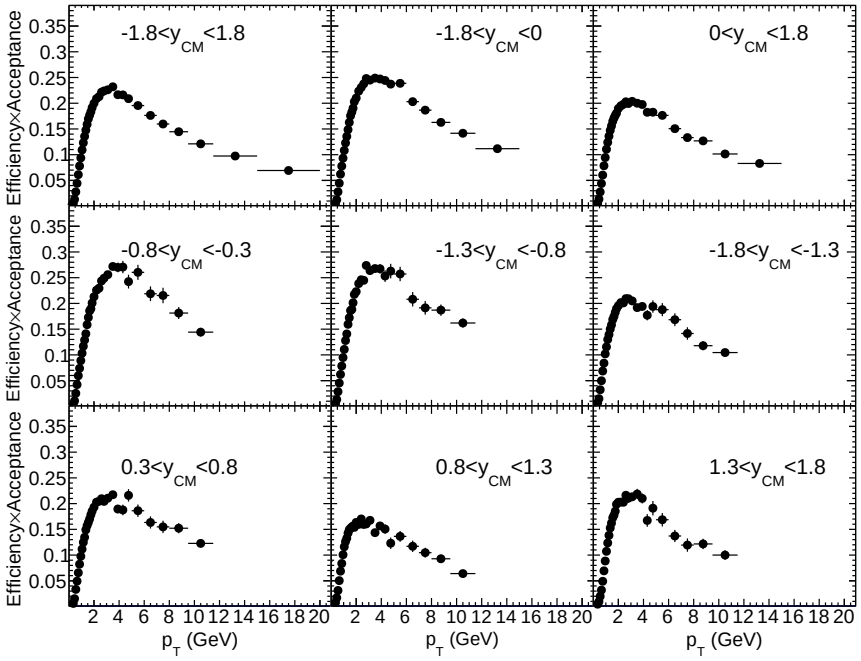


Figure 4.21: Efficiency $\times$ Acceptance of $K^0_S$ as a function of $p_T$ in several $|y_{CM}|$ bins as described in each plot derived from pPb EPOS with proton goes to the positive z direction.

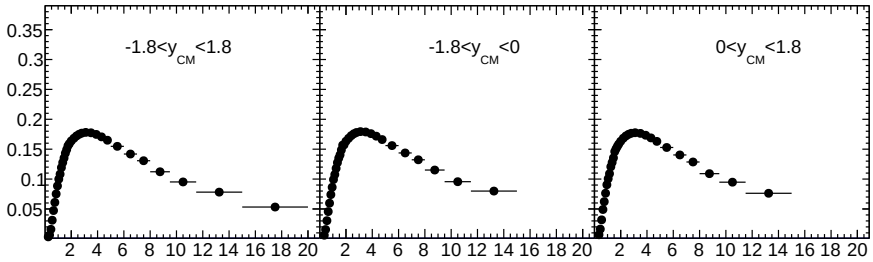


Figure 4.22: Smoothed Efficiency $\times$ Acceptance of $K^0_S$ as a function of $p_T$ in several $|y_{CM}|$ bins as described in each plot derived from pp EPOS.

and reconstruction efficiency ($\varepsilon$) using simulation, based on the EPOS generator and a GEANT4 model of the detector,

$$N^{\text{corr}}_{K^0_S/\Lambda/\Xi^-/\Omega^-} = \frac{N^{\text{raw}}_{K^0_S/\Lambda/\Xi^-/\Omega^-}}{\text{BR} \times \alpha \times \varepsilon} \tag{4.3}$$

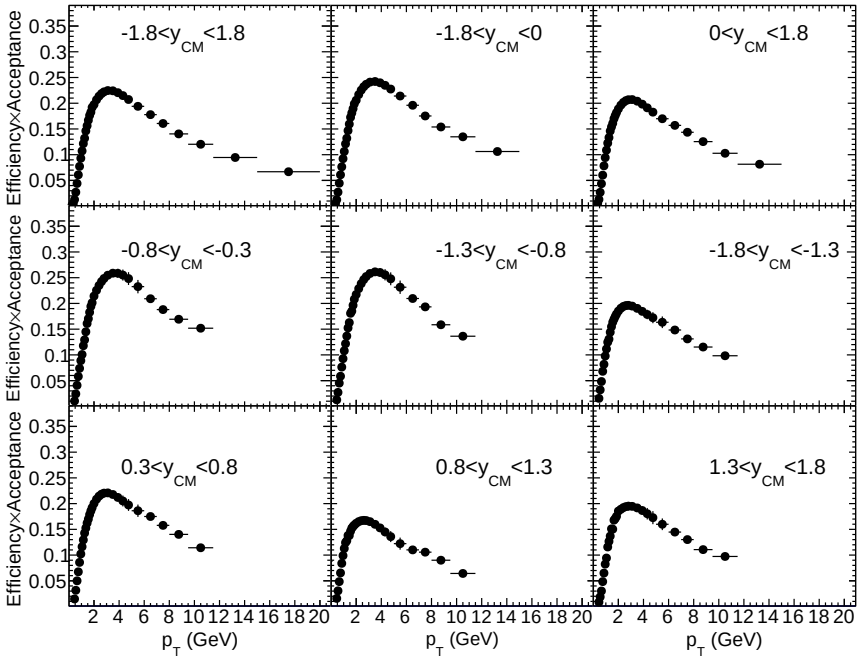


Figure 4.23: Smoothed Efficiency $\times$ Acceptance of $K^0_S$ as a function of $p_T$ in several $|y_{CM}|$ bins as described in each plot derived from pPb EPOS with proton goes to the negative z direction.

where BR $\times\, \alpha \times \varepsilon$ is obtained by the ratio of raw reconstructed yield to generated yield of strange particles in MC simulations. $N^{\rm raw}_{K^0_S/\Lambda/\Xi^-/\Omega^-}$ and $N^{\rm corr}_{K^0_S/\Lambda/\Xi^-/\Omega^-}$ represent the yield of strange particles before and after corrections.

### 4.2.3 Feed-down correction of $\Lambda$ candidates

The raw yield of $\Lambda$ candidates contains a contribution from decays of $\Xi^-$ and $\Omega^-$ particles. This "non-prompt" contribution is largely determined by the ratio of $\Xi^-$ to $\Lambda$ candidate yield ($\Omega^-$ candidate yield is negligible, in comparison to the yield of $\Xi^-$ candidates). Although tight cuts on the 3D distance of closest approach significance of $\Lambda$ candidates with respect to the primary vertex help remove a large fraction of non-prompt $\Lambda$ candidates, up to 4% non-prompt $\Lambda$ could still remain in the $\Lambda$ candidate sample at intermediate $p_T$. If the

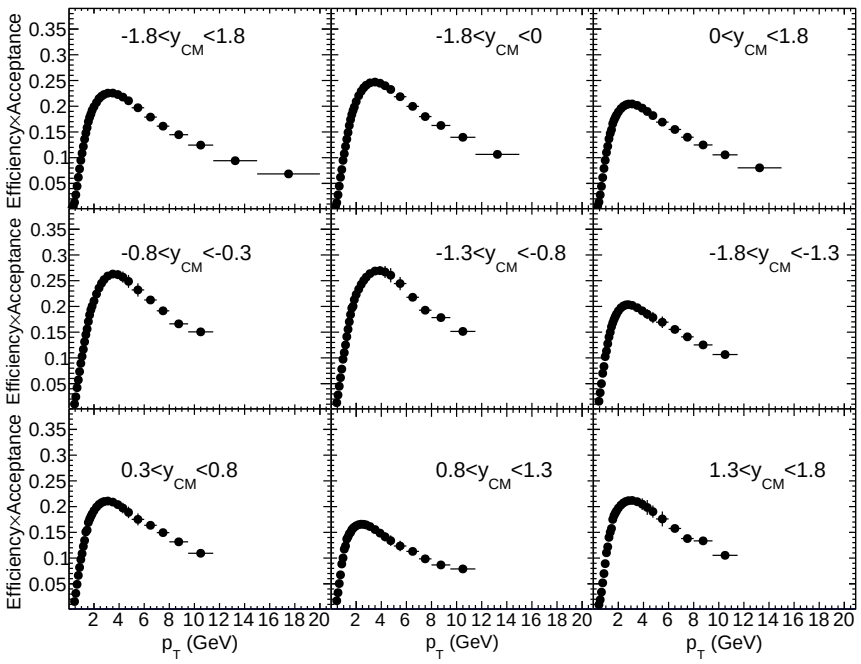


Figure 4.24: Smoothed Efficiency $\times$ Acceptance of $K^0_S$ as a function of $p_T$ in several $|y_{CM}|$ bins as described in each plot derived from pPb EPOS with proton goes to the positive z direction.

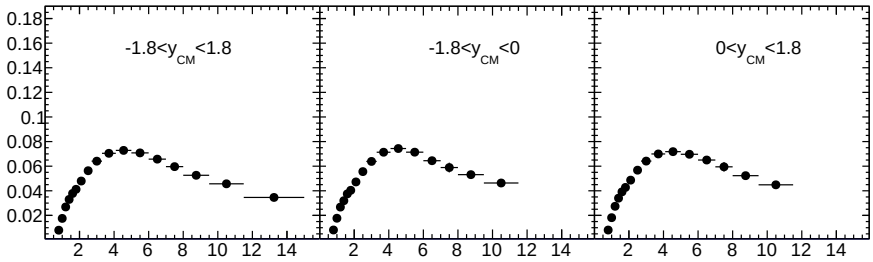


Figure 4.25: Smoothed Efficiency $\times$ Acceptance of $\Lambda$ as a function of $p_T$ in several $|y_{CM}|$ bins as described in each plot derived from pp EPOS.

ratio of $\Xi^-$ to $\Lambda$ yield is modeled precisely in simulations, contamination of non-prompt $\Lambda$ candidates will be corrected in the correction procedure using Eq. 4.3. Otherwise, an additional correction for the residual effect is necessary. As the $\Xi^-$ candidate yield is explicitly measured in this analysis. The residual correction factor can be derived in a data-driven

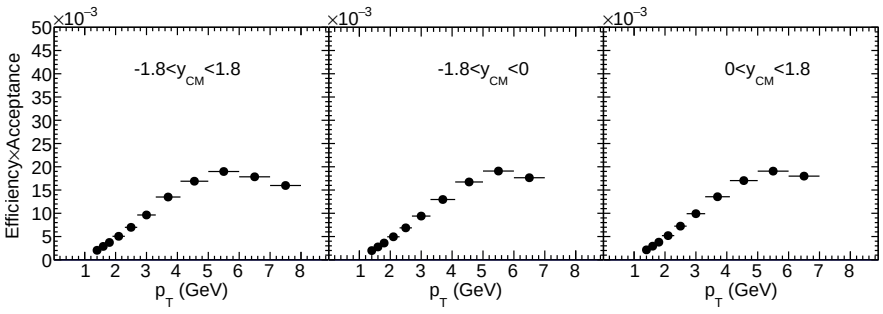


Figure 4.26: Smoothed Efficiency × Acceptance of $\Xi^-$ as a function of $p_{\mathrm{T}}$ in several $|y_{CM}|$ bins as described in each plot derived from pp EPOS.

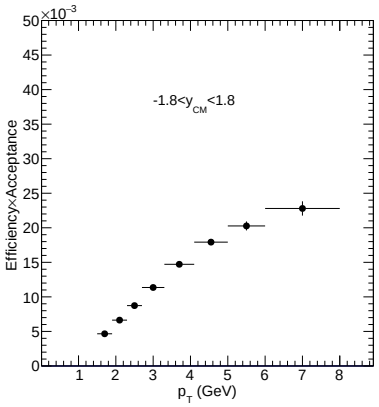


Figure 4.27: Smoothed Efficiency × Acceptance of $\Lambda$ as a function of $p_{\mathrm{T}}$ for $|y_{CM}| < 1.8$ derived from pp EPOS.

way as:

$$f_{\Lambda,np}^{\text{residual}} = 1 + f_{\Lambda,np}^{raw} \times \left( \frac{N_{\Xi^-}^{\text{corr}}/N_{\Lambda}^{\text{corr}}}{N_{\Xi^-}^{\text{MC}}/N_{\Lambda}^{\text{MC}}} - 1 \right), \tag{4.4}$$

where $f_{\Lambda,np}^{raw}$ denotes the fraction of non-prompt $\Lambda$ in the raw reconstructed $\Lambda$ sample, and is obtained from MC simulations. $N_{\Xi^-}^{\text{corr}}/N_{\Lambda}^{\text{corr}}$ and $N_{\Xi^-}^{\text{MC}}/N_{\Lambda}^{\text{MC}}$ are the $\Xi^-$-to-$\Lambda$ ratios from the data after applying corrections in Eq. 4.3, and from generator-level MC simulations, respectively. The final prompt $\Lambda$ particle yield is obtained after dividing by this residual

factor, $f_{\Lambda,np}^{\text{residual}}$. The effect from residual non-prompt $\Lambda$ particles is negligible when the EPOS event generator is used, since it has a similar $\Xi^-/\Lambda$ ratio as in the data. In the nominal results presented here, the EPOS event generator is used and in this case, the residual correction is negligible. However, for crosscheck purpose, other event generators, PYTHIA or HIJING [61], are also used to test the residual correction. Note that $N_{\Lambda}^{\text{corr}}$ used in Eq. 4.4 is first derived using Eq. 4.3, which, in principle, still contains the residual non-prompt $\Lambda$ particles. Therefore, by applying Eq. 4.4 iteratively, $N_{\Lambda}^{\text{corr}}$ will approach the final corrected yields for prompt-only $\Lambda$ particles. Studies showed that a second iteration of this correction has an effect of less than 0.1% on the spectra.

### 4.2.4 Normalization

In pp collisions, the differential invariant cross section ($\frac{1}{N_{\text{evt}}} E \frac{d^3\sigma}{d^3p}$) is used to represent particle production, where $N_{\text{evt}}$ is number of events. It can be transformed to measurable quantities based on following equation:

$$\frac{1}{N_{\text{evt}}} E \frac{d^3\sigma}{d^3p} = \frac{1}{N_{\text{evt}}} \frac{d^2\sigma}{2\pi p_{\text{T}} dp_{\text{T}} dy} \tag{4.5}$$

In pPb collision, per-event yield ($\frac{1}{N_{\text{evt}}} E \frac{d^3N}{d^3p}$) is used to represent particle production. It can be measured based on following equation:

$$\frac{1}{N_{\text{evt}}} E \frac{d^3N}{d^3p} = \frac{1}{N_{\text{evt}}} \frac{d^2N}{2\pi p_{\text{T}} dp_{\text{T}} dy} \tag{4.6}$$

For direct comparison, a factor of 70 mb [62] can be used to scale the pp spectrum from a differential cross section to a per-event yield.

# Chapter 5

## Multiplicity dependence of strange hadron production

Usually, particle correlation measurements, such as elliptic flow ($v_2$) and triangular flow ($v_3$) [17, 63, 64, 65], are used to study the collectivity of the matter produced in the collisions. In this chapter, a new way to study the potential collective flow is introduced. To test whether the radial flow is there or not in the small systems, identified particle spectra can be used, since radial flow will push all the particles out at the same velocity, thus, particles with larger masses end up with larger momentum. Multiplicity dependent spectra of $K^0_S$, $\Lambda$, and $\Xi^-$ in pp, pPb, and PbPb collisions provide an ideal way to study radial flow in small systems.

### 5.1 Data samples and event selection

The pp, pPb, and PbPb data used are recorded by CMS in the year of 2010, 2013, and 2011, respectively. Monte Carlo (MC) samples of pp, pPb, and PbPb collisions are generated to determine the performance of strange hadron reconstruction, event selection efficiency and crosscheck other potential detector effects. For pp collisions, PYTHIA event generator is used to produce the MC sample. For pPb collision, both HIJING and EPOS event generators are used to produce the MC samples. For PbPb collision, since only the peripheral events are needed, HIJING event generator with requirement on the impact parameter (b) is used.

A key component for this analysis is to get enough statistics for high multiplicity events in both pp and pPb collisions. With the goal of studying the properties of high multiplicity pp and pPb collisions, dedicated high multiplicity triggers were designed and implemented.

Fig. 5.1 shows $N_{\mathrm{trk}}^{\mathrm{offline}}$ distribution of minimum bias and high multiplicity triggers in pPb collisions. In this analysis, $N_{\mathrm{trk}}^{\mathrm{offline}}$ is used to represent the multiplicity, and it is defined as the offline reconstructed tracks that were counted within the kinematic cuts of $|\eta| < 2.4$ and $p_{\mathrm{T}} > 0.4$ GeV/c, where $\eta$ is the pseudorapidity and $p_{\mathrm{T}}$ is the transverse momentum of the track.

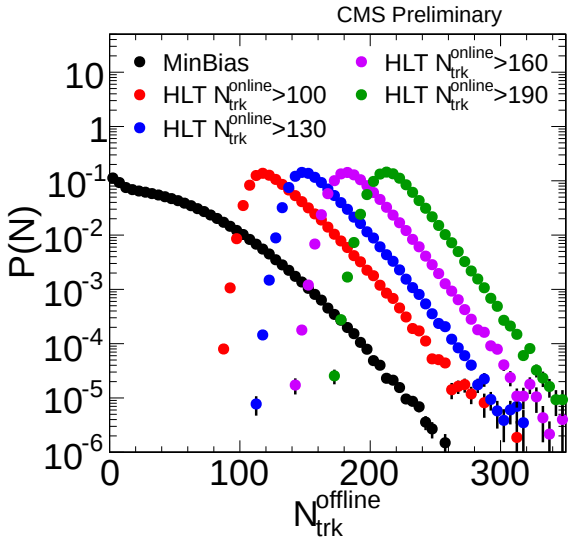


Figure 5.1: $N_{\mathrm{trk}}^{\mathrm{offline}}$ distribution of minimum bias and high multiplicity triggers in pPb collisions. [66]

The full track multiplicity range is divided into many different multiplicity bins: $[0,20)$, $[20,30)$, $[30,40)$, $[40,50)$, $[50,60)$, $[60,80)$, $[80,100)$, $[100,120)$, $[120,150)$, $[150,185)$, $[185,220)$, $[220,260)$, $[260,300)$, $[300,350)$. The faction of total number of events for each multiplicity interval, as well as the average track multiplicity before and after corrections, are summarized in Table 5.1 and Table 5.2 for pp and pPb collisions, respectively. The uncertainties on $\left\langle N_{\mathrm{trk}}^{\mathrm{corrected}} \right\rangle$ come from track quality cuts and from the tracking efficiency correction procedure, a total systematic uncertainty of 3.2%.

In order to compare the PbPb collisions with pp and pPb collisions directly, a subset of data from peripheral PbPb collisions were reanalyzed using the same track reconstruction algorithm as the one used in pp and pPb collisions. The selection of events and tracks is the

same as for the present pPb analysis although a different trigger is used. The average $N_{\mathrm{trk}}^{\mathrm{offline}}$ and $N_{\mathrm{trk}}^{\mathrm{corrected}}$ values, and corresponding average PbPb collision centrality, as determined by the total energy deposited in the HF calorimeters [67], are listed in Table 5.3 for each $N_{\mathrm{trk}}^{\mathrm{offline}}$ bin. Similarly, the uncertainties on $N_{\mathrm{trk}}^{\mathrm{corrected}}$ come from track quality cuts and from the tracking efficiency correction procedure, a total of 3.2%.

Table 5.1: Fraction of the full event sample in each multiplicity bin and the average multiplicity per bin for pp data. The multiplicity of offline reconstructed tracks, $N_{\mathrm{trk}}^{\mathrm{offline}}$, was counted within the kinematic cuts of $|\eta| < 2.4$ and $p_T > 0.4$ GeV/c. The third and forth columns list the average values of $N_{\mathrm{trk}}^{\mathrm{offline}}$ as well as the average of $N_{\mathrm{trk}}^{\mathrm{corrected}}$, the event multiplicity corrected for all detector and algorithm inefficiencies.

| Multiplicity bin ($N_{\mathrm{trk}}^{\mathrm{offline}}$) | Fraction | $\langle N_{\mathrm{trk}}^{\mathrm{offline}} \rangle$ | $\langle N_{\mathrm{trk}}^{\mathrm{corrected}} \rangle$ |
|---|---|---|---|
| $[0,35)$ | 0.93 | 13 | $14\pm1$ |
| $[35,60)$ | 0.06 | 43 | $51\pm2$ |
| $[60,90)$ | $6\times10^{-3}$ | 68 | $79\pm3$ |
| $[90,110)$ | $2\times10^{-4}$ | 96 | $111\pm4$ |
| $[110,130)$ | $1\times10^{-5}$ | 116 | $134\pm5$ |
| $[130,\infty)$ | $7\times10^{-7}$ | 138 | $161\pm6$ |

Table 5.2: Fraction of the full event sample in each multiplicity bin and the average multiplicity per bin for pPb data. The multiplicity of offline reconstructed tracks, $N_{\text{trk}}^{\text{offline}}$, was counted within the kinematic cuts of $|\eta| < 2.4$ and $p_T > 0.4$ GeV/c. The third and forth columns list the average values of $N_{\text{trk}}^{\text{offline}}$ as well as the average of $N_{\text{trk}}^{\text{corrected}}$, the event multiplicity corrected for all detector and algorithm inefficiencies.

| Multiplicity bin ($N_{\text{trk}}^{\text{offline}}$) | Fraction | $\langle N_{\text{trk}}^{\text{offline}} \rangle$ | $\langle N_{\text{trk}}^{\text{corrected}} \rangle$ |
|---|---|---|---|
| MB | 1.00 | 40 | 50±2 |
| $[0,20)$ | 0.31 | 10 | 12±1 |
| $[20,30)$ | 0.14 | 25 | 30±1 |
| $[30,40)$ | 0.12 | 35 | 42±2 |
| $[40,50)$ | 0.10 | 45 | 54±2 |
| $[50,60)$ | 0.09 | 54 | 66±3 |
| $[60,80)$ | 0.12 | 69 | 84±4 |
| $[80,100)$ | 0.07 | 89 | 108±5 |
| $[100,120)$ | 0.03 | 109 | 132±6 |
| $[120,150)$ | 0.02 | 132 | 159±7 |
| $[150,185)$ | $4\times10^{-3}$ | 162 | 195±9 |
| $[185,220)$ | $5\times10^{-4}$ | 196 | 236±10 |
| $[220,260)$ | $6\times10^{-5}$ | 232 | 280±12 |
| $[260,300)$ | $3\times10^{-6}$ | 271 | 328±14 |
| $[300,350)$ | $1\times10^{-7}$ | 311 | 374±16 |

Table 5.3: Average centrality under standard definition based on HF total energy in each multiplicity bin and the average multiplicity per bin for PbPb data. The multiplicity of offline reconstructed tracks, $N_{\text{trk}}^{\text{offline}}$, was counted within the kinematic cuts of $|\eta| < 2.4$ and $p_T > 0.4$ GeV/c. The third and forth columns list the average values of $N_{\text{trk}}^{\text{offline}}$ as well as the average of $N_{\text{trk}}^{\text{corrected}}$, the event multiplicity corrected for all detector and algorithm inefficiencies.

| Multiplicity bin ($N_{\text{trk}}^{\text{offline}}$) | <Centrality> ± RMS (%) | $\langle N_{\text{trk}}^{\text{offline}} \rangle$ | $\langle N_{\text{trk}}^{\text{corrected}} \rangle$ |
|---|---|---|---|
| $[0,20)$ | 92±4 | 10 | 13±1 |
| $[20,30)$ | 86±4 | 24 | 30±1 |
| $[30,40)$ | 83±4 | 34 | 43±2 |
| $[40,50)$ | 80±4 | 44 | 55±2 |
| $[50,60)$ | 78±3 | 54 | 68±3 |
| $[60,80)$ | 75±3 | 69 | 87±4 |
| $[80,100)$ | 72±3 | 89 | 112±5 |
| $[100,120)$ | 70±3 | 109 | 137±6 |
| $[120,150)$ | 67±3 | 134 | 168±7 |
| $[150,185)$ | 64±3 | 167 | 210±9 |
| $[185,220)$ | 62±2 | 202 | 253±11 |
| $[220,260)$ | 59±2 | 239 | 299±13 |
| $[260,300)$ | 57±2 | 279 | 350±15 |
| $[300,350)$ | 55±2 | 324 | 305±18 |

## 5.2 Systematics

The systematic uncertainties in pp, pPb, and PbPb collisions have been investigated, and no obvious multiplicity dependence has been observed among different multiplicity intervals for the measured strange particle spectra. Therefore, the same relative systematic uncertainties on the yields would be quoted for different multiplicity intervals. Due to this reason, only the multiplicity interval with the largest statistics for each system is used to perform the systematic study to reduce the effect of limited statistics. For some systematic sources, non-negligible $p_{\mathrm{T}}$ dependence has been observed. In this case, different systematic uncertainties are quoted for different $p_{\mathrm{T}}$ ranges. The total uncertainties in the particle yields are calculated by adding all the systematic sources in quadrature, assuming that they are independent. However, when we calculate the systematic uncertainty in the particle ratios some of the uncertainties that are common will cancel. Due to the fact that both $\mathrm{K}^0_{\mathrm{S}}$ and $\Lambda$ candidates are reconstructed by combining two tracks, the uncertainties from tracking efficiency [68] can be canceled out in $\Lambda$ over $\mathrm{K}^0_{\mathrm{S}}$ yield ratios. However, $\Xi^-$ candidates are reconstructed from three tracks, which means the systematic uncertainties from tracking efficiency will contribute 3.9% to $\Xi^-$ over $\Lambda$ ratios.

For each of the systematic sources, the ratios of invariant yields are calculated with various alternative conditions with respect to the default condition that is used in the analysis as a function of $p_{\mathrm{T}}$ for $\mathrm{K}^0_{\mathrm{S}}$, $\Lambda$, and $\Xi^-$. Then, the absolute values of maximum discrepancy in the ratio among various conditions for different $p_{\mathrm{T}}$ bins are fitted with a constant value, taking into account corresponding statistical uncertainties of each $p_{\mathrm{T}}$ bin. For those systematic sources that show clear $p_{\mathrm{T}}$ dependence, systematic values are quoted for low $p_{\mathrm{T}}$ and high $p_{\mathrm{T}}$ parts separately with the same technique described above. In the following subsections, each systematic uncertainty source is studied thoroughly for pp, pPb, and PbPb collisions, considering the length of this thesis, only some sample plots for pPb collision will be shown.

After carefully investigating all the systematic sources, no obvious system dependence has been seen, thus, for each systematic source, the same value is quoted for each collision system. Table 5.4 summarizes the different sources of systematic uncertainties of the $p_{\mathrm{T}}$ spectra in the mid-rapidity range for $\mathrm{K}^0_{\mathrm{S}}$, $\Lambda$, and $\Xi^-$.

Table 5.4: Summary of systematic uncertainties on $p_{\mathrm{T}}$ spectra in mid-rapidity for three collision systems.

| Source | $\mathrm{K}^0_{\mathrm{S}}$ (%) | | $\Lambda$ (%) | | $\Xi^-$ (%) |
|---|---|---|---|---|---|
| | $< 1.5$ GeV/c | $> 1.5$ GeV/c | $< 1.5$ GeV/c | $> 1.5$ GeV/c | |
| Pile-Up Effect( pp only) | 3 | 1 | 3 | 1 | 3 |
| Beam Direction( pPb only) | 3 | | 3 | | 4 |
| Efficiency Correction | | | | | 5 |
| Yield Extraction | 2 | | 2 | | 3 |
| Rapidity Binning | 1 | | 1 | | 2 |
| Selection Criteria | 3.6 | 2.2 | 3.6 | 2.2 | 7 |
| Momentum Resolution | 2 | | 2 | | |
| Tracking Efficiency | 7.8 | 7.8 | 7.8 | 7.8 | 11.7 |
| Feed-down Effect | | | 2 | 3 | |
| Total ( yields in pp ) | 9.6 | 8.7 | 9.8 | 8.9 | 15.3 |
| Total ( yields in pPb ) | 9.6 | 9.2 | 9.8 | 9.4 | 15.5 |
| Total ( yields in PbPb ) | 9.1 | 8.6 | 9.3 | 8.9 | 15.0 |
| | $< 1.5$ GeV/c | | $> 1.5$ GeV/c | | |
| Total ( $\Lambda/\mathrm{K}^0_{\mathrm{S}}$ ratios in pp ) | 8.1 | | 5.8 | | |
| Total ( $\Xi^-/\Lambda$ ratios in pp ) | 12.1 | | 11.4 | | |
| Total ( $\Lambda/\mathrm{K}^0_{\mathrm{S}}$ ratios in pPb ) | 8.1 | | 7.1 | | |
| Total ( $\Xi^-/\Lambda$ ratios in pPb ) | 12.4 | | 12.1 | | |
| Total ( $\Lambda/\mathrm{K}^0_{\mathrm{S}}$ ratios in PbPb ) | 6.9 | | 5.6 | | |
| Total ( $\Xi^-/\Lambda$ ratios in PbPb ) | 11.3 | | 11.0 | | |

Besides the systematic uncertainties on the spectra for each $p_{\mathrm{T}}$ bin, average transverse kinematic energy, $\langle m_{\mathrm{T}} \rangle - m$, of measured spectra is also studied. Due to the fact that the spectra for each particle species are not measured down to $p_{\mathrm{T}} = 0$ GeV/c, extrapolation is needed to estimate the total yields. Details of how systematic uncertainty is evaluated for the extrapolation procedure is discussed below, and this systematic uncertainty source is system size and multiplicity dependence since spectral shapes are different. Tables 5.5 to 5.7 summarize the systematic uncertainties of the measurement of $\langle m_{\mathrm{T}} \rangle - m$ from different sources for

each multiplicity interval in pp, pPb, and PbPb collisions. For each systematic source, the $\langle m_{\mathrm{T}} \rangle - m$ value is extracted from the spectra for each alternative condition and compared to default one to evaluate the systematic uncertainty. The Table 5.8 summarizes systematic sources of $\langle m_{\mathrm{T}} \rangle - m$. Only systematic uncertainties that are larger than 0.1% are presented.

Table 5.5: Summary of $\langle m_T \rangle - m$ results of mid-rapidity of $\mathrm{K}^0_{\mathrm{S}}$, $\Lambda$ in the pp system. statistical uncertainties are negligible compared to the systematic uncertainties, only systematic uncertainties are shown in the table

| multiplicity ranges | $\mathrm{K}^0_{\mathrm{S}}$ (GeV/c$^2$) | $\Lambda$ (GeV/c$^2$) |
|---|---|---|
| $(0,35)$ | $0.434 \pm 0.004$ | $0.42 \pm 0.023$ |
| $[35,60)$ | $0.583 \pm 0.004$ | $0.622 \pm 0.019$ |
| $[60,90)$ | $0.671 \pm 0.004$ | $0.736 \pm 0.02$ |
| $[90,110)$ | $0.743 \pm 0.004$ | $0.857 \pm 0.014$ |
| $[110,130)$ | $0.787 \pm 0.004$ | $0.926 \pm 0.013$ |
| $[130,\mathrm{above})$ | $0.833 \pm 0.004$ | $0.964 \pm 0.011$ |

Table 5.6: Summary of $\langle m_T \rangle - m$ results of mid-rapidity of $\mathrm{K}^0_{\mathrm{S}}$, $\Lambda$ and $\Xi^-$ in pPb system. statistical uncertainties are negligible compared to systematic uncertainties, only systematic uncertainties are shown in the table

| multiplicity ranges | $\mathrm{K}^0_{\mathrm{S}}$ (GeV/c$^2$) | $\Lambda$ (GeV/c$^2$) | $\Xi^-$ (GeV/c$^2$) |
|---|---|---|---|
| $(0,35)$ | $0.467 \pm 0.005$ | $0.47 \pm 0.025$ | $0.514 \pm 0.045$ |
| $[35,60)$ | $0.556 \pm 0.003$ | $0.609 \pm 0.015$ | $0.679 \pm 0.038$ |
| $[60,90)$ | $0.604 \pm 0.004$ | $0.68 \pm 0.018$ | $0.776 \pm 0.031$ |
| $[90,120)$ | $0.637 \pm 0.004$ | $0.736 \pm 0.013$ | $0.862 \pm 0.042$ |
| $[120,150)$ | $0.662 \pm 0.004$ | $0.779 \pm 0.01$ | $0.907 \pm 0.03$ |
| $[150,185)$ | $0.678 \pm 0.004$ | $0.809 \pm 0.011$ | $0.946 \pm 0.036$ |
| $[185,220)$ | $0.699 \pm 0.004$ | $0.842 \pm 0.012$ | $1.01 \pm 0.042$ |
| $[220,260)$ | $0.713 \pm 0.004$ | $0.862 \pm 0.014$ | $1.04 \pm 0.037$ |

### 5.2.1 Systematics in the $p_{\mathrm{T}}$ spectra

Systematic sources related to the $p_{\mathrm{T}}$ spectra of $\mathrm{K}^0_{\mathrm{S}}$, $\Lambda$, and $\Xi^-$ candidates in pp, pPb, and PbPb collisions are discussed in details in the following sections.

Table 5.7: Summary of $\langle m_T \rangle - m$ results of mid-rapidity of $K^0_S$, $\Lambda$ in PbPb system. statistical uncertainties are negligible compared to systematic uncertainties, only systematic uncertainties are shown in the table

| multiplicity ranges | $K^0_S$ (GeV/c$^2$) | $\Lambda$ (GeV/c$^2$) |
|---|---|---|
| $(0,35)$ | $0.382 \pm 0.004$ | $0.384 \pm 0.02$ |
| $[35,60)$ | $0.433 \pm 0.03$ | $0.462 \pm 0.016$ |
| $[60,90)$ | $0.447 \pm 0.003$ | $0.485 \pm 0.018$ |
| $[90,120)$ | $0.458 \pm 0.003$ | $0.503 \pm 0.011$ |
| $[120,150)$ | $0.471 \pm 0.003$ | $0.521 \pm 0.01$ |
| $[150,185)$ | $0.479 \pm 0.003$ | $0.535 \pm 0.007$ |
| $[185,220)$ | $0.491 \pm 0.003$ | $0.55 \pm 0.008$ |
| $[220,260)$ | $0.502 \pm 0.003$ | $0.551 \pm 0.014$ |

Table 5.8: Summary of systematic uncertainties of $\langle m_T \rangle - m$ results at mid-rapidity of $K^0_S$, $\Lambda$ and $\Xi^-$ in pPb system. This table provides detail systematic uncertainties that come from each systematic sources from multiplicity bin $220 \leq N^{\text{offline}}_{\text{trk}} < 260$ for pPb collisions

| systematic sources | $K^0_S$ (%) | $\Lambda$ (%) | $\Xi^-$ (%) |
|---|---|---|---|
| Reconstruction cuts | 0.4 | 0.3 | 1.0 |
| Beam direction | 0.3 | 0.1 | 0.7 |
| Mass fitting | 0.1 | 1.0 | 0.5 |
| Extrapolation | 0.3 | 1.1 | 1.0 |
| Total | 0.6 | 1.5 | 1.7 |

#### 5.2.1.1 Reconstruction criteria of $K^0_S$, $\Lambda$, and $\Xi^-$ candidates

In order to investigate the systematic uncertainties that come from the reconstruction criteria of the strange particle candidates, results using a set of tighter and looser reconstruction cuts are studied. Studies show that varing the reconstruction cuts could introduce around 20% difference in efficiency, however, the efficiency-corrected spectra would only change by a few percent.

The set of tight (loose) cuts for $V^0$s are as follows:

- Daughter track DCA significance $> 1.25(1)$
- $V^0$ candidate pointing angle $> 0.9995(0.995)$
- $V^0$ candidate decay length significance $> 7(3)$

For $\Xi^-$ reconstruction, the set of tight (loose) cuts are as follows:

- 3D impact parameter significance of proton track from $\Lambda$ decay with respect to the primary vertex $> 4(2)$
- 3D impact parameter significance of $\pi$ track from $\Lambda$ decay with respect to the primary vertex $> 5(3)$
- 3D impact parameter significance of $\pi$ track from $\Xi^-$ decay with respect to the primary vertex $> 6(4)$
- 3D impact parameter significance of the $\Xi^-$ candidate with respect to the primary vertex $< 2(3)$
- 3D separation significance between $\Lambda$ vertex and primary vertex $> 14(10)$
- 3D separation significance between $\Xi^-$ vertex and primary vertex $> 4(2)$

These studies are done independently for pp, pPb, and PbPb collisions. Here, only a sample plot for $\Xi^-$ in mid-rapidity pPb collisions at $185 \leq N_{\text{trk}}^{\text{offline}} < 220$ is shown in Fig. 5.2.

#### 5.2.1.2 Yield extraction of $K^0_S$, $\Lambda$, and $\Xi^-$ candidates

In this section, systematic uncertainties related to the way the signal was extracted are studied: mass fitting range, background fitting function, fitting or counting to get yield counts. These sources will be discussed in the following texts one by one.

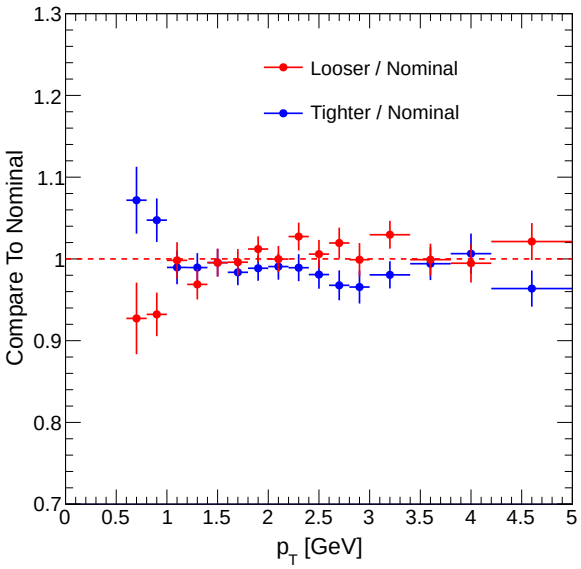


Figure 5.2: $\Xi^-$ systematics plot evaluating the effect of the reconstruction cuts in mid-rapidity pPb collisions at $185 \leq N_{\text{trk}}^{\text{offline}} < 220$. The red dots in the figure stand for the ratio of spectra using looser cut criteria over nominal one. The blue dots represent the ratio of spectra using tighter cut criteria over nominal one.

Since the background functional forms used in the nominal results are very stable, changing the fitting range does not change the results much. Studies showed that the change is within 1%, which can be neglected.

To study how much the results depend on the choice of the background functional forms, results using polynomial as a background functional form are compared to the nominal results. For $V^0$s and $\Xi^-$, 4th order polynomial and linear background functional form are studied, respectively. The sample plot for $\Xi^-$ in mid-rapidity pPb collisions at $185 \leq N_{\text{trk}}^{\text{offline}} < 220$ is shown on the left of Fig. 5.3.

Once the invariant mass peaks are fitted with signal and background functions, the signal counts can be obtained either by integrating the signal function or by using a background estimation based on the yield obtained in side-bands located away from the main mass peak. The results from these two methods are compared. A sample plot for $\Xi^-$ in mid-rapidity

pPb collisions at $185 \leq N_{\text{trk}}^{\text{offline}} < 220$ is shown on the right of Fig. 5.3.

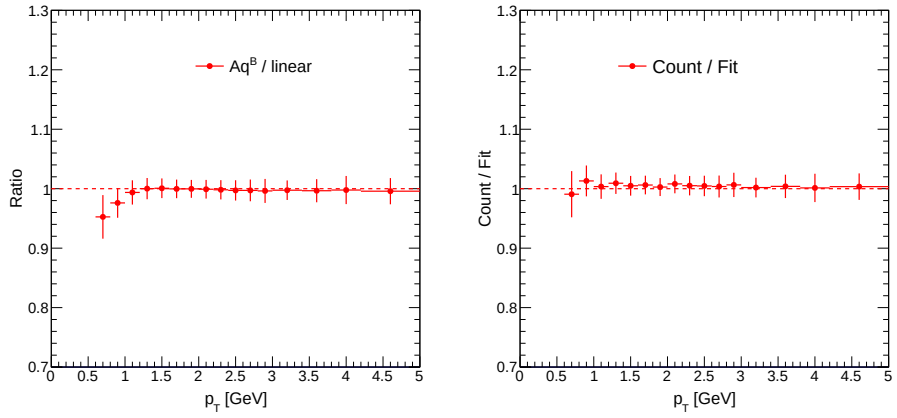


Figure 5.3: $\Xi^-$ systematics plot of varied background functions (left) and varied methods of yield extraction (right) in mid-rapidity pPb collisions with $185 \leq N_{\text{trk}}^{\text{offline}} < 220$.

In general, for systematic uncertainty in the yield extraction, 2% and 3% is assigned for $V^0$ and $\Xi^-$ respectively.

#### 5.2.1.3 Rapidity binning of $K_S^0$, $\Lambda$, and $\Xi^-$ candidates

Since the particle's rapidity distribution is not flat, the rapidity binning used in this analysis may result in incorrect efficiency due to the large bin width. To investigate if there is a binning issue that could change the particle spectra, the following procedure is used:

- Divide the default rapidity bins into 2 smaller bins, and calculate the efficiency for $K_S^0$, $\Lambda$, and $\Xi^-$
- Extract raw yield from the smaller bins and obtain corrected spectra with efficiency correction
- Integrate the smaller bins back to default rapidity binning, and compare with the original spectra

- Take the deviations from unity as systematic uncertainties

A sample plot for $\Xi^-$ in mid-rapidity pPb collisions at $185 \leq N_{\text{trk}}^{\text{offline}} < 220$ is shown in Fig. 5.4.

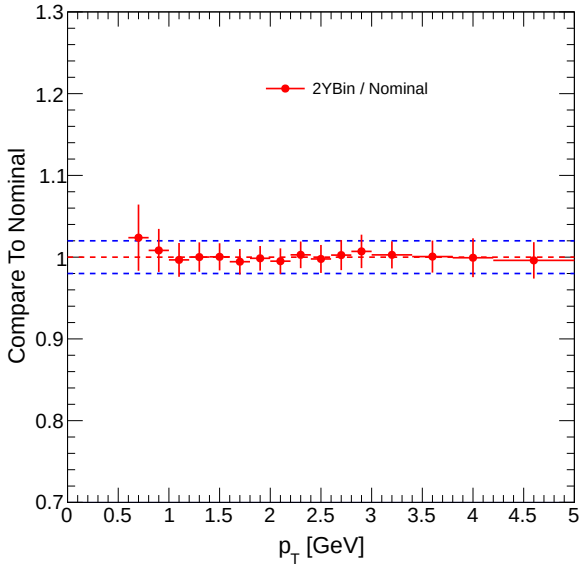


Figure 5.4: $\Xi^-$ systematics plot evaluating the effect of rapidity binning in mid-rapidity pPb at $185 \leq N_{\text{trk}}^{\text{offline}} < 220$.

#### 5.2.1.4 Efficiency smoothing of $K_S^0$, $\Lambda$, and $\Xi^-$ candidates

In the efficiency table, uneven structure may show up due to limited statistics of the MC samples. This is not the case for $V^0$s, because of their abundance in the samples. However, for $\Xi^-$ candidates, it is hard to get enough statistics to get smooth efficiency table. So, a 4th order polynomial function is used to fit the efficiency table to get a smooth efficiency table. Thus, systematic uncertainties related to this source should be studied. A sample plot for $\Xi^-$ in mid-rapidity pPb collisions at $185 \leq N_{\text{trk}}^{\text{offline}} < 220$ is shown in Fig. 5.5.

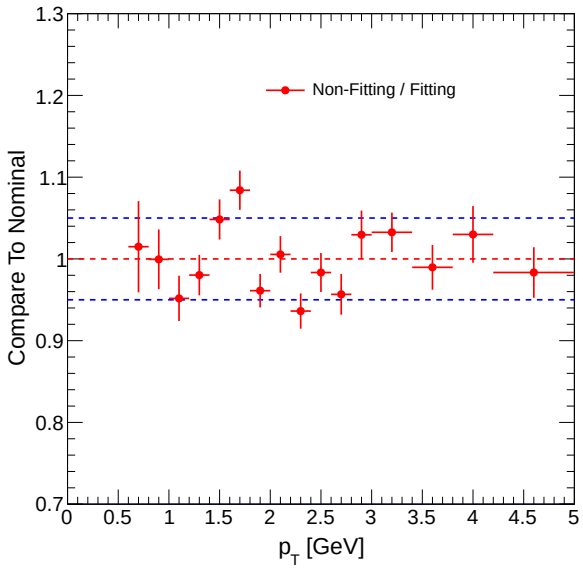


Figure 5.5: $\Xi^-$ systematics plot of evaluation the uncertainty in the efficiency correction in mid-rapidity pPb at $185 \leq N_{\text{trk}}^{\text{offline}} < 220$.

#### 5.2.1.5 Momentum resolution of $K^0_S$, $\Lambda$, and $\Xi^-$ candidates

Since the detector does not have perfect momentum resolution, the momentum of each particle could have uncertainties due to the finite resolution, which could also change the shape of the $p_{\text{T}}$ spectra. In order to investigate this issue, a simple pseudo-experiment in the MC samples needs to be performed, which is also done in the charged hadron analysis [69].

- Perform matching between the generated level particles with reconstructed level particles in order to produce a smearing function in bins of $p_{\text{T}}$ for both $K^0_S$ and $\Lambda$ , where the smearing function would be mostly a Gaussian and it would give the probability of how much the momentum could deviate from the true values.

- Smear each particle's $p_{\text{T}}$ value by randomly assigning a smearing factor ( 20-50 MeV/c) from the Gaussian function in each corresponding $p_{\text{T}}$ bins and generate the smear spectra.

- Compare the default generated spectra with the smeared spectra and take the deviations for systematic uncertainties

To be conservative, 2% is quoted for the entire $p_{\mathrm{T}}$ range for all particle species.

#### 5.2.1.6 Beam direction of $\mathrm{K}^0_{\mathrm{S}}$, $\Lambda$, and $\Xi^-$ candidates in pPb collisions

In the middle of the pPb data taking, the direction of the beam was reversed. To ensure data from two beam directions can be combined, $p_{\mathrm{T}}$ spectra in pPb collisions of two different beam directions are compared. In CMS Heavy Ion group, pPb means proton goes to positive z direction ("reverse"), while Pbp means proton goes to negative z direction ("prompt"). Sample plot for $\Xi^-$ in mid-rapidity pPb collisions at $185 \leq N_{\mathrm{trk}}^{\mathrm{offline}} < 220$ is shown in Fig. 5.6. For systematic uncertainty of beam direction, for entire $p_{\mathrm{T}}$ range, 3% and 4% are quoted for $V^0$s and $\Xi^-$ candidates, respectively.

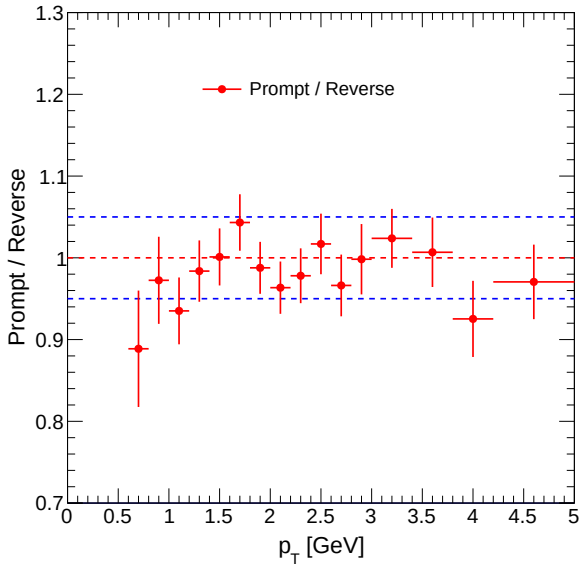


Figure 5.6: $\Xi^-$ systematics plot of beam direction in mid-rapidity pPb at $185 \leq N_{\mathrm{trk}}^{\mathrm{offline}} < 220$.

#### 5.2.1.7 Pileup in pp collisions

During the 2010 pp run, the pileup [1] is not negligible. To investigate systematic uncertainty of pileup, especially for very high multiplicity events, results with different pileup rejection conditions are studied. The pileup rejection conditions are as following:

- No pileup rejection
- Standard pileup rejection
- Only one reconstructed vertex present in the event, this will result in some loss of good single collision events that have split reconstructed vertices but no real pileup collisions.

The results of particle spectra as a function of $p_{\mathrm{T}}$ in 7 TeV pp collisions with different pileup rejection conditions are compared. For systematic uncertainty of pileup in pp, 3% and 1% for $p_{\mathrm{T}} < 1.5$ GeV and $p_{\mathrm{T}} > 1.5$ GeV for $V^0$s, and 3% for $\Xi^-$ for the entire $p_{\mathrm{T}}$ range. Sample plot of $\Xi^-$ is shown in Fig. 5.7.

Pileup effect in other collision systems is negligible, thus not considered.

### 5.2.2 Systematics of $\langle m_{\mathrm{T}} \rangle - m$ calculation

To extract the $\langle m_{\mathrm{T}} \rangle - m$, a key step is to get the $p_{\mathrm{T}}$ spectra down to 0 GeV, however, sometimes, spectra can only be measured down to a certain $p_{\mathrm{T}}$. In this case, extrapolation is needed to estimate the shape of $p_{\mathrm{T}}$ spectra at low $p_{\mathrm{T}}$. Systematic uncertainties related to calculation of $\langle m_{\mathrm{T}} \rangle - m$ are discussed in details in the following context.

[1] more than one collisions in the same bunch crossing

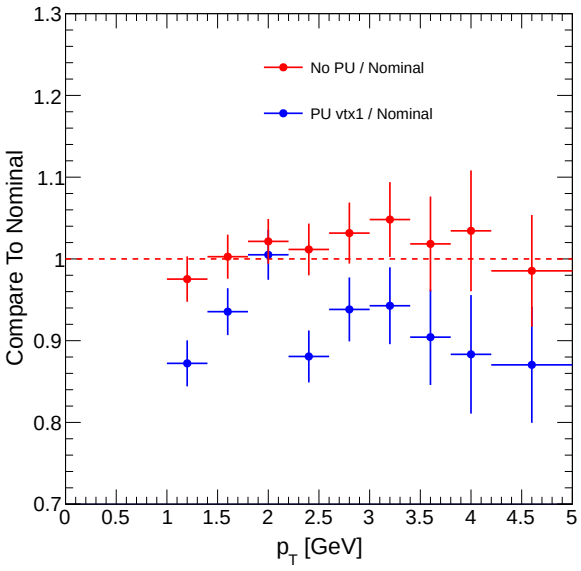


Figure 5.7: Pile-up study of $\Xi^-$ in mid-rapidity pp with multiplicity bin $0 \leq N_{\mathrm{trk}}^{\mathrm{offline}} < 35$. In this plot, "Nominal" stands for our default pp pileup filter. "PU vtx1" stands for the tightest filter where only one reconstructed vertex presented in each event. Red dots are the ratios of No pile-up filter over the default one, while blue dots stand for the ratios of the tightest filter over the default one.

#### 5.2.2.1 Extrapolation of low $p_{\mathrm{T}}$ spectra

In order to estimate the systematic uncertainties of extrapolation of low $p_{\mathrm{T}}$ particle spectra, results with different function forms have to be investigated. For the nominal results, individual blast wave function [70] is used. Linear function and 2nd order polynomial function are used for the systematic study. The three functions forms are used to fit the same set of data points. The Fig. 5.8 demonstrates how these fittings look like. From Fig. 5.8, it is easy to see that individual blast wave function describes data points best.

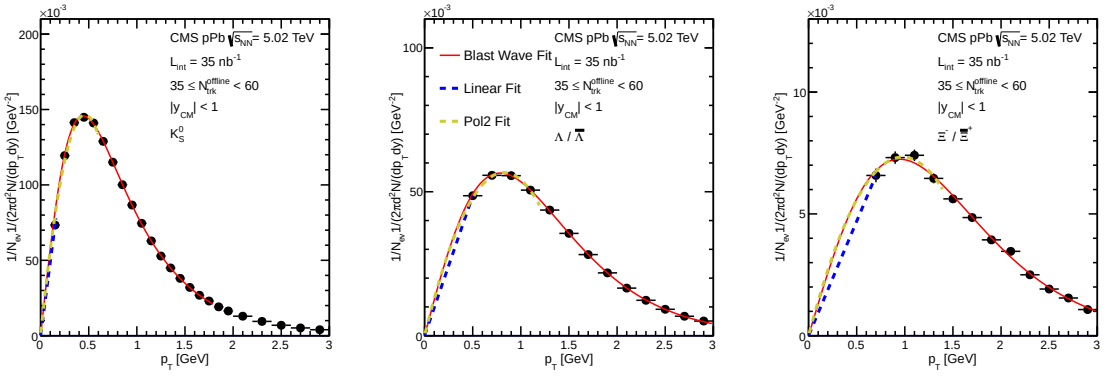


Figure 5.8: Individual blast-wave fits, 2nd order polynomials and linear function have been fitted to $K^0_S$, $\Lambda$, and $\Xi^-$ for mid-rapidity range $-1.0 < y_{\rm cm} < 1.0$ in pPb system. The fitting range individual blast-wave fits for $K^0_S$ is (0,1.5) GeV/c and $\Lambda$ (0.6,3.0) GeV/c.

#### 5.2.2.2 Method for $\langle m_{\rm T} \rangle - m$ calculation

To take advantage of $p_{\rm T}$ spectra measurement, extrapolation is only used at the low $p_{\rm T}$ part, where the spectra can not be measured. For the nominal results, individual blast wave fit is used to estimate the shape of spectra in the low pt region. After getting the fitting function for the low $p_{\rm T}$ part, the low $p_{\rm T}$ region is binned into $p_{\rm T}$ bins based on the fitting function. In this way, new histograms consist two parts: measurement and extrapolation. Then, $p_{\rm T}$ boundaries are transformed into $m_{\rm T}$ boundaries. By doing this, $m_{\rm T}$ spectra can be obtained without redoing the analysis. The last step is to calculate $\langle m_{\rm T} \rangle$ using the histograms of $m_{\rm T}$ spectra. From the histograms, number of particles within a specific $m$ interval can be obtained easily. Then, the total $m_{\rm T}$ for all the particles in this $m_{\rm T}$ bin can be estimated by using $m_{\rm T}$ at the bin center times the number of particles. By summing us total $m_{\rm T}$ of all $m_{\rm T}$ bins, the total $m_{\rm T}$ for the whole $m_{\rm T}$ range can be obtained. Then $\langle m_{\rm T} \rangle$ can be easily calculated by dividing the total $m_{\rm T}$ by the total number of particles.

Notice that the above calculation contains some approximation to simplifying the calculation process, verification is needed to ensure that the above method can get the correct $\langle m_{\rm T} \rangle$.

This can be verified with MC samples, which contains GEN level information. The study is performed with EPOS. Since, at GEN level, $p_{\mathrm{T}}$ of each generated particle is known, $m_{\mathrm{T}}$ can be calculated for each particle. Thus, the true $\langle m_{\mathrm{T}} \rangle$ can be known. By binning the generated particle spectra into histograms, $\langle m_{\mathrm{T}} \rangle$ can be calculated with the method introduced above. By comparing the true $\langle m_{\mathrm{T}} \rangle$ with the calculated $\langle m_{\mathrm{T}} \rangle$, systematic uncertainties related to the method for $\langle m_{\mathrm{T}} \rangle$ calculation can be known. The comparison is as following:

- For $\mathrm{K}^0_{\mathrm{S}}$, the true value of $\langle m_{\mathrm{T}} \rangle$ is 0.991895, and $\langle m_{\mathrm{T}} \rangle = 0.98637$ by using the same method as data. The difference is 0.557%
- For $\Lambda$ the true value of $\langle m_{\mathrm{T}} \rangle$ is 1.74013, and $\langle m_{\mathrm{T}} \rangle = 1.72511$ by using the same method as data. The difference is 0.863%
- For $\Xi^-$ the true value of $\langle m_{\mathrm{T}} \rangle$ is 1.99051, and $\langle m_{\mathrm{T}} \rangle = 1.96682$ by using the same method as data. The difference is 1.190%

The calculated $\langle m_{\mathrm{T}} \rangle$ value is very close to the true value. To be conservative, 1.5% is assigned as systematic uncertainty for this source.

## 5.3 Results

Details of the results can be found in the published paper [51].

### 5.3.1 Invariant mass peaks

In this section, invariant mass distributions of reconstructed $\mathrm{K}^0_{\mathrm{S}}$, $\Lambda$, and $\Xi^-$ candidates with $1 < p_{\mathrm{T}} < 3$ GeV are shown in Fig. 5.9 for pPb events with $220 \leq N^{\mathrm{offline}}_{\mathrm{trk}} < 260$. Prominent mass peaks are visible, with little background. The solid lines show the result of maximum likelihood fit. Details of the fitting can be found in Sec. 4.2.1.

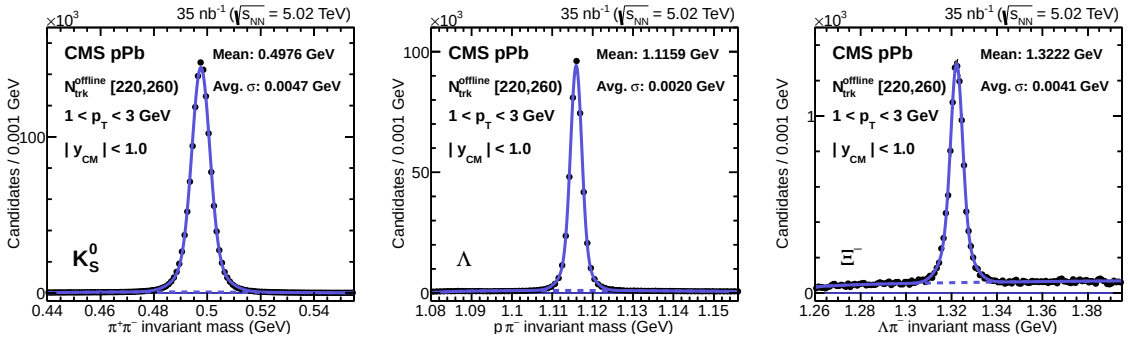


Figure 5.9: Invariant mass distribution of $K_S^0$ (left), $\Lambda$ (middle), and $\Xi^-$ (right) candidates in the $p_T$ range 1–3 GeV for $220 \leq N_{trk}^{offline} < 260$ in pPb collisions. The inclusion of the charge-conjugate states is implied for $\Lambda$ and $\Xi^-$ particles. The solid lines show the results of fits described in the text. The dashed lines indicate the fitted background component.

### 5.3.2 Multiplicity dependence of $p_T$ spectra of $K_S^0$, $\Lambda$, and $\Xi^-$

With the cut criteria and analysis methods introduced above, the $p_T$ spectra of $K_S^0$, $\Lambda$, and $\Xi^-$ particles with $|y_{CM}| < 1$ in pp collisions at $\sqrt{s}$ = 7 TeV (top), pPb collisions at $\sqrt{s_{NN}}$ = 5.02 TeV (middle), and PbPb collisions at $\sqrt{s_{NN}}$ = 2.76 TeV (bottom) are presented in Fig. 5.10, for different multiplicity intervals. Due to details in the implementation of the dedicated high-multiplicity trigger thresholds used to select the pp events, the multiplicity intervals for pp events differ slightly from those for pPb and PbPb events. The $p_T$ differential yields is defined as $dN^2/(2\pi p_T dp_T dy)$. For the purpose of better visibility, the data are scaled by factors of $2^{-n}$, as indicated in the figure legend. A clear evolution of the spectral shape with multiplicity can be seen for each particle species in each collision system. For higher multiplicity events, the spectra tend to become flatter, indicating a larger $\langle KE_T \rangle$ value. Within each collision system, heavier particles (e.g., $\Xi^-$) exhibit a harder spectrum than lighter particles ($K_S^0$), especially for high-multiplicity events.

### 5.3.3 Particle ratios

To examine the difference in the multiplicity dependence of the spectra in greater detail, the ratios $\Lambda/K^0_S$ and $\Xi^-/\Lambda$ of the yields are shown in Fig. 5.11 as a function of $p_T$ for different multiplicity ranges in the pp, pPb, and PbPb systems. The results for the $\Lambda/K^0_S$ ratio are shown in Fig. 5.11 (top). For $p_T \leq 2$ GeV, the $\Lambda/K^0_S$ ratio is seen to be smaller in high-multiplicity events than in low-multiplicity events for a given $p_T$ value. In pp and pPb collisions, this trend is similar to what has been observed between peripheral and central PbPb collisions [71]; this trend is not as evident for the PbPb data in Fig. 5.11 (top right) because in the present study only PbPb events of 50–100% centrality are considered. At higher $p_T$, this multiplicity ordering of the $\Lambda/K^0_S$ ratio is reversed. In hydrodynamic models such as those presented in Refs.[72, 73], this behavior can be interpreted as the effect of radial flow. A stronger radial flow is developed in higher-multiplicity events, which boosts heavier particles (e.g., $\Lambda$) to higher $p_T$, resulting in a suppression of the $\Lambda/K^0_S$ ratio at low $p_T$. Comparing the various collision systems at low $p_T$, the difference in the $\Lambda/K^0_S$ ratio between low- and high-multiplicity events is seen to be largest for the pp data. In the hydrodynamic model of Ref.[74], smaller collision systems like pp produce a larger radial-flow effect than larger systems like pPb or PbPb, for similar multiplicities, which could explain this observation. For $p_T > 2$ GeV, the baryon enhancement could be explained by recombination models, in which free quarks recombine to form hadrons [75]. In previous studies (e.g., Ref.[76], it has been shown that the average $p_T$ value of various particle species has only a slight center-of-mass energy dependence (10% at high multiplicity). This dependence is not sufficient to explain the difference observed in Fig. 5.11 among various systems.

For each multiplicity interval, the $\Lambda/K^0_S$ ratio reaches a maximum that has a similar value for all three collision processes, and then decreases at higher $p_T$. The location of the maximum increases with multiplicity from around $p_T$ = 2 to 3 GeV.

The results for the $\Xi^-/\Lambda$ ratio are shown in Fig.5.11(bottom). In this case, the difference between the low- and high-multiplicity events is much smaller than for the $\Lambda/K^0_S$ ratio, for all three collision systems. This could be explained by the fact that $\Xi^-$ and $\Lambda$ have similar masses. However, due to the large systematic uncertainty, it is not possible to draw a solid conclusion with respect to the radial-flow interpretation. For all systems, the $\Xi^-/\Lambda$ ratio increases with $p_T$ and reaches a plateau at around $p_T$ = 3 GeV.

### 5.3.4 $\langle m_T \rangle - m$ distribution of $K^0_S$, $\Lambda$, and $\Xi^-$

The evolution of the $p_T$ spectra with multiplicity can be compared more directly among the three systems through examination of the $\langle KE_T \rangle$ value. The $\langle KE_T \rangle$ values at $|y_{CM}| < 1$ for $K^0_S$, $\Lambda$, and $\Xi^-$ particles as a function of multiplicity are shown in Fig. 5.12. Extrapolation of the $p_T$ spectra down to $p_T$ = 0 GeV is a crucial step in extracting the $\langle KE_T \rangle$ values, while the impact of the extrapolation up to $p_T \approx \infty$ is negligible, both on the value of $\langle KE_T \rangle$ and its uncertainty. For the $\Xi^-$ particle, only results in pPb collisions are shown due to the limitation of the low-$p_T$ reach in pp and PbPb collisions, as can be seen from Fig.5.10. Blast-wave fits to the individual spectra, which only consider the spectrum shape but do not impose any physics constraint, are used to obtain the extrapolation. The fraction of the extrapolated yield with respect to the total yield is about 1.2–2.5% for the $K^0_S$, 5.8–15.1% for the $\Lambda$, and 5.4–20.4% for the $\Xi^-$ particles, depending on the multiplicity. Alternative methods to perform the extrapolation are used to evaluate the systematic uncertainty, including use of 2nd order polynomial fit to the particle spectra, and a linear extrapolation from the yields in low $p_T$.

For the lowest multiplicity range, the $\langle KE_T \rangle$ values for each particle species are seen to be similar. For all particle species, $\langle KE_T \rangle$ increases with increasing multiplicity. However, the slope of the increase differs for different particles, with the heavier particles exhibiting a

faster growth in $\langle KE_{\mathrm{T}} \rangle$ for all systems. For a given multiplicity range, the $\langle KE_{\mathrm{T}} \rangle$ value is roughly proportional to the particle's mass. In PbPb collisions, this can be understood to be due to the onset of radial flow [77, 78]. The observed difference between particle species at high multiplicity is seen to be larger for pp and pPb events than for PbPb events. Note, however, the difference in the center-of-mass energies among the three systems.

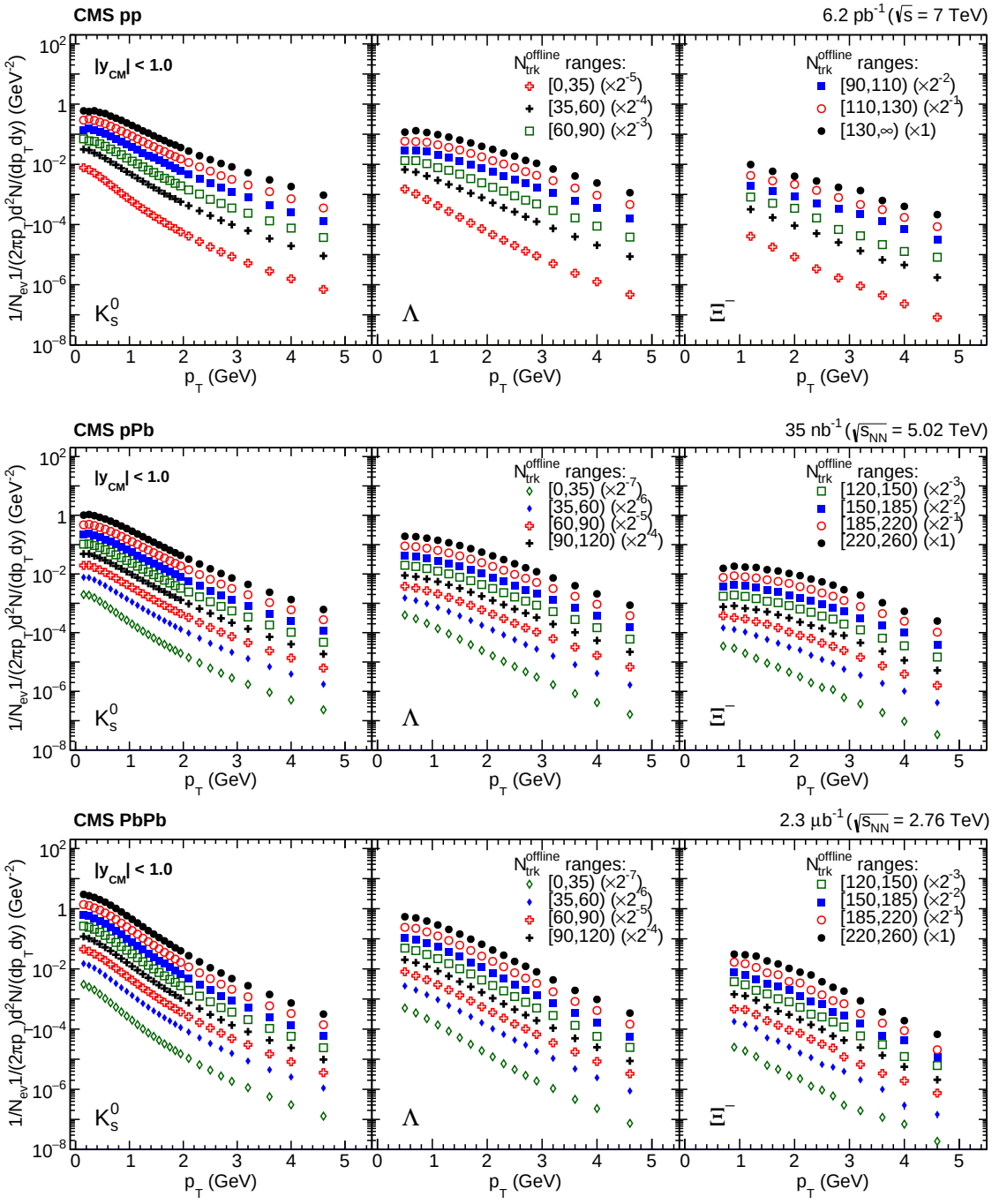


Figure 5.10: The $p_{\mathrm{T}}$ spectra of $\mathrm{K}^0_{\mathrm{S}}$, $\Lambda$, and $\Xi^-$ particles in the center-of-mass rapidity range $|y_{\mathrm{cm}}| < 1$ in pp collisions at $\sqrt{s} = 7$ TeV (top), pPbcollisions at $\sqrt{s_{NN}} = 5.02$ TeV (middle), and PbPb collisions at $\sqrt{s_{NN}} = 2.76$ TeV (bottom) for different multiplicity intervals. The inclusion of the charge-conjugate states is implied for $\Lambda$ and $\Xi^-$ particles. The data in the different multiplicity intervals are scaled by factors of $2^{-\mathrm{n}}$ for better visibility. The statistical uncertainties are smaller than the markers and the systematic uncertainties are not shown.

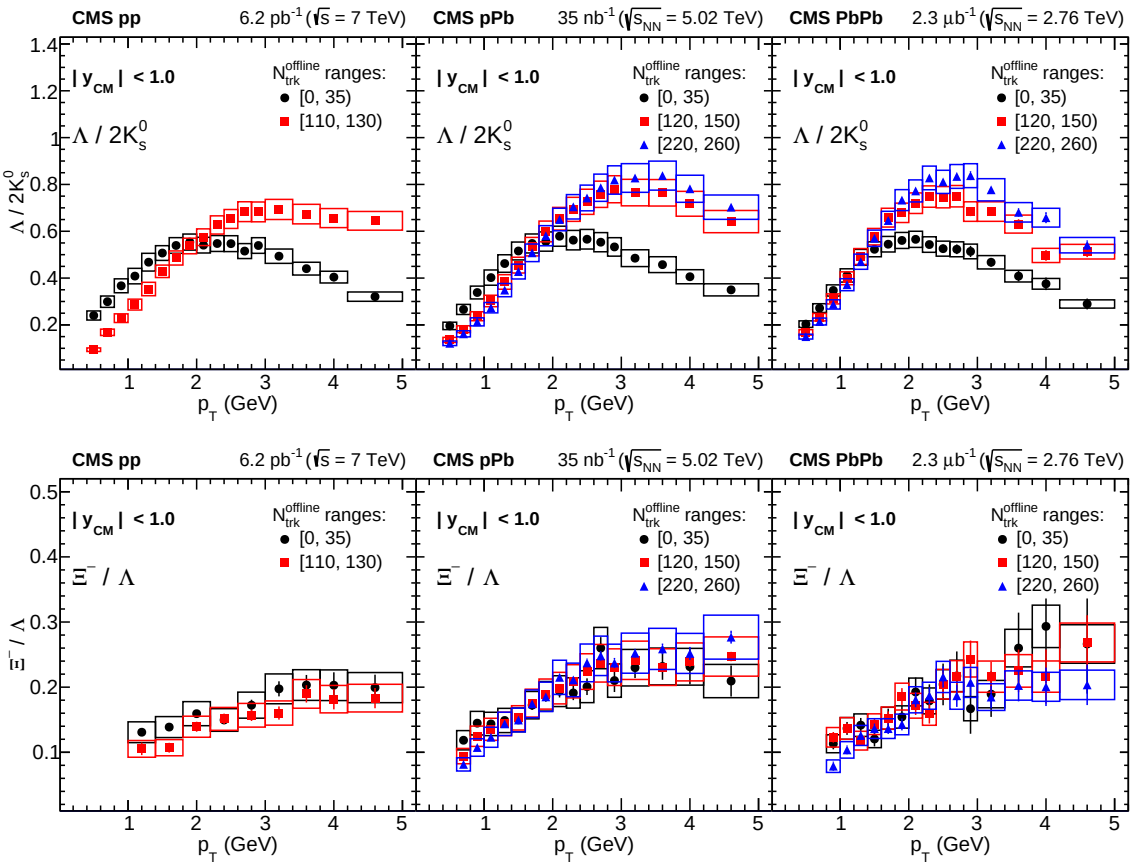


Figure 5.11: Ratios of $p_{\mathrm{T}}$ spectra for $\Lambda/2\mathrm{K}^0_{\mathrm{S}}$ (top) and $\Xi^-/\Lambda$ (bottom) in the center-of-mass rapidity range $|y_{\mathrm{cm}}| < 1.0$ for pp collisions at $\sqrt{s} = 7$ TeV (left), pPb collisions at $\sqrt{s_{NN}} = 5.02$ TeV (middle), and PbPb collisions at $\sqrt{s_{NN}} = 2.76$ TeV (right). Two (for pp) or three (for pPb and PbPb) representative multiplicity intervals are presented. The inclusion of the charge-conjugate states is implied for $\Lambda$ and $\Xi^-$ particles. The error bars represent the statistical uncertainties, while the boxes indicate the systematic uncertainties.

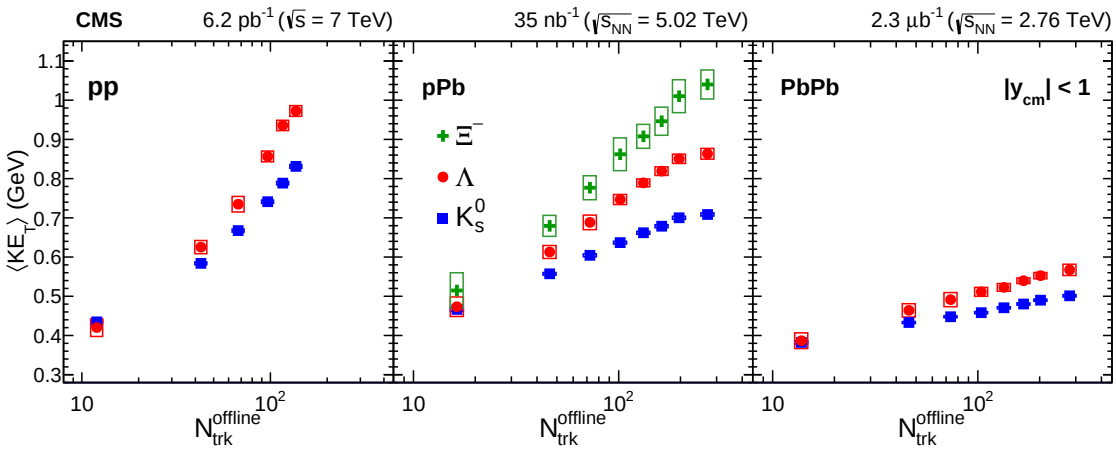


Figure 5.12: The average transverse kinetic energy, $\langle KE_{\mathrm{T}} \rangle$, at $|y_{\mathrm{cm}}| < 1$ for $\mathrm{K}^0_{\mathrm{S}}$, $\Lambda$, and $\Xi^-$ particles as a function of multiplicity in pp, pPb, and PbPb collisions. The inclusion of the charge-conjugate states is implied for $\Lambda$ and $\Xi^-$ particles. For the $\Xi^-$, only results from pPb collisions are shown. The error bars represent the statistical uncertainties, while the boxes indicate the systematic uncertainties.

# Chapter 6

## Nuclear modification factors of strange hadrons

Previous publication [51] focuses on the spectra of $K^0_S$, $\Lambda$, and $\Xi^-$ at low $p_T$ part for different multiplicity intervals. The radial flow effect on the spectra shape is studied by comparing particle ratios at similar multiplicity ranges for different collision systems. In the latest analysis [79], $K^0_S$, $\Lambda$, $\Xi^-$, and $\Omega^-$ $p_T$ spectra at 5 TeV pp and pPb are measured to as high $p_T$ as possible. With particle spectra of pp and pPb at the same energy, the nuclear modification factor, $R_{pPb}$, can be studied.

The initial idea is to use pp collisions as the baseline, and use pPb collisions as the control experiment to study PbPb collisions. However, recent studies [23, 24, 25, 26] regarding the high-multiplicity events in small systems show that small systems are an interesting and informative system to study on its own.

Another quantity measured in this analysis is called particle yield rapidity asymmetry, $Y_{asym}$, as pPb is an asymmetrical system. The definition of $Y_{asym}$ is as follows:

$$Y_{asym}(p_T) = \frac{d^2N(p_T)/dy_{CM}dp_T|_{y_{CM}\in[-b,-a]}}{d^2N(p_T)/dy_{CM}dp_T|_{y_{CM}\in[a,b]}}, \tag{6.1}$$

where $a$ and $b$ are always positive and refer to the proton beam direction.

The effect of radial flow [80], Cronin enhancement [81, 82], and nuclear shadowing [83] on particle spectra can be studied with the measurement of $R_{pPb}$ and $Y_{asym}$. Details about the measurements will be discussed below.

## 6.1 Data samples and event selection

The pp data sample at $\sqrt{s}$ = 5.02 TeV used in this analysis is recored with CMS detector in 2015. The pp sample corresponds to an integrated luminosity of 27.4 $pb^{-1}$. The pPb data sample at $\sqrt{s_{NN}}$ = 5.02 TeV used in this analysis is recored with CMS detector in 2013. The pPb sample corresponds to an integrated luminosity of 35 $nb^{-1}$. To determine the performance of strange hadron reconstruction, event selection efficiency, and cross-check of other potential detector effects, EPOS samples are generated for both pp and pPb collisions.

In order to ensure that the events selected for this analysis are not contaminated by non-collision events (beam-gas, beam-pipe, beam-halo, cosmics, beam-scraping events), standard set of event selections used by the CMS Heavy Ion Group for physics analysis are applied for pp and pPb data. For this analysis, strange particle spectra in pp collisions are corrected to inelastic collisions, as what was done in Ref.[62]. While spectra in pPb collisions are corrected to "double sided" ("DS") collisions, as what was done in Ref.[69]. A DS collision is defined as a collision in which at least one particle of lifetime $c\tau > 10^{-18}m$ with energy E $\geq$ 3 GeV is produced in the region $3 < \eta < 5$, and another such particle is produced in the region $-5 < \eta < -3$. This definition was chosen as the combination of the single track trigger and HF coincidence filter produces a collection of events that closely match the double sided definition and it is easy to evaluate in simulation.

The event selection criteria for pp used in this analysis are listed below:

- The standard filter for vertices: !isFake & $|vertex_z| \leq 25$ & position.Rho $\leq 2$ & tracksSize $\geq 2$
- The standard beam-scraping filter: if there are more than 10 tracks, then at least 25% of the tracks have to be highPurity

Besides the event selection criteria for pp collision, there is an additional requirement for pPb collision: at least one tower records $> 3$ GeV in energy deposits on each side.

## 6.2 Systematics

The systematic uncertainty sources of $K^0_S$, $\Lambda$, $\Xi^-$, and $\Omega^-$ are investigated for different $y_{CM}$ bins in both pp and pPb collisions. The systematic uncertainty sources that have been investigated are following: the method to extract yield, the effect of rapidity binning, strange particle candidates selection criteria, the effect of momentum resolution, tracking efficiency, feed-down effect of $\Lambda$ candidates, pileup effect (pp only), beam direction (pPb only), and luminosity (pp only). For some of the systematic sources, non-negligible $p_T$ dependence can be observed, in this case, different systematic uncertainties are quoted for different $p_T$ ranges. The total systematic uncertainties of particle yields are calculated by adding all the listed sources in quadrature. To calculate the total systematic uncertainties of nuclear modification factors and particle yield rapidity asymmetry, cancellation of systematic uncertainties is needed to be taken into account.

For each of the systematic sources, the ratios of $p_T$ spectra are calculated with various alternative conditions with respect to the nominal condition. Then, the absolute values of maximum discrepancy to on in the ratio among various conditions for different $p_T$ bins are fitted by a constant value. For some systematic uncertainty sources, the spectra ratios of $K^0_S$ ($\Lambda$) show different values for $p_T < 0.6(1.0)$ GeV and $p_T > 0.6(1.0)$ GeV, due to the fact that background level of invariant mass distributions of $K^0_S$ ($\Lambda$) is higher at the low $p_T$ region. Hence, for those systematic sources, the systematic uncertainties are evaluated separately for $p_T < 0.6(1.0)$ GeV and $p_T > 0.6(1.0)$ GeV using the method described above.

For systematic uncertainties of $R_{\rm pPb}$ and $Y_{\rm asym}$, the cancellation between numerator and de-

nominator is evaluated thoroughly. Instead of checking how much spectra has changed with various alternative conditions with respect to the nominal condition, the changes of $R_{\mathrm{pPb}}$ and $Y_{\mathrm{asym}}$ is checked. The systematic uncertainties are quoted using the method described above.

Detailed discussion of each systematic source is introduced below.

Tables 6.1 and 6.2 summarize the sources of systematic uncertainties in $\mathrm{K}^0_{\mathrm{S}}$, $\Lambda$, $\Xi^-$, and $\Omega^-$ $p_{\mathrm{T}}$ spectra, $R_{\mathrm{pPb}}$, and $Y_{\mathrm{asym}}$ at different $y_{\mathrm{CM}}$ ranges in both pp and pPbcollisions. The dominant sources of systematic uncertainty are associated with the strange-particle reconstruction, especially the efficiency determination.

Table 6.1: Summary of different sources of systematic uncertainties of $\mathrm{K}^0_{\mathrm{S}}$, $\Lambda$, $\Xi^-$, and $\Omega^-$ $p_{\mathrm{T}}$ spectra and $R_{\mathrm{pPb}}$ at different $y_{\mathrm{CM}}$ ranges in both pp and pPbcollisions. The ranges quoted cover both the $p_{\mathrm{T}}$ and the rapidity dependence of the uncertainties.

| Source | $\mathrm{K}^0_{\mathrm{S}}$ (%) | $\Lambda$ (%) | $\Xi^-$ (%) | $\Omega^-$ (%) |
|---|---|---|---|---|
| Yield extraction | 0–2.0 | 0–4.0 | 2.0 | 3.0 |
| Selection criteria | 1.0–4.0 | 1.0–5.0 | 3.0 | 6.0 |
| Momentum resolution | 1.0 | 1.0 | 1.0 | 1.0 |
| Tracking efficiency | 8.0 | 8.0 | 12.0 | 12.0 |
| Feed-down correction | – | 2.0–3.0 | – | – |
| Pileup effect(pp only) | 1.0–2.3 | 1.0–2.0 | 3.0 | 3.0 |
| Beam direction(pPbonly) | 1.0–4.0 | 1.0–5.0 | 3.0 | 4.0 |
| Luminosity (pp only) | 2.3 | 2.3 | 2.3 | 2.3 |
| $\langle T_{\mathrm{pPb}} \rangle$ (for $R_{\mathrm{pPb}}$) | 4.8 | 4.8 | 4.8 | 4.8 |
| Total (yields in pp) | 8.6–9.3 | 8.9–10.6 | 13.1 | 14.3 |
| Total (yields in pPb) | 8.2–10.1 | 8.6–12.3 | 13.8 | 15.1 |
| Total ($R_{\mathrm{pPb}}$) | 3.1–5.6 | 4.3–10.4 | 6.8 | 10.8 |

### 6.2.1 Reconstruction cut criteria

In order to estimate the systematic uncertainties that come from the cut criteria that are used for strange particle reconstruction, a set of looser and tighter cuts compared to the nominal ones are checked.

Table 6.2: Summary of systematic uncertainties on $Y_{\mathrm{asym}}$ in pPbcollisions. The ranges quoted cover both the $p_{\mathrm{T}}$ and the rapidity dependence of the uncertainties.

| Source | $\mathrm{K}^0_{\mathrm{S}}$ (%) | $\Lambda$ (%) |
|---|---|---|
| Yield extraction | – | 0–3.0 |
| Selection criteria | 1.0–5.0 | 1.0–6.0 |
| Momentum resolution | 1.0 | 1.0 |
| Feed-down correction | – | 2.0–3.0 |
| Beam direction | 2.0–4.0 | 2.0–6.0 |
| Total ($Y_{\mathrm{asym}}$) | 2.4–6.5 | 3.2–9.3 |

The tight (loose) cut criteria for $V^0$ candidates are as follows:

- 3D distance of closest approach significance with respect to the primary vertex $>$ $2.5(1.5)$ for both daughter tracks,
- 3D distance of closest approach significance of the $V^0$ candidate to the primary vertex $< 2(3)$,
- 3D separation significance between $V^0$ vertex and primary vertex $> 3.5(2.5)$.

The tight (loose) cut criteria for $\Xi^-$ and $\Omega^-$ candidates are as follows:

- 3D distance of closest approach significance of proton track from $\Lambda$ decay with respect to the primary vertex $> 2.5(1.5)$
- 3D distance of closest approach significance of $\pi$ track from $\Lambda$ decay with respect to the primary vertex $> 3.5(2.5)$
- 3D distance of closest approach significance of $\pi$ (K) track from $\Xi^-$ ($\Omega^-$) decay with respect to the primary vertex $> 4.5(3.5)$
- 3D distance of closest approach significance of the $\Xi^-$ ($\Omega^-$) candidate with respect to the primary vertex $< 2.5(3.5)$

- 3D separation significance between $\Lambda$ vertex and primary vertex $> 11(9)$
- 3D separation significance between $\Xi^-$ ($\Omega^-$) vertex and primary vertex $> 2.5(1.5)$

Sample plots for $K^0_S$ are shown from Fig. 6.1 to Fig. 6.4. Considering the length of this writing, similar plots for other particles are not shown here.

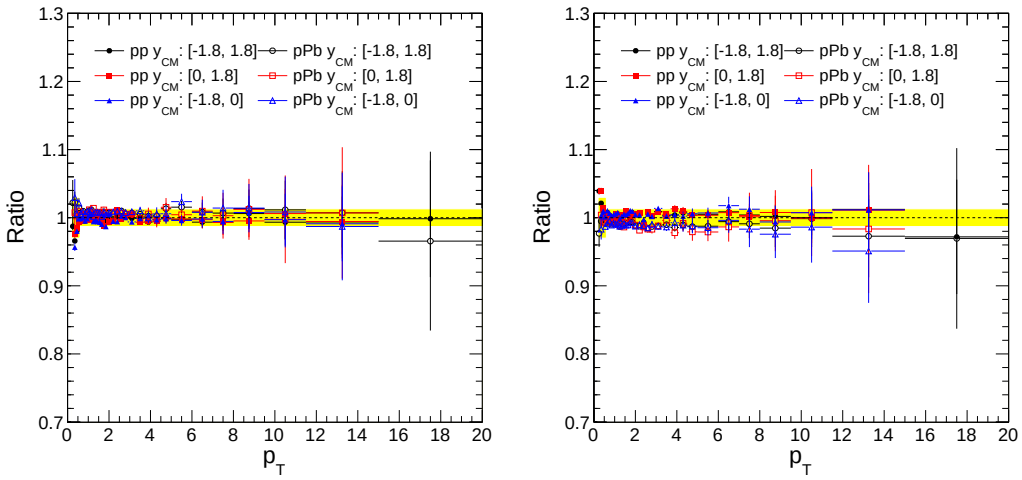


Figure 6.1: Ratio of $K^0_S$ spectra with looser (left) and tighter (right) cuts to the one with nominal cuts in pp and pPb for various $y_{CM}$ bins: [-1.8,1.8], [0,1.8], [-1.8,0]. The yellow band stands for the systematic uncertainty value quoted for this source.

### 6.2.2 Yield extraction

In this section, the systematic uncertainty sources related to the way signal counts are extracted are studied: background fitting function, fitting or counting to get yield counts. These two sources will be discussed in the following context.

To study how much measured spectra rely on the background fitting function forms, results with nominal background function are compared to results using third order polynomial as background function. In order to avoid the statistic fluctuation invades into the systematical effects, toy MC datasets are generated. The nominal signal and background function is

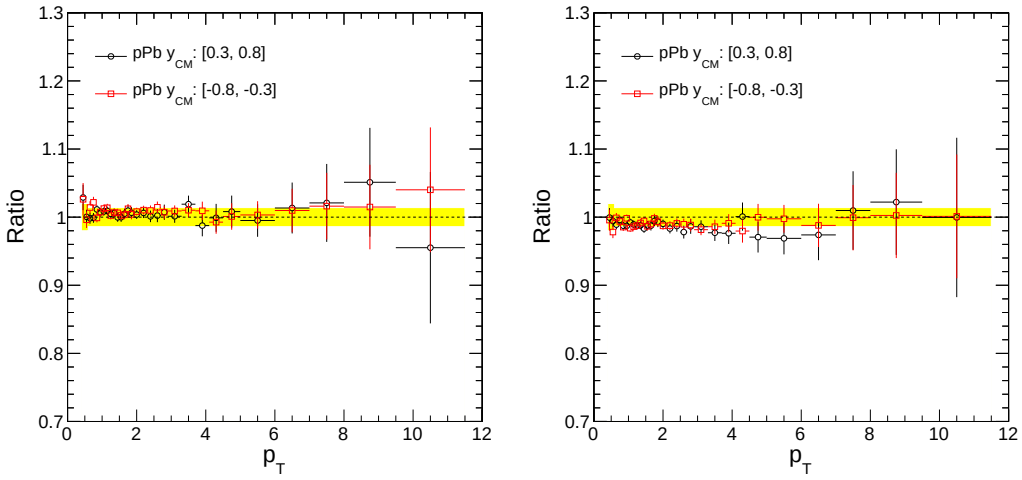


Figure 6.2: Ratio of $K^0_S$ spectra with looser (left) and tighter (right) cuts to the one with nominal cuts in pPb for various $y_{CM}$ bins: [-0.8,-0.3], [0.3,0.8]. The yellow band stands for the systematic uncertainty value quoted for this source.

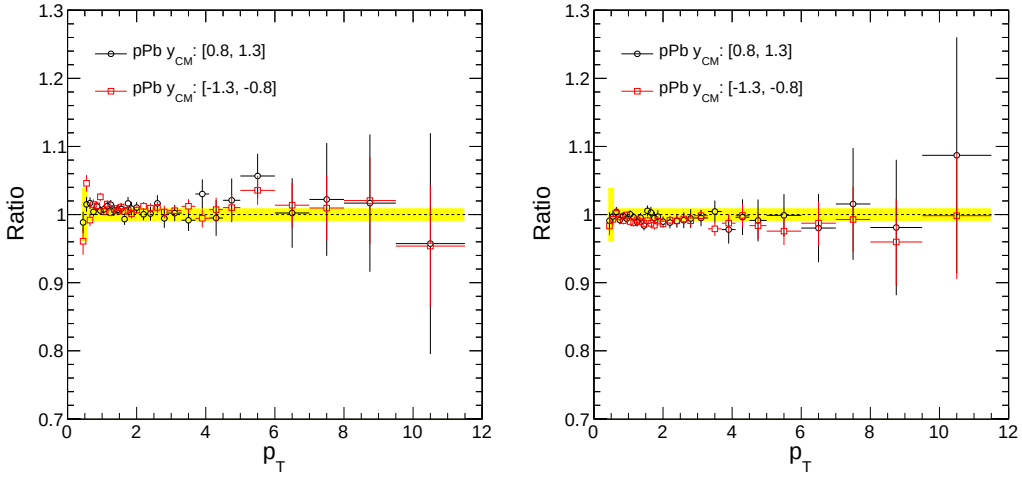


Figure 6.3: Ratio of $K^0_S$ spectra with looser (left) and tighter (right) cuts to the one with nominal cuts in pPb for various $y_{CM}$ bins: [-1.3,-0.8], [0.8,1.3]. The yellow band stands for the systematic uncertainty value quoted for this source.

used to fit data first. Then based on the combined probability distribution function (PDF) of signal and background function, 50K events are generated for each $p_T$, $y_{CM}$ bin. Then the generated toy MC dataset is fitted by a third order polynomial plus the nominal signal function. Particle yield obtained in this way is compared to the nominal yield. A sample

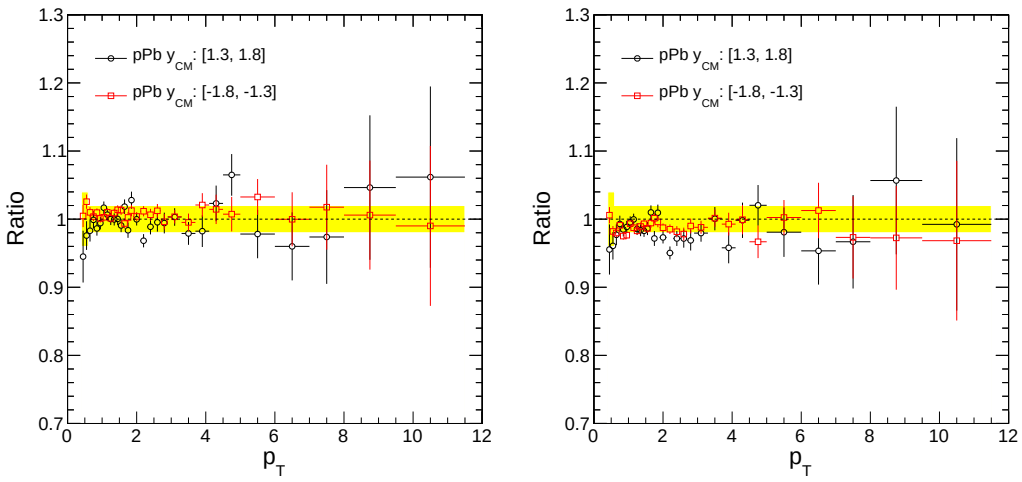


Figure 6.4: Ratio of $K^0_S$ spectra with looser (left) and tighter (right) cuts to the one with nominal cuts in pPb for various $y_{CM}$ bins: [-1.8,-1.3], [1.3,1.8]. The yellow band stands for the systematic uncertainty value quoted for this source.

of invariant mass distribution fittings of the toy MC for $K^0_S$ in pPb data is shown in Fig.6.5. The yield comparison plots for $K^0_S$ are shown from Fig.6.6 to Fig.6.9. In these plots, the legend "Pol3" represents yield obtained by fitting toy MC dataset generated with PDF of nominal signal function and 3rd order polynomial background function, while the legend "Nominal" means yield obtained with the nominal method.

Once the invariant mass distributions are fitted, the signal counts can be obtained either by integrating the signal function or by using side-band subtraction method as mentioned in Sec. 4.2. The comparison plots are shown from Fig.6.10 to Fig.6.13.

### 6.2.3 Rapidity binning

Since strange particles' rapidity distribution are not flat, the rapidity bins selected in this analysis may result in incorrect efficiency due to the large bin width. In order to estimate if there is a binning issue that could affect strange particles' $p_T$ spectra, the following procedures are deployed:

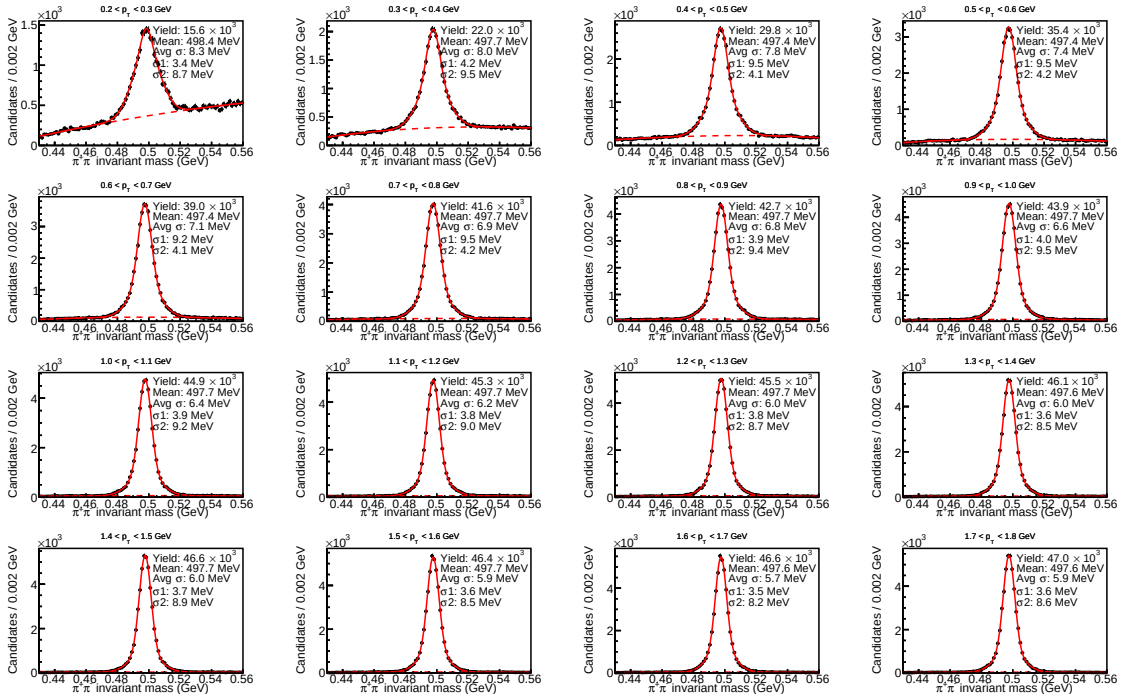


Figure 6.5: Generated toy MC invariant mass peaks of $K^0_S$ in pPb data fitted by third order polynomial plus the nominal signal function.

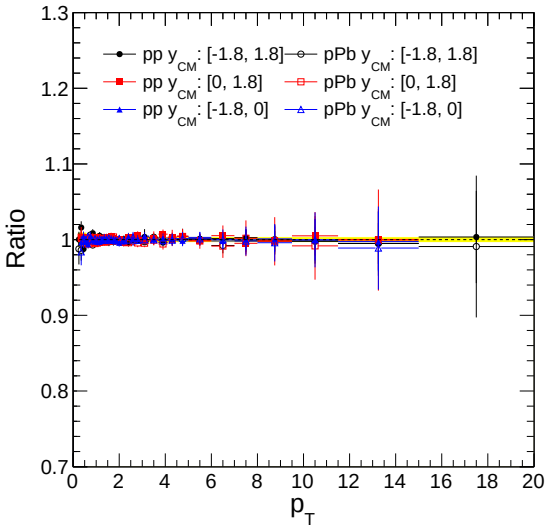


Figure 6.6: Ratio of $K^0_S$ yield obtained with third order polynomial background function form fit to toy MC generated with nominal signal and background PDF to the nominal yield in pp and pPb for various $y_{CM}$ bins: [-1.8,1.8], [0,1.8], [-1.8,0]. The yellow band stands for the systematic uncertainty value quoted for this source.

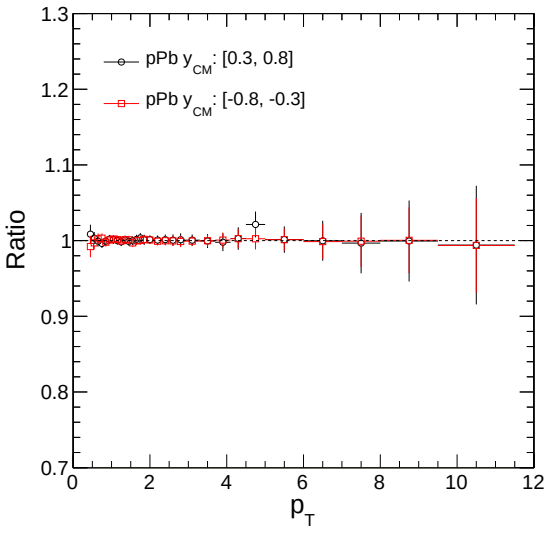


Figure 6.7: Ratio of $K^0_S$ yield obtained with third order polynomial background function form fit to toy MC generated with nominal signal and background PDF to the nominal yield in pPb for various $y_{CM}$ bins: [-0.8,-0.3], [0.3,0.8]. The yellow band stands for the systematic uncertainty value quoted for this source.

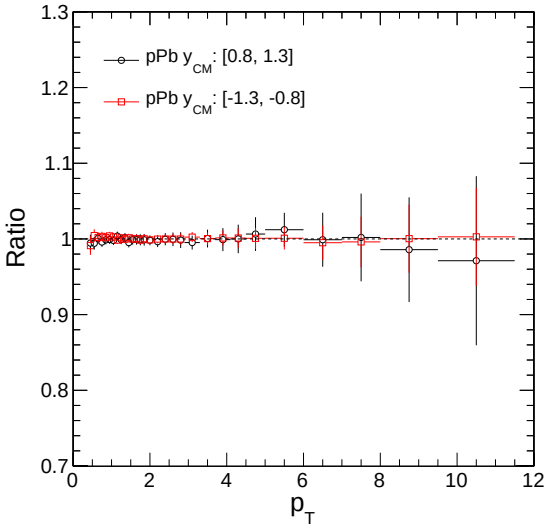


Figure 6.8: Ratio of $K^0_S$ yield obtained with third order polynomial background function form fit to toy MC generated with nominal signal and background PDF to the nominal yield in pPb for various $y_{CM}$ bins: [-1.3,-0.8], [0.8,1.3]. The yellow band stands for the systematic uncertainty value quoted for this source.

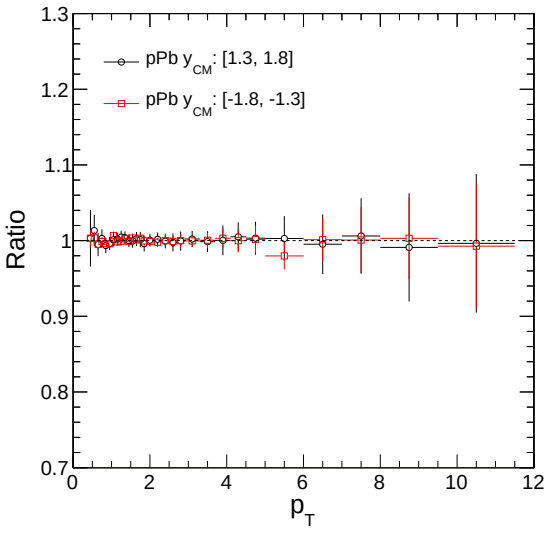


Figure 6.9: Ratio of $K^0_S$ yield obtained with third order polynomial background function form fit to toy MC generated with nominal signal and background PDF to the nominal yield in pPb for various $y_{CM}$ bins: [-1.8,-1.3], [1.3,1.8]. The yellow band stands for the systematic uncertainty value quoted for this source.

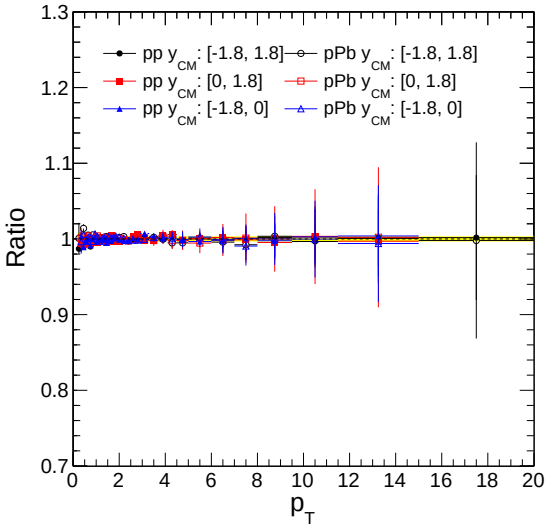


Figure 6.10: Ratio of $K^0_S$ using counting method to extract signal to the one using nominal method to extract signal in pp and pPb for various $y_{CM}$ bins: [-1.8,1.8], [0,1.8], [-1.8,0]. The yellow band stands for the systematic uncertainty value quoted for this source.

- Divide one default rapidity bins into two smaller bins, and calculate efficiency for each particle species in those smaller bins;

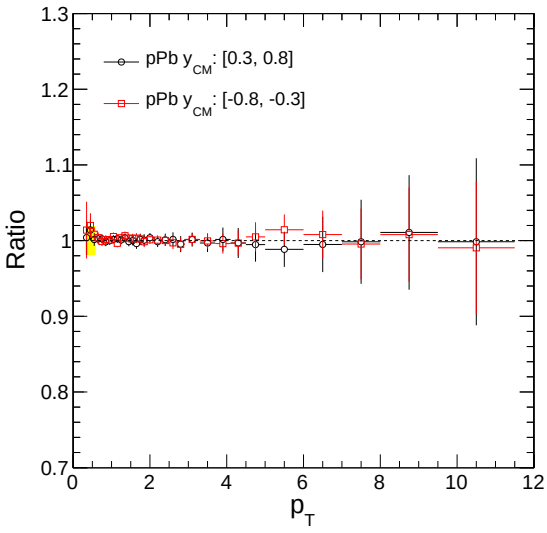


Figure 6.11: Ratio of $K^0_S$ using counting method to extract signal to the one using nominal method to extract signal in pPb for various $y_{CM}$ bins: [-0.8,-0.3], [0.3,0.8]. The yellow band stands for the systematic uncertainty value quoted for this source.

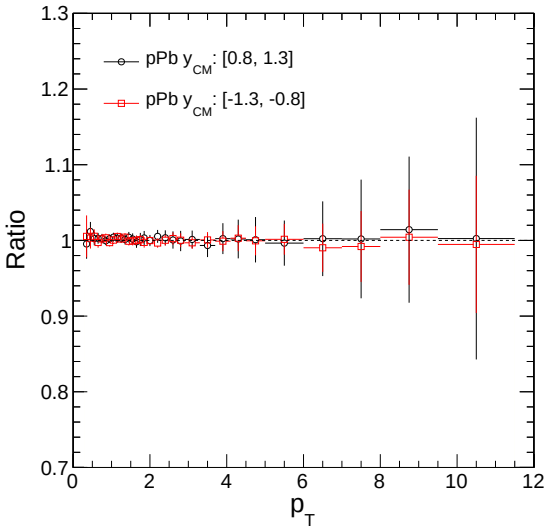


Figure 6.12: Ratio of $K^0_S$ using counting method to extract signal to the one using nominal method to extract signal in pPb for various $y_{CM}$ bins: [-1.3,-0.8], [0.8,1.3]. The yellow band stands for the systematic uncertainty value quoted for this source.

- Extract raw yield from smaller bins and get efficiency corrected spectra
- Merge spectra of the smaller bins into spectra of the default bin

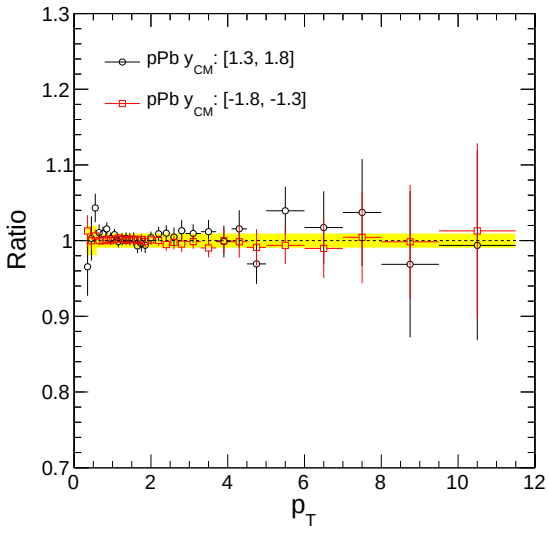


Figure 6.13: Ratio of $K^0_S$ using counting method to extract signal to the one using nominal method to extract signal in pPb for various $y_{\mathrm{CM}}$ bins: [-1.8,-1.3], [1.3,1.8]. The yellow band stands for the systematic uncertainty value quoted for this source.

- Compare the merged spectra with the nominal one

In principle, this method can check the effect of rapidity binning issue. However, since fitting invariant mass distribution needs to be performed for each $p_{\mathrm{T}}$ and $y_{CM}$ bins, this method is limited by statistics. Only bins with sufficient statistics can be checked, otherwise, the difference between merged spectra and nominal spectra could be a purely statistics issue. The comparison plots for $K^0_S$ are shown from Fig.6.14.

### 6.2.4 Momentum resolution

Since the detector does not have perfect momentum resolution, the momentum of each particle could have uncertainties due to the finite resolution, which could change the shape of strange particle $p_{\mathrm{T}}$ spectra. In order to investigate this issue, the iterative procedure is as follows:

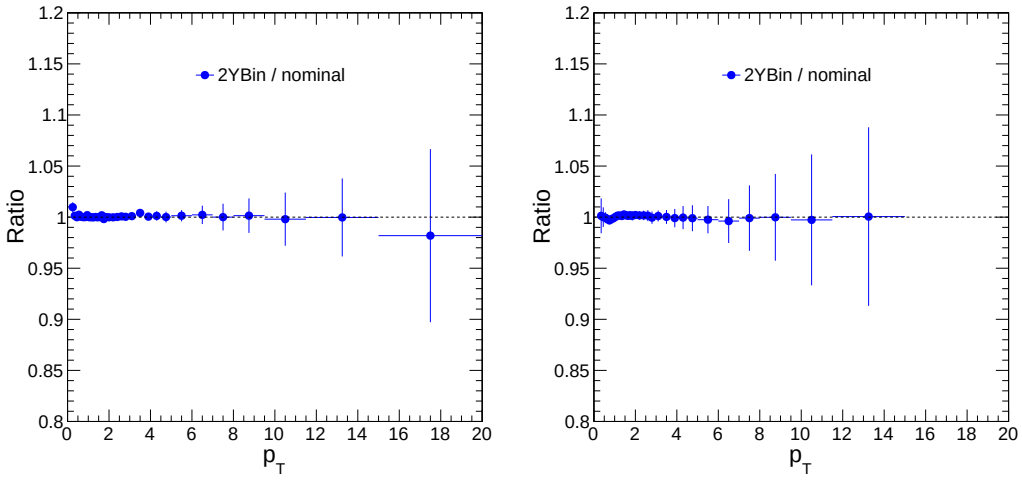


Figure 6.14: Ratio of $K^0_S$ merged spectra to nominal spectra in pp (left) and pPb (right) for $y_{CM}$ bin: [-1.8,1.8].

1. Determine the momentum resolution based on simulation and matching
2. Smearing the measured $p_T$ distribution with the momentum resolution.
3. Comparison of the original and the smeared $p_T$ distribution; the ratio of the two will be the initial resolution correction, the input for the iterative method
4. The resolution correction is applied on the original measured spectrum
5. Use the new resolution-corrected measured spectrum as input for step 2, 3, and 4. Repeat the procedure until a stable resolution correction are reached.

If the resolution correction turns out to be small in step 3, the iterative procedure is not needed.

The correlation between reconstructed and simulated $K^0_S$ $p_T$ in EPOS embedded $\hat{p_T}$ = 50 PYTHIA sample is shown in top left of Fig.6.15. The changes of bin width can be directly seen in the figure. In order to determine how wide $p_T$ bins should be chosen so that the derived resolution is not biased due to too wide $p_T$ bins, correlations of simulated and

reconstructed $p_{\mathrm{T}}$ values are filled into two dimensional histograms, which had $p_{\mathrm{T}}$ bin width from 12 MeV/c to 400 MeV/c. The computed $\mathrm{K}^0_{\mathrm{S}}$ $p_{\mathrm{T}}$ resolution are shown in the top right of Fig. 6.15. From the plot, it is clear that having finer $p_{\mathrm{T}}$ bins is very important at low $p_{\mathrm{T}}$. For the study of resolution smearing, the parameterization indicated in top right of Fig. 6.15 will be used.

The measured $p_{\mathrm{T}}$ distribution is fitted with a global fit function, shown in bottom left of Fig. 6.15. The combined global fit function is used to generate entries in a histogram, which has the same binning as the measurement. At the same time, a second histogram is filled with $p_{\mathrm{T}}$ values smeared according to the resolution parameterization. The ratio of the original and the smeared distribution is shown in bottom right of Fig. 6.15.

The same check is repeated for EPOS embedded particle gun samples for $\Lambda$, $\Xi^-$, and $\Omega^-$. However, due to the limitation of the length of this writing, these plots are not shown here.

### 6.2.5 Beam direction

In the middle of the 2013 pPb data taking, the direction of beam was reversed. In the first part of the data taking, the proton beam traveled to the negative z direction (Pbp), while for the second part, the proton beam traveled to the positive z direction (pPb). To ensure data taken from two beam directions can be combined, the spectra difference between the two beam directions are compared for $\mathrm{K}^0_{\mathrm{S}}$, $\Lambda$, $\Xi^-$, and $\Omega^-$. The results of $\mathrm{K}^0_{\mathrm{S}}$ are shown from Fig. 6.16 to Fig. 6.19.

### 6.2.6 Pileup

During the 2015 pp run, the condition that more than on collision happens in the same event is not negligible. The average pileup rate was approximately 0.9. In order to take

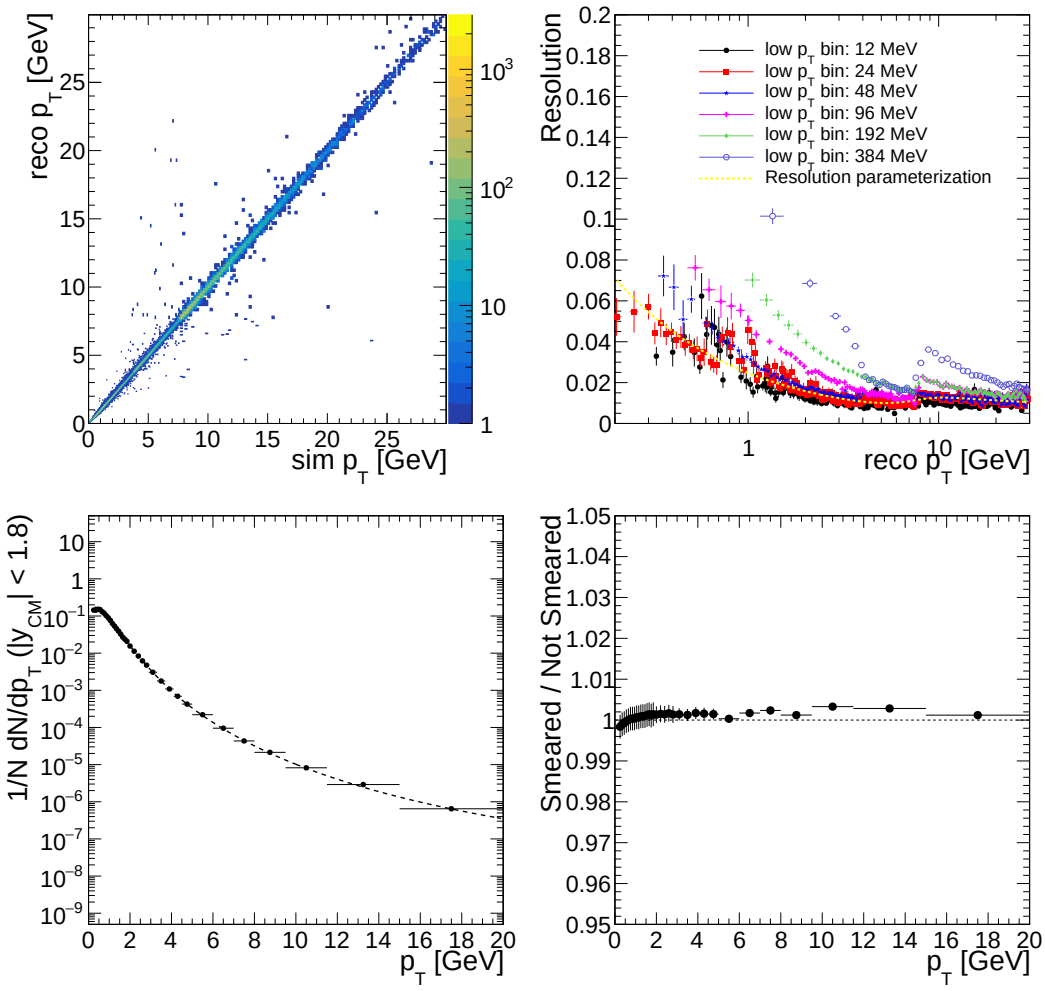


Figure 6.15: Top left: Correlation between simulated and reconstructed $K^0_S$ $p_T$ values in EPOS embedded $K^0_S$ particle gun sample. Top right: $K^0_S$ momentum resolution computed from EPOS embedded $K^0_S$ particle gun sample for various bin width. The derived resolution converges at low-$p_T$ as the bin width gets narrower. Bottom left: Measured $K^0_S$ $p_T$ distribution together with the combined global fit function. Bottom right: Ratio of not smeared $K^0_S$ $p_T$ spectrum to smeared spectrum with momentum resolution parameterization derived from EPOS embedded $K^0_S$ particle gun sample.

this into account, strange particles are selected as long as they are compatible with at least one reconstructed vertex, and the luminosity is used to normalize the pp strange particle spectra. In order to check this procedure, a comparison was made between strange particle spectra of pp collisions measured with all runs in the golden JSON [1] file and runs in the

[1] JSON format files used in CMS to describe which luminosity sections in which runs are considered good and should be processed.

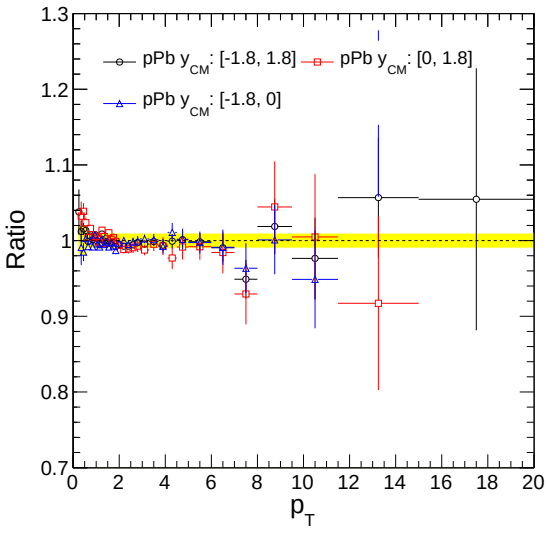


Figure 6.16: Ratio of $K^0_S$ $p_T$ distribution of pPb to the nominal combined spectra for $y_{CM}$ bin: [-1.8,1.8], [0,1.8], [-1.8,0]. The yellow band stands for the systematic uncertainty value quoted for this source.

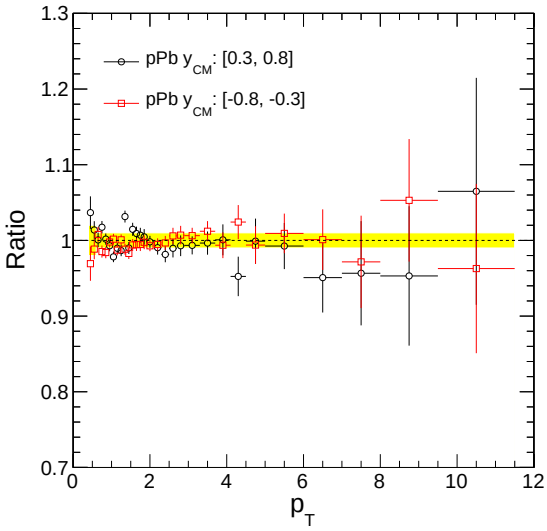


Figure 6.17: Ratio of $K^0_S$ $p_T$ distribution of pPb to the nominal combined spectra for $y_{CM}$ bin: [-0.8,-0.3], [0.3,0.8]. The yellow band stands for the systematic uncertainty value quoted for this source.

low pileup JSON file. The comparison plot for $K^0_S$ can be seen in Fig. 6.20.

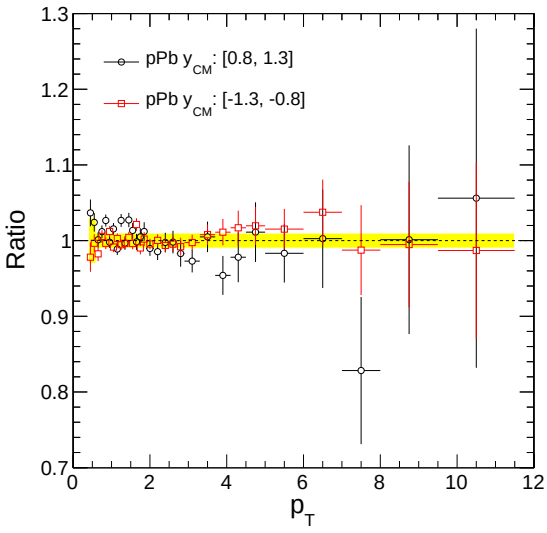


Figure 6.18: Ratio of $K^0_S$ $p_T$ distribution of pPb to the nominal combined spectra for $y_{CM}$ bin: [-1.3,-0.8], [0.8,1.3]. The yellow band stands for the systematic uncertainty value quoted for this source.

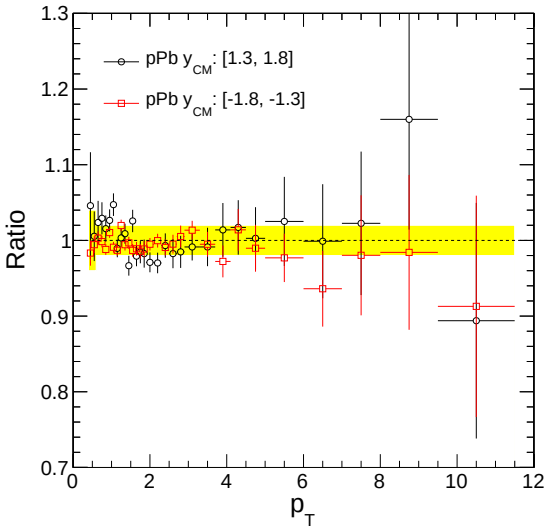


Figure 6.19: Ratio of $K^0_S$ $p_T$ distribution of pPb to the nominal combined spectra for $y_{CM}$ bin: [-1.8,-1.3], [1.3,1.8]. The yellow band stands for the systematic uncertainty value quoted for this source.

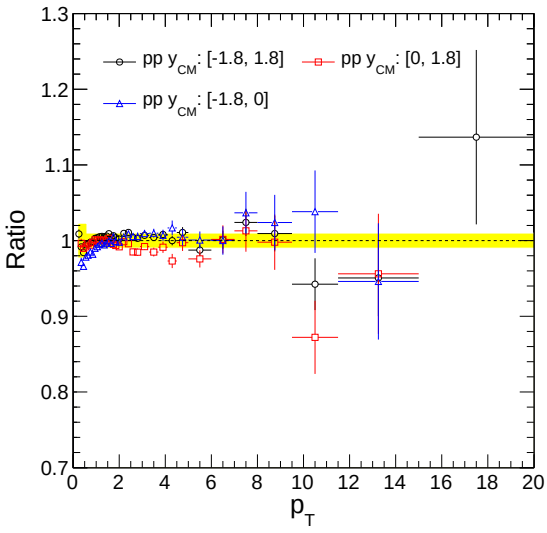


Figure 6.20: Ratio of $K^0_S$ spectra produced using all runs in the golden JSON file to that produced using runs in the lowPU JSON file for various $y_{CM}$ bins: [-1.8,1.8](left), [0,1.8](middle), [-1.8,0](right).

### 6.2.7 Data-MC difference in tracking efficiency

The difference in modeling tracking for data and MC is a significant source of systematic uncertainty for particle spectra. One way to estimate the difference is to study tracks coming from resonances (particularly of D mesons). One such study in CMS [84] has been done for the same pp dataset used in this analysis. According to the study, 4% is quoted as systematic uncertainty of data and MC difference in pp tracking. This number is also supported by previous studies [68], which measured the relative efficiency of reconstructing pion tracks in data and simulation. The method involves the reconstruction of $D^0$ mesons in pp collision data using two decay channels. One is $D^0 \to K^-\pi^+$, and the other is $D^0 \to K^-\pi^+\pi^-\pi^+$. $D^0$ mesons mentioned above is from the decay chain $D^{*+} \to D^0\pi^+$. By doing this, purity of the sample can be increased and it provides a common production sources. The ratio of branching fractions can be measured as:

$$R = \frac{N_{\mathrm{K}3\pi}}{N_{\mathrm{K}\pi}} \cdot \frac{\varepsilon_{\mathrm{K}\pi}}{\varepsilon_{\mathrm{K}3\pi}} \tag{6.2}$$

where the $N_{\mathrm{Kx}\pi}$ are the number of $D^0$ mesons from a specific decay channel, and $\varepsilon_{\mathrm{Kx}\pi}$ are the reconstruction efficiency of that channel. Assuming that simulation agrees with data perfectly, then $R$ should be equal to the true ratio of branching fractions, which is represented by the world-average ratio of branching fractions $R_{\mathrm{PDG}} = 2.08 \pm 0.05$. The relative tracking efficiency for pions in data and simulation can be estimated as:

$$\frac{\varepsilon_{\mathrm{data}}}{\varepsilon_{\mathrm{MC}}} = \sqrt{\frac{R}{R_{\mathrm{PDG}}}} \tag{6.3}$$

where the $\varepsilon_{\mathrm{data}}$ is the tracking efficiency of pions in data, while $\varepsilon_{\mathrm{MC}}$ is the tracking efficiency of pions in simulation. The final result of this technique was $\varepsilon_{\mathrm{data}}/\varepsilon_{\mathrm{MC}} = 1.007 \pm 0.034 \pm 0.014 \pm 0.012$, where the first uncertainty is statistical, the second is systematic, and the third is from the value of $R_{\mathrm{PDG}}$.

## 6.3 Results

Details of the results can be found in the paper to be published [79].

### 6.3.1 Invariant mass peaks

The invariant mass distributions of reconstructed $\mathrm{K}^0_{\mathrm{S}}$, $\Lambda$, $\Xi^-$, and $\Omega^-$ candidates in the range $-1.8 < y_{CM} < 1.8$ are shown in Fig. 6.21 for pPb events. Prominent mass peaks are visible, with little background. The solid lines show the results of a maximum likelihood

fit. The details of fitting function can be found in Sec. 4.2.1. These fit functions are found to provide a reasonable description of the signal and background with relatively few free parameters. The fits are performed over the ranges of strange-particle invariant masses indicated in Fig. 6.21 to obtain the raw strange-particle yield $N^{\text{raw}}_{\text{K}^0_\text{S}/\Lambda/\Xi^-/\Omega^-}$.

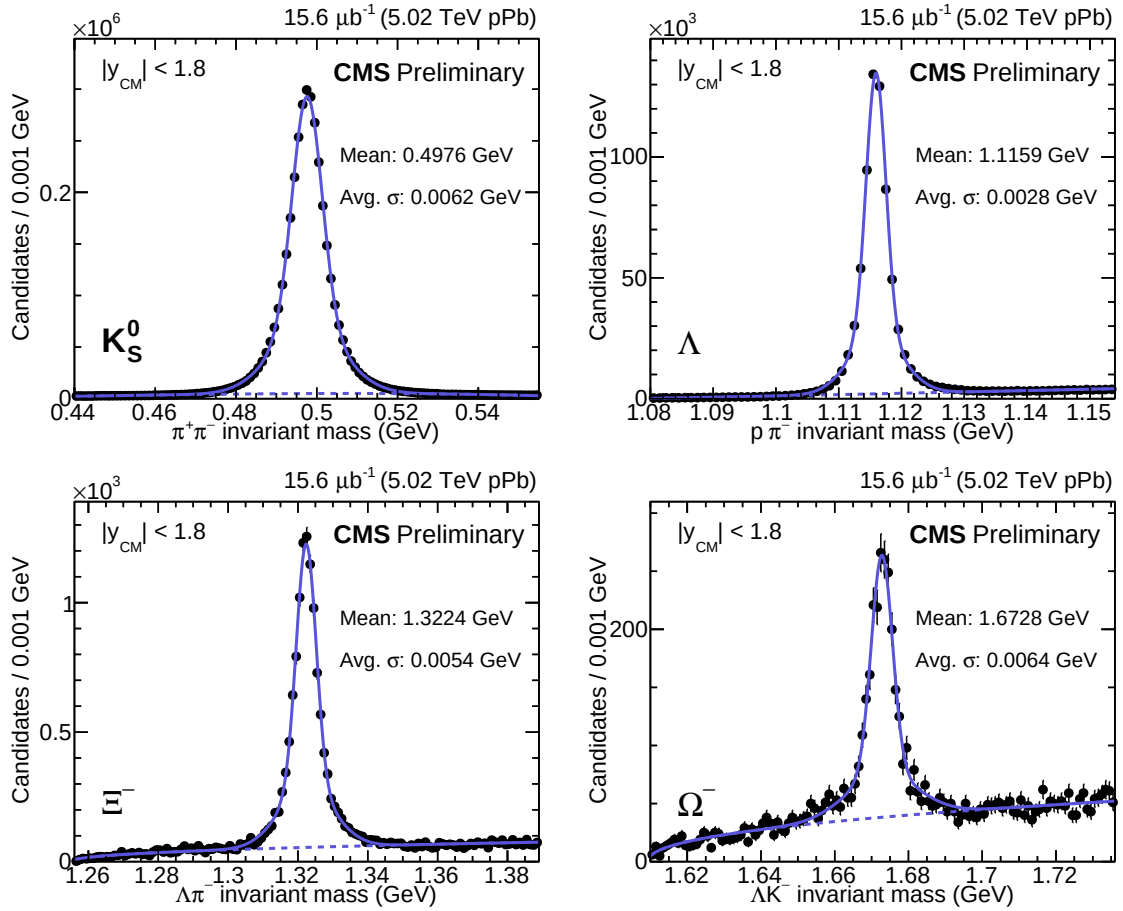


Figure 6.21: Invariant mass distribution of $\text{K}^0_\text{S}$ (top left), $\Lambda$ (top right), $\Xi^-$ (bottom left), and $\Omega^-$ (bottom right) candidates in $|y_{\text{CM}}| < 1.8$ in pPb collisions. The inclusion of the charge-conjugate states is implied for $\Lambda$, $\Xi^-$, and $\Omega^-$ particles. The solid lines show the results of fits described in the text. The dashed lines indicate the fitted background component.

### 6.3.2 Nuclear modification factor

The invariant $p_\text{T}$-differential spectra of $\text{K}^0_\text{S}$, $\Lambda$, $\Xi^-$, and $\Omega^-$ particles at $-1.8 < y_{CM} < 1.8$, $-1.8 < y_{CM} < 0$, and $0 < y_{CM} < 1.8$ in pp and pPb collisions at 5.02 TeV are presented in

Fig. 6.22. Due to statistical limitation, spectra of $\Omega^-$ is measured at only $-1.8 < y_{CM} < 1.8$. Invariant $p_{\mathrm{T}}$-differential yield is defined as the average number of particles per event weighted by $1/(2\pi p_{\mathrm{T}})$, for each $p_{\mathrm{T}}$ and $y_{CM}$ range. The pp spectrum, for the purpose of measuring the $R_{\mathrm{pPb}}$, is measured as a differential cross section with normalization determined from the integrated luminosity. In order to convert this quantity to a per-event yield for comparison on the same figure, a scaling factor of $70 \pm 5$ mb [62], corresponding approximately to the total inelastic pp cross section, is applied. To compare the strange-particle spectra in pp and pPb collisions directly, the spectra in pPb collisions are divided by the average number of binary nucleon-nucleon collisions, $\langle N_{\mathrm{coll}} \rangle = 6.9$, which is obtained from a Glauber MC simulation [38]. For purpose of better visibility, spectra for different $y_{CM}$ ranges are scaled by factors of $10^n$, with $-1.8 < y_{CM} < 1.8$ not scaled.

With the efficiency-corrected strange-particle spectra, the $R_{\mathrm{pPb}}$ of $\mathrm{K}^0_{\mathrm{S}}$, $\Lambda$, $\Xi^-$, and $\Omega^-$ are calculated in different $y_{CM}$ ranges. The Fig. 6.23 shows the $R_{\mathrm{pPb}}$ of each particle species at $-1.8 < y_{CM} < 1.8$. The $R_{\mathrm{pPb}}$ values of $\mathrm{K}^0_{\mathrm{S}}$ are consistent with unity for $p_{\mathrm{T}} > 2$ GeV. For baryons, the $R_{\mathrm{pPb}}$ values of $\mathrm{K}^0_{\mathrm{S}}$ of both $\Lambda$ and $\Xi^-$ reach unity at around 7 GeV. This is consistent with the charged-particle $R_{\mathrm{pPb}}$ [69, 85, 86], which also shows no modification in the $p_{\mathrm{T}}$ range from 7 to 20 GeV. In the intermediate $p_{\mathrm{T}}$ range from 3 to 6 GeV, Cronin-like enhancements are visible and clear mass ordering is observed for baryons with the greater mass showing larger $R_{\mathrm{pPb}}$. The observed mass ordering is consistent with expectations from the radial-flow effect in hydrodynamic models [80]. The calculation from EPOS LHC, including collective flow in pp and pPb collisions, are compared to data in Fig. 6.23. They indeed show clear mass ordering for baryon $R_{\mathrm{pPb}}$ in this $p_{\mathrm{T}}$ range, with even stronger mass dependence in the calculations. At higher $p_{\mathrm{T}}$, $R_{\mathrm{pPb}}$ calculated from EPOS LHC is clearly smaller than the data because of the strong screening in nuclear collisions in EPOS which reduces the number of binary collision in the initial state [54]. It is not clear from current measurements whether effects from recombination [87, 88, 89] play a role. This can be addressed by similar studies with more identified particles, such as the measurements of

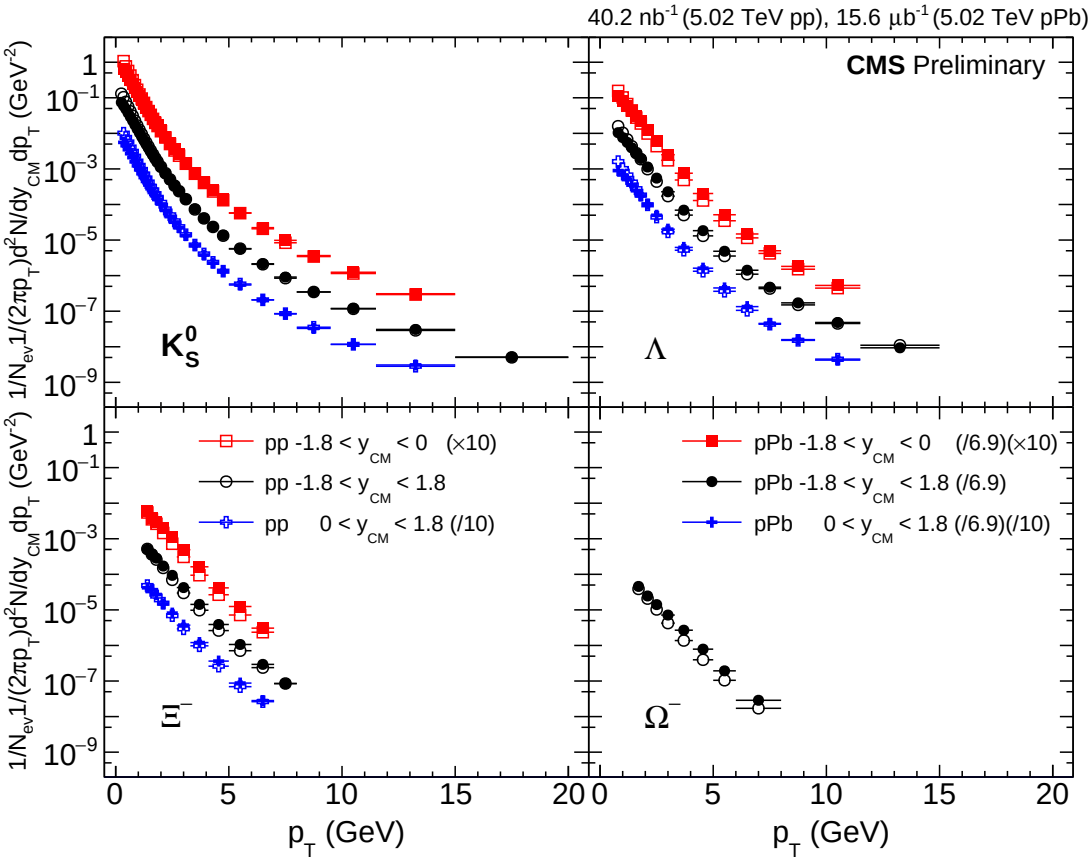


Figure 6.22: The invariant $p_{\mathrm{T}}$-differential spectra of $\mathrm{K}^0_{\mathrm{S}}$ (top left), $\Lambda$ (top right), $\Xi^-$ (bottom left), and $\Omega^-$ (bottom right) particles at $-1.8 < y_{\mathrm{CM}} < 1.8$, $-1.8 < y_{\mathrm{CM}} < 0$, and $0 < y_{\mathrm{CM}} < 1.8$ in pp and pPb collisions at $\sqrt{s_{NN}} = 5.02$ TeV. Spectra for different $y_{\mathrm{CM}}$ ranges are scaled by factors of $10^n$, with $-1.8 < y_{\mathrm{CM}} < 1.8$ not scaled. A factor of 70 mb is used to scale the pp spectra of strange particles from a differential cross section to a per-event yield. The error bars correspond to statistical uncertainties.

proton and $\phi$ meson $R_{\mathrm{dAu}}$ at RHIC [39]. For $p_{\mathrm{T}}$ less than 3 GeV, the predicted $R_{\mathrm{pPb}}$ values from EPOS LHC agree with data for each particle species. The values of $R_{\mathrm{pPb}}$ for $\mathrm{K}^0_{\mathrm{S}}$ and $\Lambda$ become less than unity for $p_{\mathrm{T}}$ less than 2 GeV, which is consistent with the $R_{\mathrm{pPb}}$ of charged particles in this $p_{\mathrm{T}}$ range and could be contributed to both, radial-flow and nuclear shadowing, effects.

The $R_{\mathrm{pPb}}$ values of $\mathrm{K}^0_{\mathrm{S}}$, $\Lambda$, and $\Xi^-$ particles for $-1.8 < y_{CM} < 0$ and $0 < y_{CM} < 1.8$ are presented as functions of $p_{\mathrm{T}}$ in Fig. 6.24. Because of the limited statistical precision,

the $R_{\rm pPb}$ of $\Omega^-$ baryon is not shown in the p- and Pb-going direction separately. The $R_{\rm pPb}$ of all three species are found to be larger in the Pb-going direction than the p-going direction, with a stronger mass splitting between the heavier and the lighter particles in the Pb-going direction. This trend is consistent with expectations from the radial-flow effect in hydrodynamic models. The Cronin effect with the parton multiple scattering interpretation predicts a stronger enhancement in the p-going direction with a larger $R_{\rm pPb}$ on the p-going side, which is inconsistent with data. However, this could be explained by the prediction that this effect is small compared to the nuclear shadowing effect [90] at the LHC energies. The accessed parton momentum fraction, x, in the nucleus is less than 0.02 for the $p_{\rm T}$ and rapidity considered in this analysis. Therefore, these measurements are sensitive to the shadowing effect, and $R_{\rm pPb}$ should be smaller in the p-going direction because the accessed x fractions in the nucleus are smaller.

### 6.3.3 The particle yield rapidity asymmetry of $\rm K^0_S$ and $\Lambda$ particles

The invariant $p_{\rm T}$-differential spectra of $\rm K^0_S$ and $\Lambda$ at $-1.8 < y_{CM} < -1.3$, $-1.3 < y_{CM} < -0.8$, $-0.8 < y_{CM} < -0.3$, $0.3 < y_{CM} < 0.8$, $0.8 < y_{CM} < 1.3$, and $1.3 < y_{CM} < 1.8$ in pPb collisions at $\sqrt{s_{NN}}$ = 5.02 TeV are presented in Fig. 6.25. Spectra in different $y_{CM}$ ranges are scaled by factors of $10^{\rm n}$, with $-0.8 < y_{CM} < -0.3$ not scaled.

The Fig. 6.26 shows the $Y_{\rm asym}$ as functions of $p_{\rm T}$ for $\rm K^0_S$ and $\Lambda$ for different rapidity ranges. It is found that $Y_{\rm asym}$ of both $\rm K^0_S$ and $\Lambda$ in the forward $Y_{\rm asym}$ ranges rise up to a certain $p_{\rm T}$, and then approach unity at higher $p_{\rm T}$. The values of $Y_{\rm asym}$ are larger than one in all three rapidity ranges. The observed $Y_{\rm asym}$ are larger in the forward region, consistent with expectations from nuclear shadowing. The $Y_{\rm asym}$ of $\rm K^0_S$ and $\Lambda$ in the above three $y_{CM}$ ranges are compared to the $Y_{\rm asym}$ of charged particles in similar $\eta_{\rm CM}$ ranges. It is found that the $Y_{\rm asym}$ of $\rm K^0_S$ and $\Lambda$ are larger than that of charged particles, and the $p_{\rm T}$ value of the charged-

particle $Y_{\mathrm{asym}}$ peak is between that of $\mathrm{K}^0_{\mathrm{S}}$ and $\Lambda$ in forward $|y_{CM}|$ ranges. These detailed structures, with mass dependence or meson-baryon difference, can provide constraints to models such as hydrodynamic and recombination, which also have mass ordering effect and number of constituent quark difference, respectively. The results of $Y_{\mathrm{asym}}$ are compared to EPOS LHC calculations in the three rapidity ranges. The calculated $Y_{\mathrm{asym}}$ increases from mid-rapidity to forward rapidity, consistent with the trend in data, but fails to describe the particle species dependence at forward rapidities.

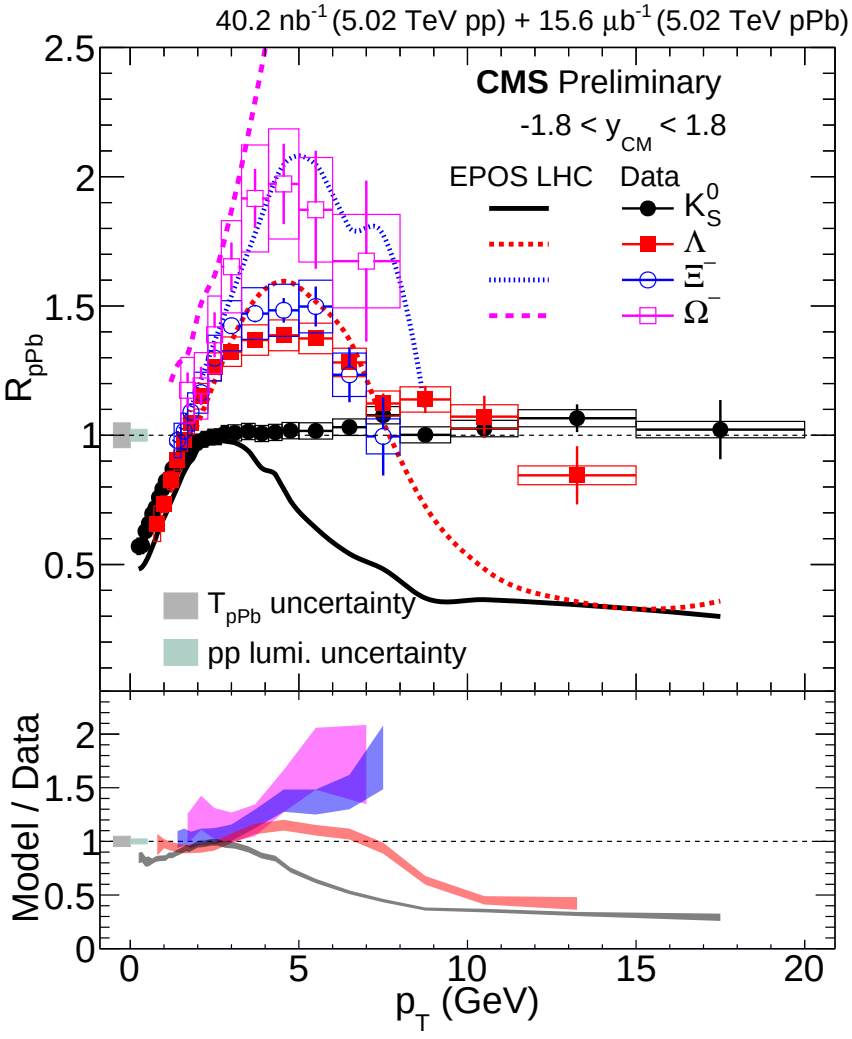


Figure 6.23: (Top) Nuclear modification factors of $K^0_S$ (black filled circles), $\Lambda$ (red filled squares), $\Xi^-$ (blue open circles), and $\Omega^-$ (purple open squares) at $-1.8 < y_{CM} < 1.8$ in pPb collisions are presented. The error bars correspond to statistical uncertainties, while the boxes around the markers denote the systematic uncertainties. The $T_{pPb}$ and pp integrated luminosity uncertainties are represented by the shaded areas around one. The results are compared to EPOS LHC predictions including collective flow in pp and pPb collisions. The data and predictions share the same color for each particle species. (Bottom) The ratios of nuclear modification factors of $K^0_S$, $\Lambda$, $\Xi^-$, and $\Omega^-$ of EPOS LHC to measurements are shown. The bands represent the combination of statistical uncertainties and systematic uncertainties.

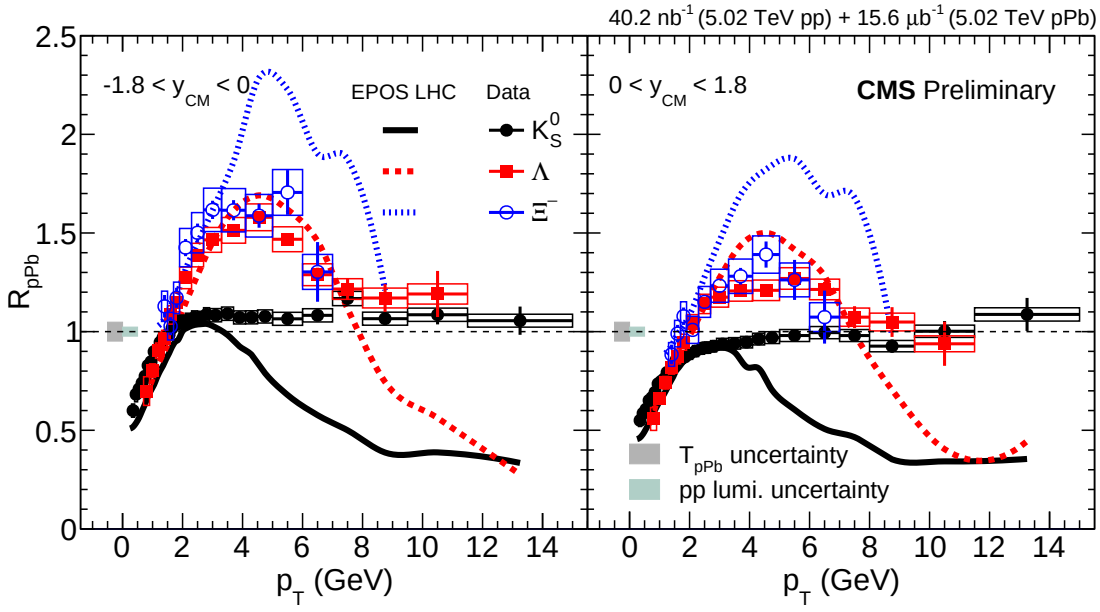


Figure 6.24: Nuclear modification factors of $K^0_S$ (black filled circles), $\Lambda$ (red filled squares), and $\Xi^-$ (blue open circles) at $-1.8 < y_{\mathrm{CM}} < 0$ (left) and $0 < y_{\mathrm{CM}} < 1.8$ (right) in pPb collisions are presented. The error bars correspond to statistical uncertainties, while the boxes around the markers denote the systematic uncertainties. The $T_{\mathrm{pPb}}$ and pp integrated luminosity uncertainties are represented by the shaded areas around one. The results are compared to EPOS LHC predictions including collective flow in pp and pPb collisions. The data and predictions share the same color for each particle species.

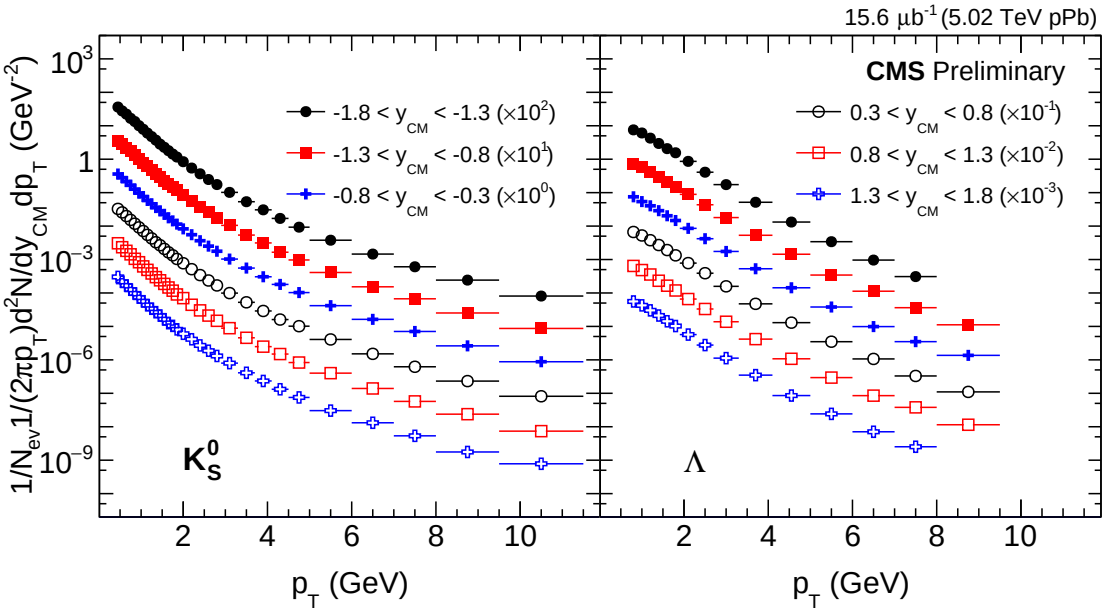


Figure 6.25: The invariant $p_{\mathrm{T}}$-differential spectra of $\mathrm{K}^0_{\mathrm{S}}$ (left) and $\Lambda$ (right) particles at $-1.8 < y_{\mathrm{CM}} < -1.3$, $-1.3 < y_{\mathrm{CM}} < -0.8$, $-0.8 < y_{\mathrm{CM}} < -0.3$, $0.3 < y_{\mathrm{CM}} < 0.8$, $0.8 < y_{\mathrm{CM}} < 1.3$, and $1.3 < y_{\mathrm{CM}} < 1.8$ in pPb collisions at $\sqrt{s_{NN}}$ = 5.02 TeV. Spectra in different $y_{\mathrm{CM}}$ ranges are scaled by factors of $10^n$, with $< -0.8 < y_{\mathrm{CM}} < -0.3$ not scaled. The error bars correspond to statistical uncertainties.

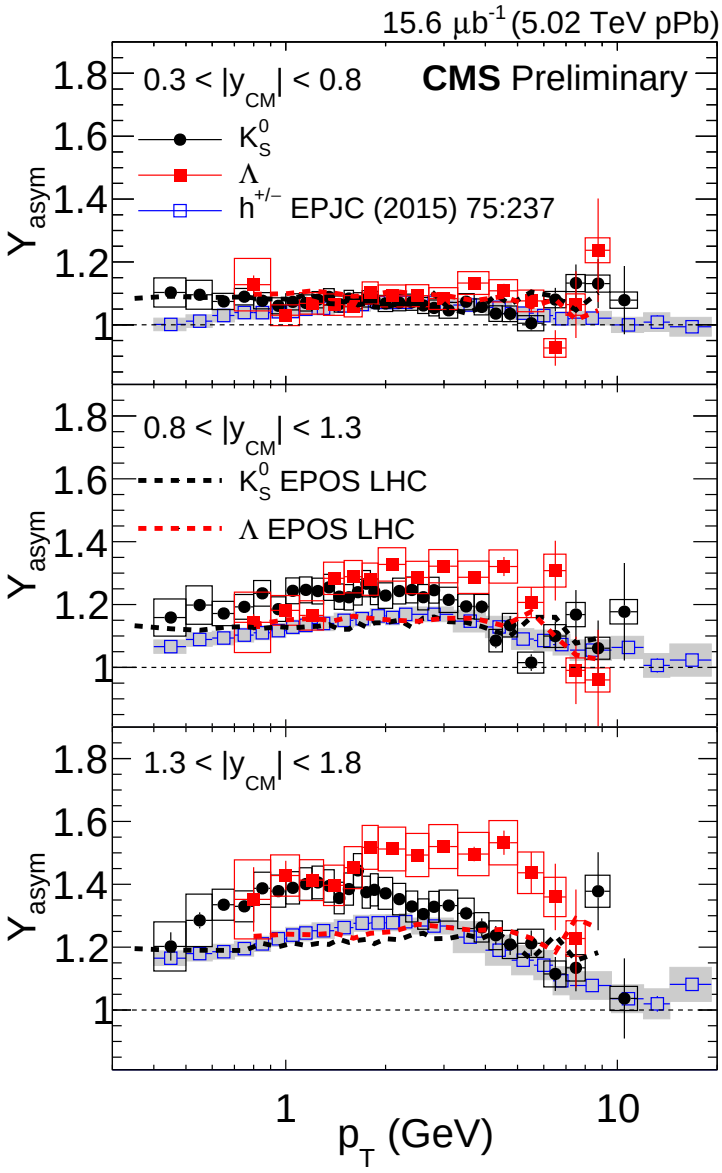


Figure 6.26: $Y_{\text{asym}}$ of $K^0_S$ (black filled circles), $\Lambda$ (red filled squares), and charged particles (blue open squares) at $0.3 < |y_{\text{CM}}| < 0.8$, $0.8 < |y_{\text{CM}}| < 1.3$, and $1.3 < |y_{\text{CM}}| < 1.8$ ($|\eta_{\text{CM}}|$ ranges for charged particles) in pPb collisions at $\sqrt{s_{NN}}$ = 5.02 TeV. The error bars correspond to statistical uncertainties, while the boxes around the markers denote the systematic uncertainties. The results are compared to EPOS LHC predictions including collective flow in pp and pPb collisions. The data and predictions share the same color for each particle species.

# Chapter 7

## Discussion and conclusion

As mentioned above, the thesis has two goals. The first is to study the effect of radial flow on the particle spectra with the help of CMS high-multiplicity triggers. The other goal is to investigate the particle production mechanism with the measurements of nuclear modification factor, $R_{\mathrm{pPb}}$, and particle yield rapidity asymmetry, $Y_{\mathrm{asym}}$.

To achieve the first goal, measurements of $\mathrm{K}^0_{\mathrm{S}}$, $\Lambda$, and $\Xi^-$ transverse momentum, $p_{\mathrm{T}}$, spectra in pp, pPb, and PbPb collisions are performed over a wide range of charged particle multiplicity. With these spectra, particle yield ratios, $\Lambda/\mathrm{K}^0_{\mathrm{S}}$ and $\Xi^-/\Lambda$, are calculated. A clear mass effect on the particle ratios is observed, and the results are consistent with the expectation of hydrodynamic models. The average transverse kinetic energy, $\langle KE_{\mathrm{T}} \rangle$, is also calculated. The results show that $\langle KE_{\mathrm{T}} \rangle$ in small systems behave similar as the heavy ion collisions. This is also consistent with the expectation of hydrodynamic models. One caveat of this analysis is that the center-of-mass energy of pp, pPb, and PbPb collisions available at that time were different. The center-of-mass energy may have an effect on the spectra as well. Fortunately, CMS has data of pp, pPb, and PbPb at 5.02 TeV available now. A similar analysis can be performed to determine the effect of center-of-mass energy on particle spectra.

For the second goal, measurements of $\mathrm{K}^0_{\mathrm{S}}$, $\Lambda$, $\Xi^-$, and $\Omega^-$ transverse momentum, $p_{\mathrm{T}}$, spectra in pp and pPb collision at 5.02 TeV are measured. Based on these spectra, $R_{\mathrm{pPb}}$ and $Y_{\mathrm{asym}}$ are calculated. The results of $R_{\mathrm{pPb}}$ and $Y_{\mathrm{asym}}$ are consistent with the expectation of radial flow, recombination, and nuclear shadowing effect, and disfavor the multiple scattering interpretation of Cronin effect. However, with current measurements it is not possible

to distinguish these effects. To improve this, theoretical predictions of these effects are needed. With the comparison of data and theoretical predictions, each effect can be understood better. One more improvement is to have the measurement of $\phi$ mesons, because it is a meson and has mass that is close to $\Lambda$ baryon. With the measurement of $\phi$ mesons, the effect of radial flow and recombination may be disentangled.

The measurement of strangeness in different collision systems is intriguing. More measurements and theoretical calculations should be done to improve our understanding of the deconfined QCD phase at high temperature and energy density.

# BIBLIOGRAPHY


[1] C. Patrignani et al. Review of Particle Physics. *Chin. Phys.*, C40(10):100001, 2016.

[2] Tim Kolar. Qcd matter phase diagram. http://mafija.fmf.uni-lj.si/seminar/files/2014_2015/seminar_v3-skrajsana.pdf, 2014. Online; accessed 29-June-2018.

[3] F. Karsch. Lattice QCD at high temperature and density. *Lect. Notes Phys.*, 583:209–249, 2002.

[4] Shusu Shi. *Event anisotropy $v_2$ at STAR*. PhD thesis, Hua-Zhong Normal U., 2010.

[5] The CMS Collaboration. Observation and studies of jet quenching in pbpb collisions at $\sqrt{s_{NN}} = 2.76$ tev. *Phys. Rev. C*, 84:024906, Aug 2011.

[6] Torbjörn Sjöstrand et al. An introduction to pythia 8.2. *Computer Physics Communications*, 191:159 – 177, 2015.

[7] Peter Jacobs and Xin-Nian Wang. Matter in extremis: ultrarelativistic nuclear collisions at rhic. *Progress in Particle and Nuclear Physics*, 54(2):443 – 534, 2005.

[8] Wikimedia Commons. File:standard model of elementary particles.svg — wikimedia commons, the free media repository, 2018. [Online; accessed 3-July-2018].

[9] Didier Alexandre. Hyperon production in p-pb collisions with alice at the lhc. December 2016.

[10] The ALICE Collaboration. $K^0_S$ and $\Lambda$ production in pb-pb collisions at $\sqrt{s_{NN}}$=2.76 TeV. *Phys. Rev. Lett.*, 111:222301, Nov 2013.

[11] Multi-strange baryon production at mid-rapidity in pbpb collisions at snn=2.76 tev. *Physics Letters B*, 728:216 – 227, 2014.

[12] Jaroslav Adam et al. Enhanced production of multi-strange hadrons in high-multiplicity proton-proton collisions. *Nature Phys.*, 13:535, 2017.

[13] The PHENIX Collaboration. Spectra and ratios of identified particles in au+au and $d$+au collisions at $\sqrt{s_{NN}} = 200$ gev. *Phys. Rev. C*, 88:024906, Aug 2013.

[14] Long-range two-particle correlations of strange hadrons with charged particles in ppb and pbpb collisions at lhc energies. *Physics Letters B*, 742:200 – 224, 2015.

[15] Lyndon Evans and Philip Bryant. Lhc machine. *Journal of Instrumentation*, 3(08):S08001, 2008.

[16] M Friedl. The CMS silicon strip tracker and its electronic readout. 2001.

[17] The CMS Collaboration. The cms experiment at the cern lhc. *Journal of Instrumentation*, 3(08):S08004, 2008.

[18] CMS Collaboration. Projected Performance of an Upgraded CMS Detector at the LHC and HL-LHC: Contribution to the Snowmass Process. *ArXiv e-prints*, July 2013.

[19] https://indico.desy.de/indico/event/1964/session/26/contribution/212/material/slides/0.pdf.

[20] https://physicsworld.com/a/a-strange-quark-plasma/.

[21] https://www.uni-muenster.de/imperia/md/content/physik_kp/agwessels/thesis_db/ag_wessels/baumeier_2011_bachelor.pdf.

[22] https://twiki.cern.ch/twiki/bin/view/CMSPublic/PhysicsResultsHIN13002.

[23] Matthias Troyer and Uwe-Jens Wiese. Computational complexity and fundamental limitations to fermionic quantum monte carlo simulations. *Phys. Rev. Lett.*, 94:170201, May 2005.

[24] K. Fukushima and T. Hatsuda. The phase diagram of dense QCD. *Reports on Progress in Physics*, 74(1):014001, January 2011.

[25] Frithjof Karsch. Lattice results on QCD thermodynamics. *Nucl. Phys.*, A698:199–208, 2002.

[26] R. Rapp, T. Schäfer, E. Shuryak, and M. Velkovsky. Diquark bose condensates in high density matter and instantons. *Phys. Rev. Lett.*, 81:53–56, Jul 1998.

[27] Mark G. Alford, Andreas Schmitt, Krishna Rajagopal, and Thomas Schäfer. Color superconductivity in dense quark matter. *Rev. Mod. Phys.*, 80:1455–1515, 2008.

[28] W. Greiner, H. Curien, H. Aksas, L. Neise, and H. Stöcker. *Thermodynamique et mécanique statistique*. Springer Berlin Heidelberg, 1999.

[29] Johann Rafelski and Berndt Muller. Strangeness Production in the Quark - Gluon Plasma. *Phys. Rev. Lett.*, 48:1066, 1982. [Erratum: Phys. Rev. Lett.56,2334(1986)].

[30] J. Sollfrank and U. Heinz. *The Role of Strangeness in Ultrarelativistic Nuclear Collisions*, pages 555–634. World Scientific Publishing Co, 1995.

[31] Xin-Nian Wang and Miklos Gyulassy. Gluon shadowing and jet quenching in a+a collisions at $\sqrt{}$s =200a gev. *Phys. Rev. Lett.*, 68:1480–1483, Mar 1992.

[32] Xin-Nian Wang, Zheng Huang, and Ina Sarcevic. Jet quenching in the direction opposite to a tagged photon in high-energy heavy-ion collisions. *Phys. Rev. Lett.*, 77:231–234, Jul 1996.

[33] M. Gyulassy, I. Vitev, X.-N. Wang, and B.-W. Zhang. *Jet Quenching and Radiative Energy Loss in Dense Nuclear Matter*, pages 123–191. World Scientific Publishing Co, 2004.

[34] A. Kovner and U. A. Wiedemann. *Gluon Radiation and Parton Energy Loss*, pages 192–248. World Scientific Publishing Co, 2004.

[35] P. Huovinen. *Hydrodynamical Description of Collective Flow*, pages 600–633. World Scientific Publishing Co, 2004.

[36] Jean-Yves Ollitrault. Anisotropy as a signature of transverse collective flow. *Phys. Rev. D*, 46:229–245, Jul 1992.

[37] W. Reisdorf and H. G. Ritter. Collective flow in heavy-ion collisions. *Annual Review of Nuclear and Particle Science*, 47(1):663–709, 1997.

[38] Raimond Snellings. Elliptic flow: a brief review. *New Journal of Physics*, 13(5):055008, 2011.

[39] The CMS Collaboration. Observation of long-range, near-side angular correlations in ppb collisions at the lhc. *Physics Letters B*, 718(3):795 – 814, 2013.

[40] Multiplicity and transverse momentum dependence of two- and four-particle correlations in ppb and pbpb collisions. *Physics Letters B*, 724(4):213 – 240, 2013.

[41] The CMS Collaboration. Evidence for collective multiparticle correlations in $p-$Pb collisions. *Phys. Rev. Lett.*, 115:012301, Jun 2015.

[42] Evidence for collectivity in pp collisions at the lhc. *Physics Letters B*, 765:193 – 220, 2017.

[43] The CMS Collaboration. Measurement of inclusive jet production and nuclear modifications in ppb collisions at 5.02 tev. *The European Physical Journal C*, 76(7):372, Jul 2016.

[44] Measurement of charged jet production cross sections and nuclear modification in ppb collisions at snn=5.02 tev. *Physics Letters B*, 749:68 – 81, 2015.

[45] M. Gell-Mann. A schematic model of baryons and mesons. *Physics Letters*, 8(3):214 – 215, 1964.

[46] G. Zweig. An SU(3) model for strong interaction symmetry and its breaking. Version 1. 1964.

[47] G. Zweig. An SU(3) model for strong interaction symmetry and its breaking. Version 2. In D.B. Lichtenberg and Simon Peter Rosen, editors, *DEVELOPMENTS IN THE QUARK THEORY OF HADRONS. VOL. 1. 1964 - 1978*, pages 22–101. 1964.

[48] Michael L. Miller, Klaus Reygers, Stephen J. Sanders, and Peter Steinberg. Glauber modeling in high-energy nuclear collisions. *Annual Review of Nuclear and Particle Science*, 57(1):205–243, 2007.

[49] https://twiki.cern.ch/twiki/bin/view/CMSPublic/LumiPublicResults.

[50] https://home.cern/about/updates/2017/11/record-luminosity-well-done-lhc.

[51] M. Garcia-Sciveres and N. Wermes. A review of advances in pixel detectors for experiments with high rate and radiation. *Reports on Progress in Physics*, 81(6):066101, June 2018.

[52] The CMS Collaboration. Strange particle production in pp collisions at 0.9 and 7 tev. *Journal of High Energy Physics*, 2011(5):64, May 2011.

[53] The CMS Collaboration. Multiplicity and rapidity dependence of strange hadron production in pp, ppb, and pbpb collisions at the lhc. *Physics Letters B*, 768:103 – 129, 2017.

[54] Klaus Werner, Fu-Ming Liu, and Tanguy Pierog. Parton ladder splitting and the rapidity dependence of transverse momentum spectra in deuteron-gold collisions at the bnl relativistic heavy ion collider. *Phys. Rev. C*, 74:044902, Oct 2006.

[55] T. Pierog, Iu. Karpenko, J. M. Katzy, E. Yatsenko, and K. Werner. Epos lhc: Test of collective hadronization with data measured at the cern large hadron collider. *Phys. Rev. C*, 92:034906, Sep 2015.

[56] J. Podolanski and R. Armenteros. Iii. analysis of v-events. *The London, Edinburgh, and Dublin Philosophical Magazine and Journal of Science*, 45(360):13–30, 1954.

[57] Wouter Verkerke and David P. Kirkby. The RooFit toolkit for data modeling. *eConf*, C0303241:MOLT007, 2003. [,186(2003)].

[58] R. Brun and F. Rademakers. ROOT: An object oriented data analysis framework. *Nucl. Instrum. Meth.*, A389:81–86, 1997.

[59] S. Agostinelli et al. GEANT4: A Simulation toolkit. *Nucl. Instrum. Meth.*, A506:250–303, 2003.

[60] https://twiki.cern.ch/twiki/bin/view/CMSPublic/WorkBookGenParticleCandidate.

[61] https://twiki.cern.ch/twiki/bin/view/CMSPublic/SWGuideGenParticleFromSim.

[62] Xin-Nian Wang and Miklos Gyulassy. hijing: A monte carlo model for multiple jet production in pp, pA, and AA collisions. *Phys. Rev. D*, 44:3501–3516, Dec 1991.

[63] The CMS Collaboration. Charged-particle nuclear modification factors in pbpb and ppb collisions at 5.02 tev. *Journal of High Energy Physics*, 2017(4):39, Apr 2017.

[64] J.-Y. Ollitrault. Reconstructing azimuthal distributions in nucleus-nucleus collisions. *ArXiv Nuclear Experiment e-prints*, November 1997.

[65] S. Voloshin and Y. Zhang. Flow study in relativistic nuclear collisions by fourier expansion of azimuthal particle distributions. *Zeitschrift für Physik C Particles and Fields*, 70(4):665–671, Dec 1996.

[66] A. M. Poskanzer and S. A. Voloshin. Methods for analyzing anisotropic flow in relativistic nuclear collisions. *Phys. Rev. C*, 58:1671–1678, Sep 1998.

[67] The CMS Collaboration. Measurement of the elliptic anisotropy of charged particles produced in pbpb collisions at $\sqrt{s_{NN}} = 2.76$ tev. *Phys. Rev. C*, 87:014902, Jan 2013.

[68] Measurement of Tracking Efficiency. Technical Report CMS-PAS-TRK-10-002, CERN, Geneva, 2010.

[69] The CMS Collaboration. Nuclear effects on the transverse momentum spectra of charged particles in ppb collisions at 5.02 tev. *The European Physical Journal C*, 75(5):237, May 2015.

[70] Ekkard Schnedermann, Josef Sollfrank, and Ulrich Heinz. Thermal phenomenology of hadrons from 200a gev s+s collisions. *Phys. Rev. C*, 48:2462–2475, Nov 1993.

[71] The ALICE Collaboration. Centrality dependence of $\pi$, $k$, and $p$ production in pb-pb collisions at $\sqrt{s_{NN}} = 2.76$ tev. *Phys. Rev. C*, 88:044910, Oct 2013.

[72] Piotr Bożek and Iwona Wyskiel-Piekarska. Particle spectra in pb-pb collisions at $\sqrt{\mathbf{s_{NN}}} = \mathbf{2.76}$ tev. *Phys. Rev. C*, 85:064915, Jun 2012.

[73] Iu. A. Karpenko, Yu. M. Sinyukov, and K. Werner. Uniform description of bulk observables in the hydrokinetic model of $a+a$ collisions at the bnl relativistic heavy ion collider and the cern large hadron collider. *Phys. Rev. C*, 87:024914, Feb 2013.

[74] Edward Shuryak and Ismail Zahed. High-multiplicity $pp$ and $pa$ collisions: Hydrodynamics at its edge. *Phys. Rev. C*, 88:044915, Oct 2013.

[75] Rainer Fries, Vincenzo Greco, and Paul Sorensen. Coalescence models for hadron formation from quark-gluon plasma. *Annual Review of Nuclear and Particle Science*, 58(1):177–205, 2008.

[76] The CMS Collaboration. Study of the inclusive production of charged pions, kaons, and protons in pp collisions at 0.9, 2.76, 7 tev. *The European Physical Journal C*, 72(10):2164, Oct 2012.

[77] STAR Collaboration. Experimental and Theoretical Challenges in the Search for the

Quark Gluon Plasma: The STAR Collaboration's Critical Assessment of the Evidence from RHIC Collisions. *ArXiv Nuclear Experiment e-prints*, January 2005.

[78] PHENIX Collaboration. Formation of dense partonic matter in relativistic nucleus-nucleus collisions at RHIC: Experimental evaluation by the PHENIX collaboration. *ArXiv Nuclear Experiment e-prints*, October 2004.

[79] Measurement of the nuclear modification factor of identified strange and multi-strange particles in pPb collisions at sqrt(sNN) = 5.02 TeV with CMS experiment. Technical Report CMS-PAS-HIN-16-013, CERN, Geneva, 2018.

[80] Piotr Boek, Adam Bzdak, and Vladimir Skokov. The rapidity dependence of the average transverse momentum in p+pb collisions at the lhc: The color glass condensate versus hydrodynamics. *Physics Letters B*, 728:662 – 665, 2014.

[81] J. W. Cronin, H. J. Frisch, M. J. Shochet, J. P. Boymond, P. A. Piroué, and R. L. Sumner. Production of hadrons at large transverse momentum at 200, 300, and 400 gev. *Phys. Rev. D*, 11:3105–3123, Jun 1975.

[82] D. Antreasyan, J. W. Cronin, H. J. Frisch, M. J. Shochet, L. Kluberg, P. A. Piroué, and R. L. Sumner. Production of hadrons at large transverse momentum in 200-, 300-, and 400-gev $p-p$ and $p$-nucleus collisions. *Phys. Rev. D*, 19:764–778, Feb 1979.

[83] Michele Arneodo. Nuclear effects in structure functions. *Physics Reports*, 240(5):301 – 393, 1994.

[84] Nuclear modification factor of d0 mesons in pbpb collisions at snn=5.02tev. *Physics Letters B*, 782:474 – 496, 2018.

[85] The ALICE Collaboration. Transverse momentum distribution and nuclear modification factor of charged particles in $p$+Pb collisions at $\sqrt{s_{NN}}$=5.02 TeV. *Phys. Rev. Lett.*, 110:082302, Feb 2013.

[86] Transverse momentum, rapidity, and centrality dependence of inclusive charged-particle production in snn=5.02 tevp+pb collisions measured by the atlas experiment. *Physics Letters B*, 763:313 – 336, 2016.

[87] Rudolph C. Hwa and C. B. Yang. Scaling distributions of quarks, mesons, and proton for all $p_T$, energy, and centrality. *Phys. Rev. C*, 67:064902, Jun 2003.

[88] R. J. Fries, B. Müller, C. Nonaka, and S. A. Bass. Hadronization in heavy-ion collisions: Recombination and fragmentation of partons. *Phys. Rev. Lett.*, 90:202303, May 2003.

[89] V. Greco, C. M. Ko, and P. Lévai. Parton coalescence and the antiproton/pion anomaly at rhic. *Phys. Rev. Lett.*, 90:202302, May 2003.

[90] The JET Collaboration. Predictions for p+pb collisions at 5 tev. *International Journal of Modern Physics E*, 22(04):1330007, 2013.